13 Molding

13.1 Injection Molding, 753
13.2 Reactive Injection Molding, 798
13.3 Compression Molding, 811

The injection molding, compression molding, and casting-shaping operations all entail forcing the polymer into a cavity and reproducing its shape. In the process of casting, the cavity is filled by gravitational flow with a low viscosity liquid (reacting monomer or prepolymer) and, following polymerization the liquid solidifies. In compression molding, a prepolymer solid mass is heated up or melted and forced to undergo a squeezing flow by hot mold surfaces that close to form a final shape. The prepolymer usually cross-links and permanently assumes the shape of the closed cavity. In the injection molding process, a polymer melt is forced through an orifice (gate) into a closed, cold mold, where it solidifies under pressure in the shape of the mold cavity.

Two polymers can be used in sequence to fill the mold, forming skin–core sandwich molded articles. Air can also be introduced in partially melt-filled molds, and pressurized to form a polymer skin–air core sandwich structure, through the gas-assist injection-molding process. In all injection molding processes, the polymer is melted, mixed, and injected from the injection unit of the machine.

Finally, in the reaction injection-molding (RIM) process, low-viscosity reacting monomers or prepolymers are intimately mixed just before being injected into a hot cavity, where they react further and solidify. The RIM process, then, is a variation of the casting process, where highly reactive liquid systems are injected quickly, rather than being allowed to flow by gravity, into complex shape cavities, where they quickly react and solidify.

In this chapter we focus on injection molding, which, along with die forming, is one of the two most important shaping steps. We also discuss reaction injection molding and compression molding. From a process analysis point of view, the basic problems this chapter addresses are (a) nonisothermal and transient flow of polymer melts, followed by *in situ* cooling and solidification, and (b) nonisothermal and transient flow of reacting (polymerizing) liquids followed by *in situ* polymerization and heat transfer.

13.1 INJECTION MOLDING

Injection molding involves two distinct processes. The first comprises the elementary steps of solids transport, melt generation, mixing, and pressurization and flow, which are carried

Principles of Polymer Processing, Second Edition, by Zehev Tadmor and Costas G. Gogos.

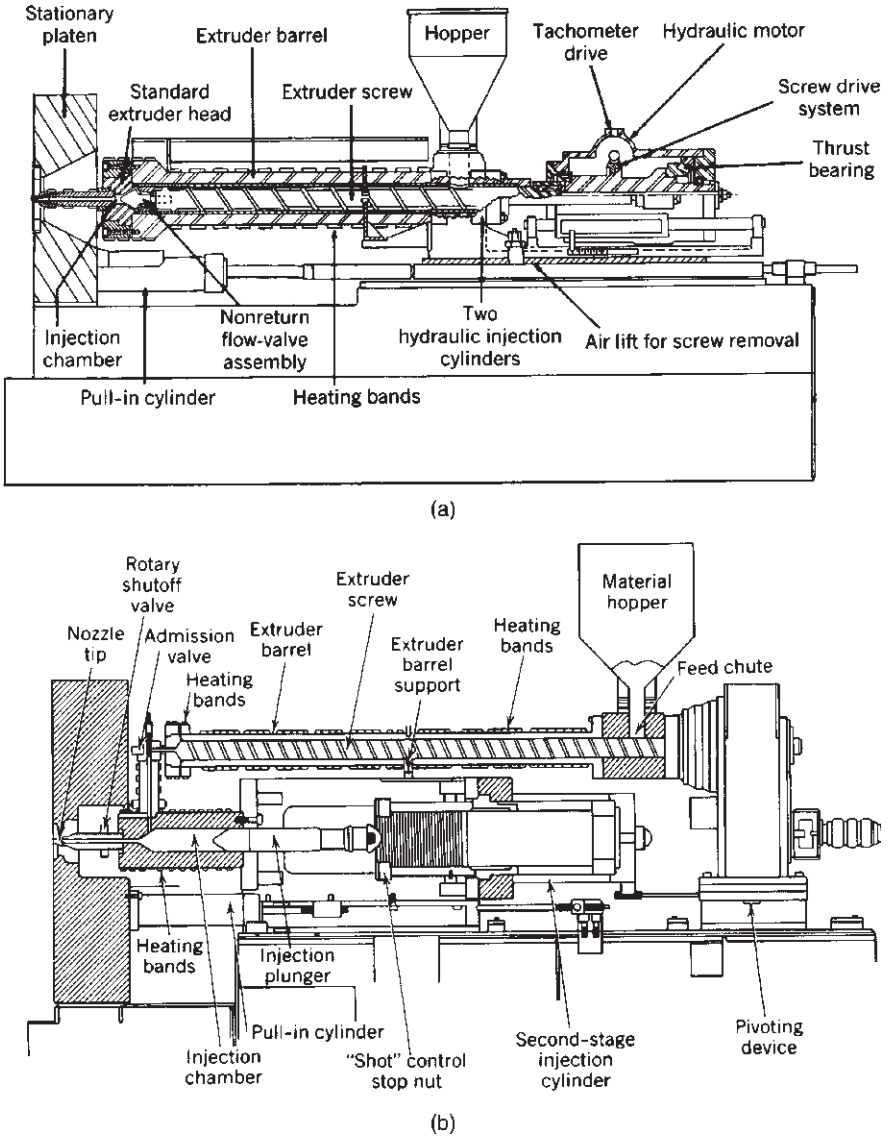

Fig. 13.1 (a) Reciprocating-screw machine, injection end. (b) Two-stage screw–plunger machine. [Courtesy of HPM Division of Koehring Company.]

out in the injection unit of the molding machine; the second is the product shaping and ''structuring,'' which takes place in the mold cavity. Most injection molding machines are the in-line, reciprocating-screw type, as illustrated in Fig. 13.1(a). Two-stage injection molding machines, shown in Fig. 13.1(b) are also used; the polymer melt is produced in an extruder and exits into a reservoir connected to a hydraulic piston device, which is cyclically pressurized to deliver the melt into the cold mold cavity.

The theoretical analysis of the injection unit involves all the facets of steady, continuous, plasticating screw extrusion, with the added complication of a transient

operation resulting from the intermittent screw rotation, on which axial motion is superimposed. In the injection unit the melting step is the dominant one regarding design and operation. Experimental work on melting in injection units (1) revealed a melting mechanism similar to that in plasticating screw extrusion, which was then used to formulate a mathematical model for the melting process (2). The product of the injection unit is the polymer melt accumulating in front of the screw. Melt homogeneity affects the filling process and final product quality. However, we assume that the same quality of well-mixed and uniform temperature melt is produced by the injection unit during each cycle, as well as from one cycle to the next.

To inject the polymer melt into the mold, the melt must be pressurized. This is achieved by the forward thrust of the screw (a) or the piston (b), both of which act as rams. Hence we have static mechanical pressurization, as discussed in Section 6.7, which results in positive displacement flow.

The injection ''molding cycle'' is shown schematically in Fig. 13.2, indicating the simultaneous positions and states of the screw, the mold and the process. A typical injection mold is made of at least two parts, one of which is movable so that it can open and close during different parts of the molding cycle, as shown in Fig. 13.3(a) and 13.3(b). The entire mold is kept at a constant temperature below T_g or T_m. The melt exits the nozzle of the injection unit and flows through the *sprue*, *runner*, and *gate* into the mold cavity. Each of these structural elements of the mold performs well-defined functions and affects the molding operation. Thus the sprue forms the overall entrance into the mold. It should not generate large resistance to flow, yet at the same time the melt in it should

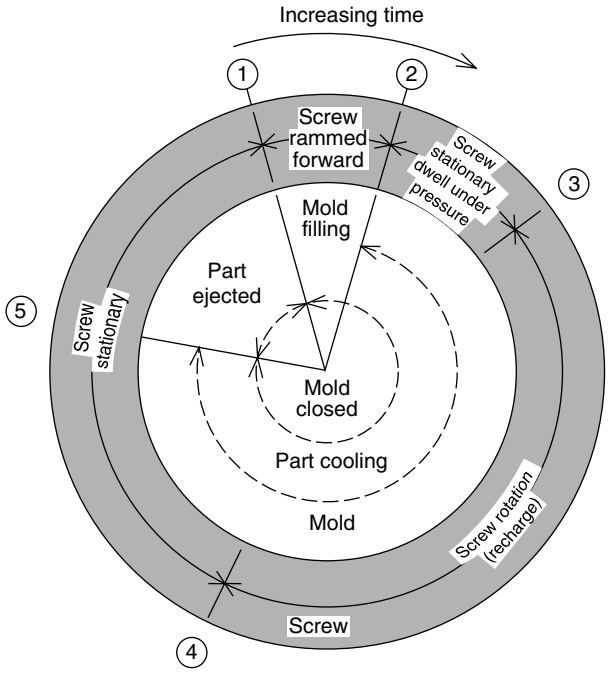

Fig. 13.2 The injection molding cycle. [Reprinted by permission from R. C. Donovan, ''An Experimental Study of Plasticating in a Reciprocating-Screw Injection Molding Machine,'' *Polym. Eng. Sci.*, **11**, 353 (1971).]

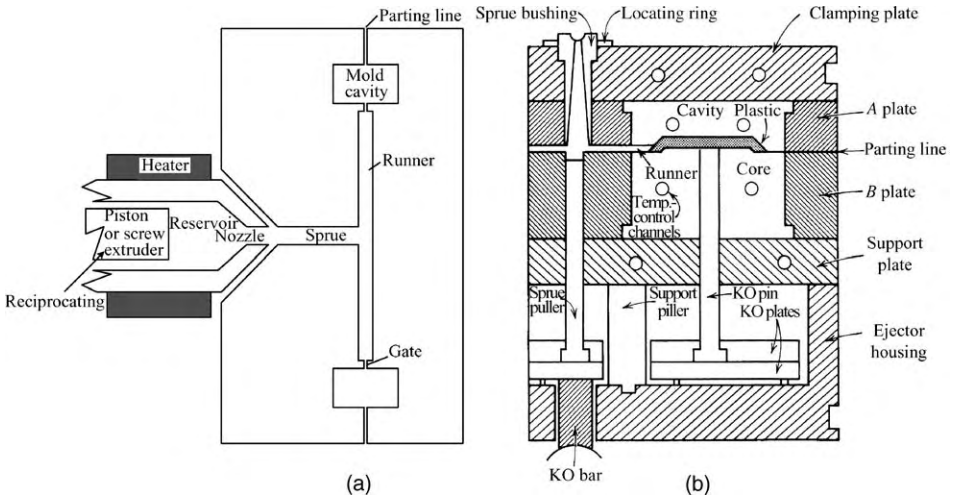

Fig. 13.3 (a) Schematic view of injection molding tooling showing the tip of the injection system and its connection to the mold. Melt passes from the reservoir through the nozzle, the sprue, and the runner system, entering the mold cavities through the gate. (b) Two-plate mold. [Courtesy of Robinson Plastic Corporation.]

quickly solidify upon completion of injection and should be extracted from it without difficulty. The sprue should also form a streamlined transition between the nozzle and runner system. All these functions are attainable by a short, diverging conical shape.

The function of the runner system is to bring the hot melt to the cavities. This should be done with the minimum of material and pressure-drop ''waste.'' Therefore the runner conduit length must be kept to a minimum, and the cross section should be *optimally* set for low pressure drop, low material waste, and relatively slow cooling, avoiding premature solidification and ''short shots.'' Generally, the runner is about 1.5 times the characteristic thickness of the molded part, and it is of circular cross section to minimize heat loss as well as to facilitate easy machining. Polymer saving and faster cycles occasionally can be achieved by hot-runner systems where the polymer in the runners is prevented from solidifying through heating units built around them in the mold plate housing them in hot-runner molds. Alternatively, particularly with large parts, it is sufficient to insulate the runner system from the mold. In both cases, the sprue can, in effect, be eliminated from the design.

The gate controls the flow of the polymer melt into the mold. Its size, shape, and position are affected by a number of considerations. First, a narrow gate is desirable from the standpoint of ease of separation of the molded part from the runner system, as well as solidification after the completion of melt injection, to isolate the cavity from the rest of the system. Of course, early solidification must be prevented. Moreover, narrow gates may be detrimental to the finished product because they also bring about large shear rates and stresses (above the melt fracture region), and consequent excessive temperature rise. When the stress level must be reduced, divergent fan gates are used, spreading the flow. Generally speaking, the gate length is about half the characteristic thickness of the section

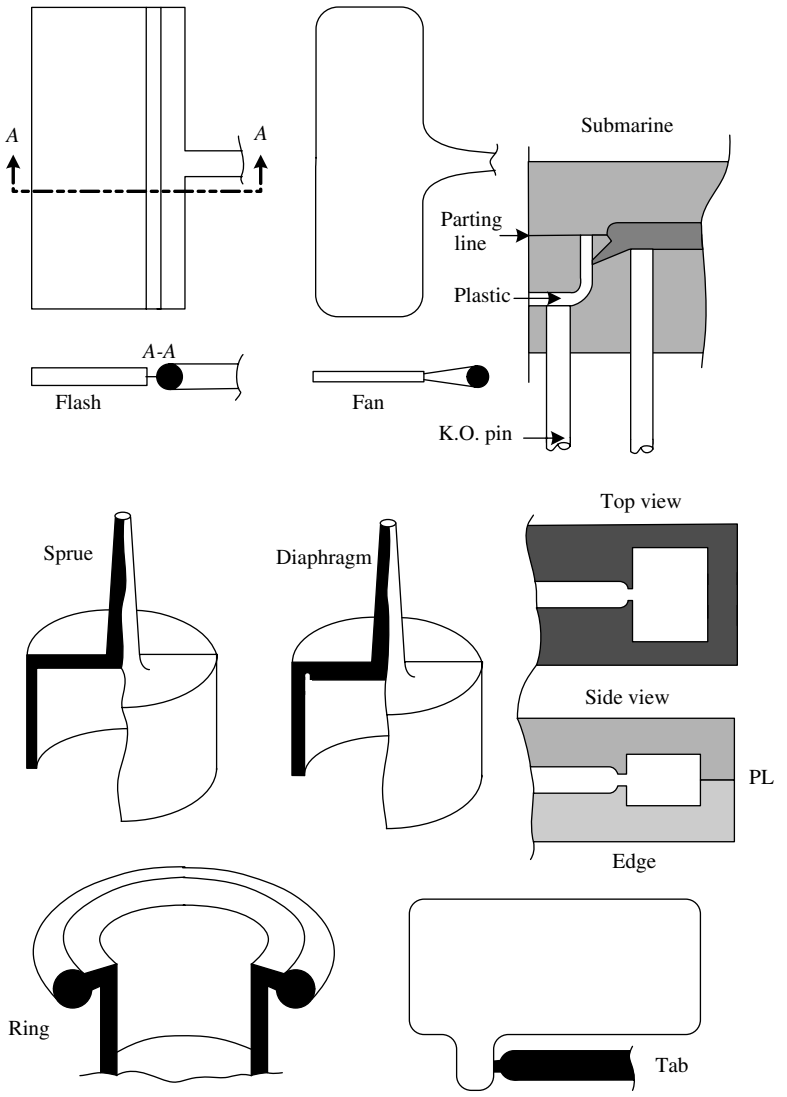

Fig. 13.4 Typical gate designs and locations. [Reprinted by permission from I. Rubin, *Injection Molding—Theory and Practice*, Wiley, New York, 1972.]

where the gate is attached (usually the heavy sections). It is positioned such that the emerging stream impinges on the opposite wall. Figure 13.4 presents typical gate designs and locations. In multiple-cavity molds, gates (and runners) also serve the function of balancing flow such that all cavities fill simultaneously. Further discussion of sprue, runner, and gate design considerations can be found in the literature (3,4). The detailed mathematical modeling of the flow of polymer melts through these conduits is not easy, and involves most of the complexities of the cavity filling problems, which we discuss below.

Example 13.1 Flow in an Idealized Runner System We consider a straight tubular runner of length L. A melt following the Power Law model is injected at constant pressure into the runner. The melt front progresses along the runner until it reaches the gate located at its end. We wish to calculate the melt front position and the instantaneous flow rate as a function of time. We assume an incompressible fluid in isothermal and fully developed flow, and make use of the pseudo–steady state approximation.

With the preceding assumption, the *instantaneous* flow rate $Q(t)$, at given constant inlet pressure, P_0, and instantaneous fill length, $Z(t)$ at time, t, is given by (see Example 3.4 or Table 12.2):

$$Q(t) = \frac{\pi R^3}{s+3}\left(\frac{RP_0}{2mZ(t)}\right)^s \tag{E13.1-1}$$

The position $Z(t)$ is obtained from a mass balance

$$Z(t) = \frac{1}{\pi R^2}\int_0^t Q(t)dt \tag{E13.1-2}$$

Differentiating the preceding equation, we obtain

$$\frac{dZ(t)}{dt} = \frac{Q(t)}{\pi R^2} \tag{E13.1-3}$$

Finally, substituting the flow rate expression into the preceding equation, followed by integration, gives

$$Z(t) = \left(\frac{1+n}{1+3n}\right)^{n/(1+n)} R\left(\frac{P_0}{2m}\right)^{1/(1+n)} t^{n/(1+n)} \tag{E13.1-4}$$

and the flow rate is

$$Q(t) = \pi R^3\left(\frac{1+n}{1+3n}\right)^{n/(1+n)}\left(\frac{n}{1+n}\right)\left(\frac{P_0}{2m}\right)^{1/(1+n)} t^{\frac{1}{1/(1+n)}} \tag{E13.1-5}$$

It is interesting to note that the ''penetration depth'' $Z(t)$ is proportional to the radius R. This implies that the ratio of penetration depths of the same material in two conduits of different radii is given by $Z_1/Z_2 = R_1/R_2$, and for constant P_0 is dependent only on geometry and not the rheological behavior of the fluid. We next consider a polymer melt with $m = 2.18 \times 10^4\,\mathrm{N\cdot s^n/m^2}$ and $n = 0.39$, and calculate $Z(t)$ and $Q(t)$ for an applied pressure $P_0 = 20.6\,\mathrm{MN/m^2}$ in a runner of dimensions $R = 2.54\,\mathrm{mm}$ and $L = 25.4\,\mathrm{cm}$.
The expressions for $Z(t)$ and $Q(t)$ for the values just given become

$$Z(t) = 0.188t^{0.281} \tag{E13.1-6}$$

$$Q(t) = \frac{1.07 \times 10^{-6}}{t^{0.719}} \tag{E13.1-7}$$

Values of $Z(t)$ and $Q(t)$ are listed in the following table for various times:

t (s)	Z (m)	Q (m^3/s)
0	0	∞
0.5	0.155	1.76×10^{-6}
1	0.188	1.06×10^{-6}
1.5	0.211	0.8×10^{-6}
2	0.228	0.65×10^{-6}
2.88	0.253	0.5×10^{-6}

These results clearly indicate that we should expect a very high flow rate initially, followed by a rapidly dropping flow rate, $Q(t)$ as the runner fills up. The first half of the runner is filled in 10% of the total runner fill time. From the equation for $Q(t)$ given earlier (under the assumptions made), it is easy to show that, for a constant flow rate, a linear increase in the applied pressure is required. In practice, the initial part of the mold filling cycle is one of increasingly applied pressure and almost constant flow rate. If the mold is easy to fill, this situation will persist until mold filling is completed. On the other hand, if the mold flow resistance is high (as, for example, in Fig. 13.5), the pressure will reach its maximum available value and will remain constant for the rest of the filling time, while the flow rate decreases with time. In the real nonisothermal case, once the flow rate reaches low values, the melt has time to cool by conduction to the cold walls, its viscosity increases exponentially, and the flow stops completely, resulting in ''short shots.''

For comparison purposes, the numerical simulation results of nonisothermal runner filling are given in the following table (5). For the same conditions, using a flow activation energy value of 6 kcal/g · mole. It is clear from the tabulation, and especially from the nonisothermal-to-isothermal flow ratio, that the polymer is cooling rapidly in the runner and that a ''short shot'' will result soon after 1 s. Huang's (5) simulation indicates that a ''frozen skin'' was formed at 0.7 s in the axial region of 2–4 cm from the entrance.

t (s)	Z (t)	Q (t)	$Z(t)/Z(t)\|_{T=\text{const.}}$ (%)	$Q(t)/Q(t)\|_{T=\text{const.}}$ (%)
0.5109	0.111	1.10×10^{-6}	0.77	0.63
0.9703	0.140	0.51×10^{-6}	0.74	0.48

After the cavity has been filled, the injection pressure is maintained to ''pack'' a small additional amount of melt into the cavity and to compensate for the thermal contraction of the polymer during the cooling and solidification stages. Packing increases the cavity pressure rapidly and appreciably. When the externally applied pressure is removed (by retracting the reciprocating screw or piston of the injection-molding machine), backflow out of the cavity takes place, unless the polymer in the gate has solidified or unless such flow is prevented by a one-way valve. At the end of the backflow, if there is any, only cooling of the polymer takes place, together with minute contraction-induced local flows. When the polymer has solidified sufficiently to withstand the forces of ejection, the mold is opened and the molded article is removed from the cavity with the aid of the ejection ''knock out'' (KO) pins.

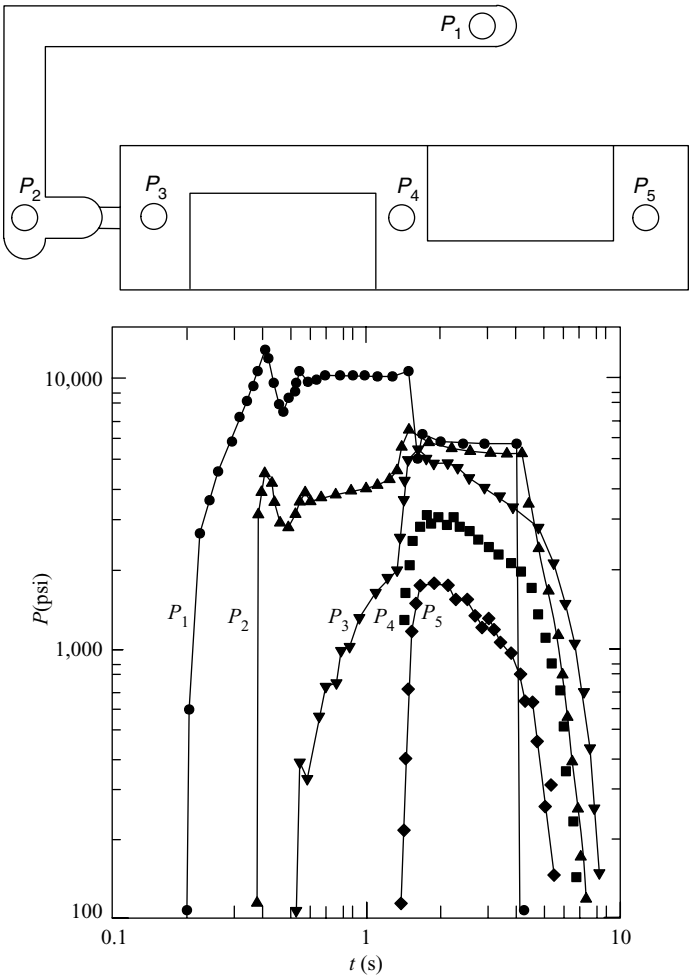

Fig. 13.5 Experimental pressure traces during mold filling of a rectangular cavity shown on the top with polystyrene at 400°F. P_1 is the pressure at the nozzle, P_2 the pressure at the end of the runner outside the gate, and P_3–P_5 are cavity pressures at the locations indicated. Pressure traces P_4 and P_5 are questionable because of an unintentional preloading of the transducers upon mold closing. [Reprinted by permission from W. L. Krueger and Z. Tadmor, "Injection Molding into Rectangular Cavity with Inserts," *Proc. Society of Plastics Engineering 36th Annu. Tech. Conf.*, Washington, DC, 1978, pp. 87–91.]

A detailed study of mold filling was done by Krueger and Tadmor (6). The various stages of the injection process was followed by pressure gauges in the mold, as shown in Fig. 13.5. In this experiment polystyrene (PS) was injected into a shallow rectangular cavity with inserts as shown in the figure. Pressure transducers were placed in the nozzle, runner, and mold cavity; their output was scanned every 0.02 s and retrieved by a computer. The nozzle pressure was set by machine controls to inject at a constant 10,000 psi and, upon mold filling, to hold the pressure at 5500 psi.

Appreciable pressure overshoots and undershoots are noticeable. The pressure trace at the end of the runner system (P_2) at lower levels follows the pattern of the nozzle pressure.

The two become equal upon cessation of flow when the mold is full. The difference $P_1 - P_2$ indicates the pressure drop over the sprue and runner system. The pressure drop across the gate is given approximated by $P_2 - P_3$. We note that just downstream of the gate, the pressure P_3 increases with time throughout the filling process (from about 0.4 s to 1.3 s). As Example 13.1 pointed out, such a pressure trace approaches conditions of constant filling rate. This is supported by ram position measurements, which were also retrieved at 0.02-s intervals. We further note that, upon mold filling, when P_5 sharply increases, there is also a steep increase in all the pressures except the nozzle pressure, which is then reduced to 5500 psi.

During the ''hold'' time, the three pressure transducers within the cavity record different pressures in spite of the absence of appreciable pressure drops due to flow. This is probably the result of skin formation and solidification preventing true core pressure (liquid) recordings. All cavity pressures drop gradually upon solidification, and this gradual pressure drop continues after gate solidification. Of particular practical interest is the residual pressure at the time the mold is opened. If it is near zero, there is the real danger that, with further cooling to room temperature, the part will either be smaller than the cavity or will show ''sink marks.'' On the other hand, if the residual pressure is high, the part cannot be easily ejected from the mold and will be ''scarred'' or deformed during the process.

From the short description of the molding cycle, it is clear that flow, viscous heat generation (filling flow rates are very high), heat transfer, and melt stress relaxation occur to varying degrees of intensity simultaneously. The transport phenomena involved are coupled, and since the solidification times can be comparable to the polymer relaxation times [Deborah number $(\mathrm{De}) \sim 1$], molded articles solidify under strained conditions, that is, they contain ''frozen-in'' strains. Such internal strains greatly affect the properties and morphology of molded articles. Thus, we can use the injection molding process to ''structure'' polymers. We will examine the various stages of injection molding separately.

Mold Filling

It is now clear that there is no simple answer to the question of what are the optimal conditions for the proper molding of a specific polymer in a given mold cavity. Figure 13.6, however, illustrates an empirical answer, showing an experimentally determined ''molding area'' processing window on the melt temperature–injection pressure plane. Within this area the specific polymer is *moldable* in the specific cavity. The area is bounded by four curves. Below the bottom curve, the polymer is either a solid or will not flow. Above the top curve, the polymer degrades thermally. To the left of the ''short shot'' curve, the mold cannot be completely filled, and to the right of the ''flash'' curve, the melt flows in the gaps formed between the various metal pieces that make up the mold, creating thin webs attached to the molded article at the parting lines.

Another practical approach to the question of moldability, especially in comparing one polymer with another, is the use of a standard spiral mold cavity and the measurement, under prescribed molding conditions, of the spiral length filled (7).

Because mold filling is a complex process, flow visualization studies have been useful and necessary, both for the actual mold design and for the mathematical simulation of the process. The first important experimental contributions were made by Gilmore and Spencer (8,9) whose work forms the basis of a review chapter by Beyer and Spencer (10). Ballman et al. (11–13) conducted mold filling experiments in the early 1960s. A decade later, a time that marks the beginning of serious efforts to solve

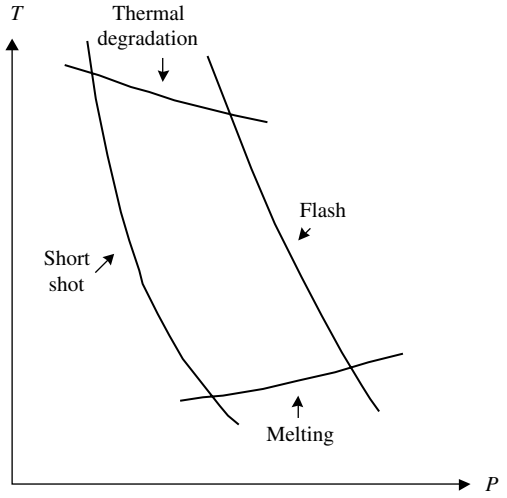

Fig. 13.6 Schematic ''molding area'' or ''molding window'' diagram that can be determined for a given polymer and mold cavity.

the injection molding problem, a new wave of mold-filling flow visualization studies were reported by Aoba and Odaira (14), Kamal and Kenig (15), White and Dee (16), and Schmidt (17). These studies revealed that the mode of filling at moderate flow rates is an orderly forward flow, as shown schematically in Fig. 13.7(a) for a constant

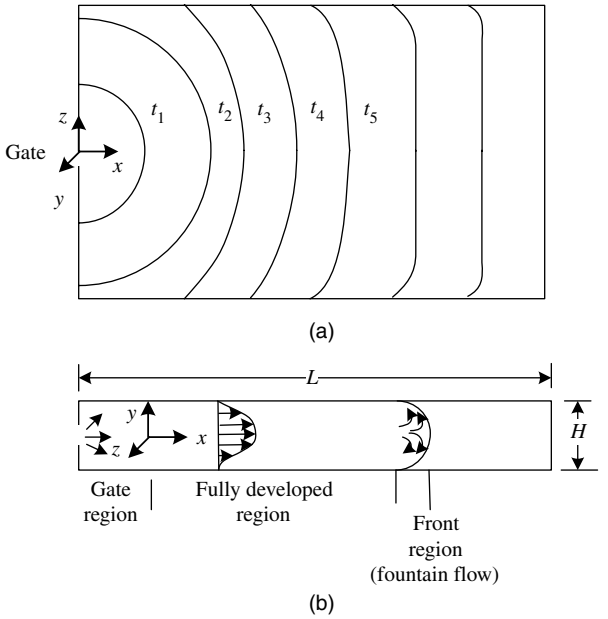

Fig. 13.7 Schematic representation of the flow patterns during the filling of an end-gated rectangular mold whose width is much greater than its thickness. (a) Width direction flow fronts at various times. (b) Velocity profiles in the fully developed region, and schematic representation of the fountain effect in the front region.

depth rectangular cavity. During the early stages of filling, the flow is radial and the melt ''front'' circular (in this top view). The flow character changes as the melt front advances away from the gate, whereby the predominant velocity component is now v_x and the front shape is either flat for isothermal filling or curved for filling into cold molds (16).

In mold cavities with inserts and nonuniform thickness distribution, the flow pattern is more complicated. This problem was investigated by Krueger and Tadmor (6) using a thin, rectangular 1.5 $\times$ 6-in cavities like the one shown in Fig. 13.5. Inserts of various shapes and sizes could be placed in different locations in the mold, creating either obstacles to the flow or regions of different thickness. PS was injected, and the position and shape of the advancing front could be traced by a series of short shots, as shown in Fig. 13.8.

Figure 13.8(a) shows the trace of the advancing front recorded from the experimental molded pieces in Fig. 13.8(b). The solid lines are the experimentally measure advancing front lines obtained from the short shots, the simulated results discussed later are marked by the $\times$ signs, and the broken curve shows the weld lines clearly visible in the finished products.

In Fig. 13.8, Sample 1 shows that the outline (shape) of the front is circular in the deep section and becomes somewhat distorted upon entering the thinner region. The flow is split by the T insert and reunites past the insert, forming a weld line. The location and the shape of the weld line are determined by the flow profile around the insert. The insert strongly affects the direction of the advancing front which, as we see later, determines the direction of molecular orientation. We would expect, therefore, a highly nonuniform orientation distribution in such a mold.

In Fig. 13.8, Sample 2, the insert was placed in the thin section close to the gate, completely changing the weld line location and shape, as well as the advancing melt profiles (consequently, the orientation distribution). Figure 13.8, Sample 3, shows an S-shaped deep section connected by a thin web. We note that the penetration lengths in the deep and shallow sections of the mold, which are being simultaneously filled, qualitatively follow the predictions of Example 13.1, where for $P =$ constant, $Z(t)$ is proportional to the cross-sectional thickness of the channel, and, to a first approximation, is independent of the rheological properties of the melt. This is, in fact, what is observed (6). There is also formation of two weld lines, where the second weld line branches out sideways upon entering the deep section.

Figure 13.8, Sample 4, shows flow in an S-shaped cavity without weld line formation. Finally, Fig. 13.8, Sample 5, shows flow around square and circular inserts, with pronounced weld line formation. These results draw attention to the complex flow patterns occurring even in relatively simple molds. In particular, it is interesting to note the shape of weld lines, which are important not only because they sometimes form visual defects in the product, but also because they generally represent ''weak'' regions in properties. In general, we can state that weld lines are formed whenever advancing melt fronts ''meet,'' that is, whenever their outward normals are opposite or converging. The former case occurs in double gate filling and immediately past cavity obstacles, whereas the latter occurs when the front is composed of two segments and there is a discontinuity in the shape of the advancing front.

As mentioned in Section 12.4, weld line interfaces can be characterized by an appreciably different (lower) entanglement level as compared to the bulk of the material. The formation and properties of the weld lines can be explained in view of the detailed

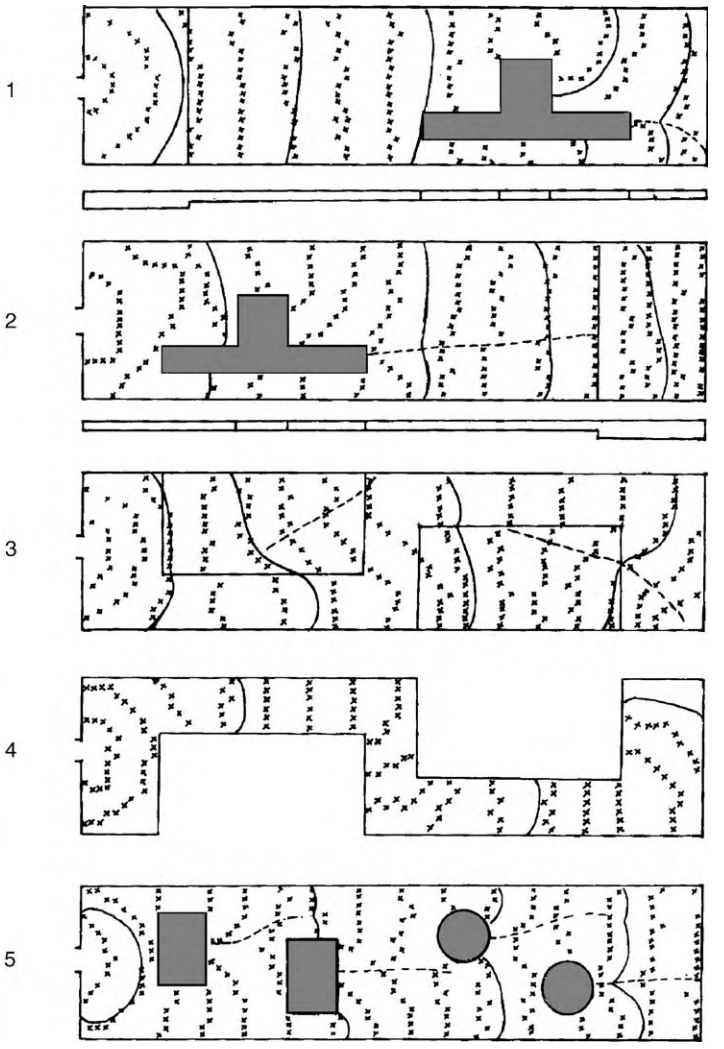

Fig. 13.8(a) Experimental (solid lines) and simulated (×) advancing front profiles in a shallow rectangular cavity with inserts of various shapes. Experimental profiles were obtained by short shots (6), as shown in Fig. 13.8(b). Cavity dimensions are 3.8 × 15.2 cm (1.5 × 6 in). Sample 1: A T-shaped insert completely obstructing the flow, and a step reduction in thickness as indicated in the figure. The deep section was 0.335 cm and the thin section varied from 0.168 to 0.180 cm. (In the simulations, the actual thickness distribution was determined by measuring the injection molded samples corrected for contraction, but not for mold distortion.) Sample 2: the reverse of Sample 1, but the shallow section has a uniform thickness of 0.166 cm. Sample 3 contained two rectangular web inserts, giving rise to a correspondingly shallow section, 0.35 cm thick. Sample 4 had two rectangular inserts blocking flow, giving rise to an S-shaped cavity of thickness ranging from 0.165 cm to 0.173 cm. Sample 5 had two rectangular and two circular inserts obstructing the flow with the rest of the cavity at uniform thickness of 0.323 cm. The broken curves denote visually observable weld lines. [Reprinted by permission from W. L. Krueger and Z. Tadmor, "Injection Molding into Rectangular Cavity with Inserts," *Proc. Soc. of Plastics Engineers, 36th Annu. Techn. Conf.*, Washington, DC, 1978, pp. 87–91.]

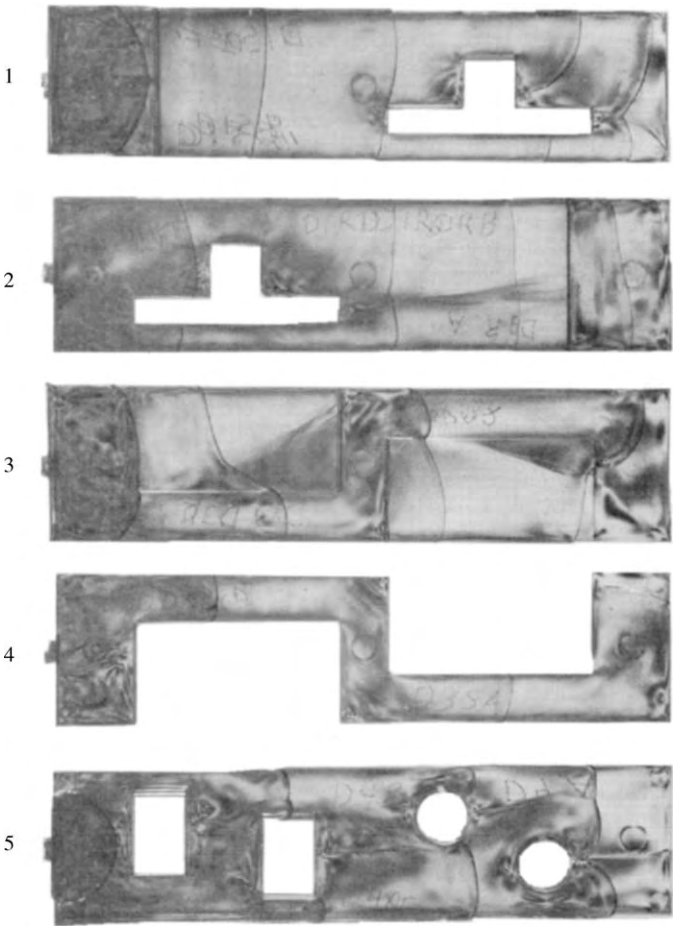

Fig. 13.8(b) Photographs of superimposed short shots using polarized light. [Reprinted by permission from W. L. Krueger and Z. Tadmor, "Injection Molding into Rectangular Cavity with Inserts," *Proc. Society of Plastics Engineers, 36th Annu. Techn. Conf.*, Washington, DC, 1978, pp. 87–91.]

flow pattern at and near the advancing front, which is different from that in the bulk. In the front region, the melt at the center of the thickness direction, which moves with the maximum velocity of the parabolic-like velocity profile, spills out or *fountains* out to the mold wall to form the surface of the molded article at that location, as in Fig. 13.7(b). This is the only way of filling the region near the wall of the mold, where there is no slip. Thus, in the front region, the central core decelerates from the maximum velocity at the centerline upstream from the front, to the mean velocity at which the front advances. As it decelerates in the direction of flow, x, it acquires a velocity component in the thickness direction, y.

The term *fountain effect* or *fountain flow* was coined and discussed by Rose (18), and it is essentially the reverse of the flow observed near a plunger emptying a fluid out of a channel of the same cross section. The two-dimensional flow in the

front region is important in determining the quality and morphology of the surface of the molded article as well as the nature of weld lines. We shall return to weld line morphology following the discussion of the flow pattern in the melt front.

When the gate faces a mold wall that is far away, and when the filling flow rate is very high, the phenomenon of ''jetting'' is observed. The melt emerging from the gate forms a jet that rapidly advances until it is stopped by the mold wall opposite to it. Both melt fractured and smooth melt jets have been observed. There are two modes of mold filling under jetting conditions. In the first mode, jetting continues after the jet tip has touched the opposite wall and the jet folds over many times, starting at the impingement surface and continuing toward the gate. When the cavity is almost full of the folded melt jet, regular filling and compression of the folded jet occurs. Thus the filling is in the backward direction. In the second mode of filling, jetting stops after impingement of the jet tip on the opposite wall, and regular forward filling commences. In both cases, weld lines may present problems with respect to the optical and mechanical properties of the molded article.

It has been experimentally observed that jetting can occur whenever the dimension of the fluid stream is smaller than the smallest dimension in the plane perpendicular to the flow (19). It is thus related both to the gate size and to the degree of extrudate swelling of the melt, rather than to the level of the axial momentum. Filled polymers, which swell less than unfilled melts, exhibit jetting at lower filling rates. Two ''cures'' for jetting are commonly practiced. First, the gate is positioned so that the emerging melt impinges on a *nearby* wall; second, ''fan'' gates are used, which increase one of the dimensions of the exiting melt stream, thus decreasing its momentum.

Mold Filling Simulations

A complete mold filling simulation would require the calculation of the detailed velocity and temperature profiles throughout the mold flow region, including the position and shape of the advancing front. This would suffice, in principle, to determine orientation distribution affecting the article morphology, which evolves upon cooling and solidification. Such a complete model, if available, would be instrumental in assisting the theoretical mold design, as well as in optimizing molding conditions for specified property requirements.

The complete problem, of course, is extremely complex even for a relatively simple mold, and is hardly soluble for intricate molds. Fortunately, however, a great deal of information and insight can be obtained by simulating (i.e., modeling) selected aspects of the filling problem in isolated ''flow regions.'' Each of these regions requires a unique approach and mathematical tools. Considering the mold filling visualizations in Fig. 13.7(b), we distinguish among the following regions.

1. *The* ''*fully*'' *developed region*. During the filling process most of the melt flows in an almost fully developed flow in a narrow-gap configuration between cold walls. The nature of this flow determines filling time and part core orientation, as well as the occurrence of short shots. A great deal of insight can be obtained by analyzing one-dimensional flow (either radial, spreading disk, or rectilinear) of hot melt between cold walls. The coupling of the momentum and energy equation eliminates analytical solutions, and finite difference methods can be used.

2. *The close neighborhood of the front region*. As pointed out earlier, this region determines both surface properties (skin formation) and weld line formations. Hence, a detailed analysis of the front region is warranted. This region can be simulated either by approximate analytical or detailed numerical models.
3. *The gate region*. This region is dominant at the beginning of mold filling. It contributes less as the melt front advances and, because fresh melt is hot in this region, melt memory of the flow experience in this region soon decays.

We discuss some of these regions in detail below. In addition, we concern ourselves with the *overall* flow pattern during filling. Recall that the manner in which a mold is filled—that is, the location of the advancing melt front—affects the weld-line location and the orientation distribution and may be responsible for poor mold filling conditions.

The Fully Developed Region A number of mathematical simulations of the flow and heat transfer in the fully developed region have been reported (11,15,20–25). Here we follow the work of Wu et al. (23), who simulated the filling of a center gated disk (Fig. 13.9). A frozen surface layer (frozen ''skin") can be formed during the filling process, which forces the fluid to flow through a channel of reduced cross section. Assuming constant thermophysical properties, quasi-steady-state, $\partial v_r/\partial t = 0$, and neglecting $\tau_{\theta\theta}$ and τ_{rr} in the r-momentum equation, as well as the axial conduction in the energy equation, these balance expressions become

$$\frac{d\tau_{zr}}{dz} = \frac{dP}{dr} \tag{13.1-1}$$

$$\rho C_p \left(\frac{\partial T}{\partial t} + v_r \frac{\partial T}{\partial t} \right) = k \frac{\partial^2 T}{\partial z^2} - \tau_{\theta\theta} \frac{v_r}{r} - \tau_{zr} \frac{\partial v_r}{\partial z} \tag{13.1-2}$$

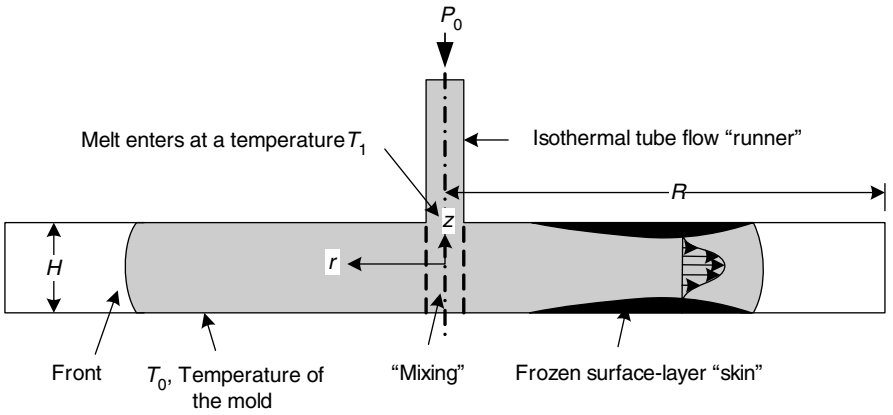

Fig. 13.9 Cross-sectional view of a center-fed, disk-shaped mold cavity. Indicated schematically are the frozen-skin layer that can form during filling, as well as the ''nipple''-shaped velocity profile.

The term $\tau_{\theta\theta} v_r / r$ is significant only at small values of r. Inserting the Power Law constitutive equation

$$\tau_{zr} = -m \left| \frac{dv_r}{dz} \right|^{n-1} \frac{dv_r}{dz} \tag{13.1-3}$$

where $m = m_0 \exp(\Delta E / RT)$ and n is a constant. The radial pressure drop is given (22) by the following equation

$$\left| \frac{dP}{dr} \right| = \left[\frac{Q(t)}{4\pi r \int_0^{H/2} (z^{1+s}/m^s)\, dz} \right]^n \tag{13.1-4}$$

The velocity can be obtained by integration of Eq. 13.1-1 and using Eq. 13.1-4

$$v_r(r, z, t) = -\left| \frac{dP}{dr} \right|^s \int_{H/2}^{z} \left(\frac{z}{m} \right)^s dz \tag{13.1-5}$$

For the numerical calculation of the pressure drop, as well as the velocity field, one must iterate the pressure at every radial position until the flow rate in the cavity is the same as that across the tube entrance. In both Eqs. 13.1-4 and 13.1-5, the consistency index m varies with z, since the temperature varies in the thickness direction. Two boundary conditions used in the energy equation are of interest. At the advancing front $r = r_{ik}$, the heat transferred to the air in the mold dictates that the term $2r_{ik}\, h(T_{ik} - T_a)/(r_{ik}^2 - r_{ik-1}^2)$ be included in the right-hand side of Eq. 13.1-2, where h is the heat-transfer coefficient to the air. At the mold wall

$$k \left(\frac{\partial T}{\partial z} \right)_{z=H/2} = h \left[T_0 - T\left(r, \frac{H}{2}, t \right) \right] \tag{13.1-6}$$

where T_0 is the mold bulk temperature and h is a heat-transfer coefficient that is taken to be equal to k_{mold}/d, where d is the distance from the mold surface to the depth where the mold temperature is, T_0. The energy equation is transformed into a difference equation using an implicit formula and solved by the Crank–Nicolson (26) or by methods discussed by O'Brien et al. (27). The grid size used can be logarithmically decreasing with increasing z, so that the details of the rapidly changing temperature and velocity can be revealed.

The simulation results indicate that as far as filling time calculations are concerned, the important variable is the ratio of the rate of heat generated by viscous dissipation to that lost by heat transfer to the cold walls. As a matter of fact, when the ratio is close to unity, fair estimates of filling times can be obtained by assuming isothermal flow.

The flow front is found to advance at an ever decreasing rate, when the disk-shaped cavity is fed at a constant tube-entrance pressure (see Example 13.1). Correspondingly, the filling pressure builds up at an ever-increasing rate if the front is to advance at a constant filling rate. As mentioned earlier, a constant filling rate can be assumed if the mold is easy to fill. Realistically, the flow rate is constant for the early part of filling, and drops during

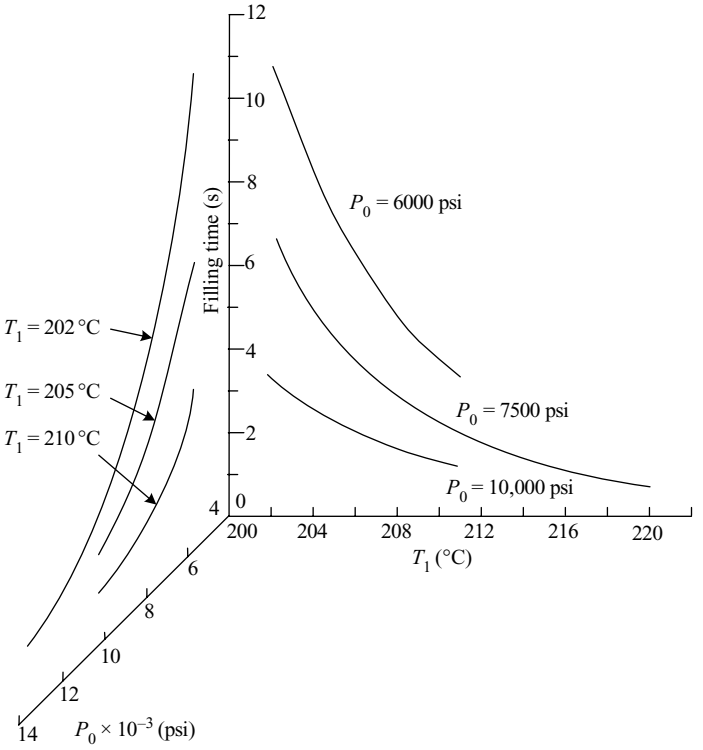

Fig. 13.10 Filling time versus entrance melt temperature at three constant injection pressures and filling time versus injection pressure at three constant entrance melt temperatures. Mold dimensions are $R = 9\,\text{cm}$, $H = 0.635\,\text{cm}$. The polymer is unplasticized polyvinyl chloride (PVC) of $n = 0.50$, $m(202°\text{C}) = 4 \times 10^4$ $(\text{N} \cdot \text{s}^n/\text{m}^2)$, $A = 6.45 \times 10^{-8}$, $\Delta E = 27.8\,(\text{kcal/g} \cdot \text{mole})$, $\rho = 1.3 \times 10^3$ (kg/m^3), $C_p = 1.88 \times 10^3$ $(\text{J/kg} \cdot \text{K})$, and $k = 9.6 \times 10^{-2}$ $(\text{J/m} \cdot \text{s} \cdot \text{K})$. [Reprinted by permission from P. C. Wu, C. F. Huang, and C. G. Gogos, "Simulation of the Mold Filling Process," *Polym. Eng. Sci.*, **14**, 223 (1974).]

the latter part. The filling time versus melt temperature at the mold entrance, as well as versus injection pressure, is plotted in Fig. 13.10 for an unplasticized polyvinyl chloride (PVC) resin.

The slope of the filling time versus melt temperature curves depends on the activation energy for flow, that is, the temperature sensitivity of the consistency index m. On the other hand, the slope of the filling time versus injection pressure curves depends on the value of the Power Law model index n. The temperature profiles at the instant of complete fill for the same mold and resin entering the mold at 202°C and 15,000 psi are shown in Fig. 13.11. A number of features are interesting. First, almost isothermal conditions prevail in the thickness region from the center of the mold halfway to the wall. This is because the velocity profile is almost flat and heat transfer is negligible. Appreciable and rapid conductive cooling occurs only *very* near the mold cavity wall.

If 150°C is taken to be a temperature level where PVC has a practically infinite viscosity, then an effective thin frozen skin is formed for $r > 2.5\,\text{cm}$. At lower injection

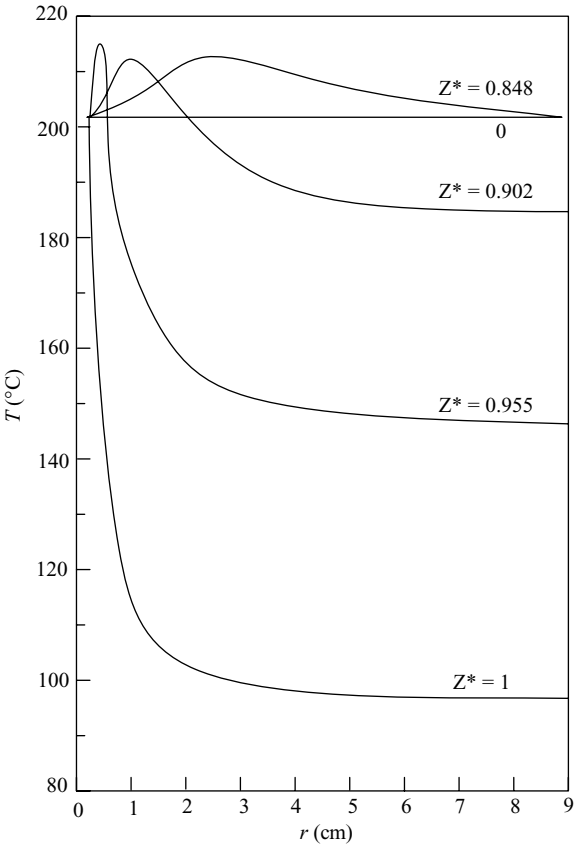

Fig. 13.11 Temperature distribution at the instant of fill as a function of radial distance and at various values of $Z^* = z/(H/2)$, for PVC at 15,000 psi, $H = 0.635$ cm, $t = 1.45$ s; $R = 9$ cm, $T_1 = 202°C$, $T_0 = 30°C$. [Reprinted by permission from P. C. Wu, C. F. Huang, and C. G. Gogos, "Simulation of the Mold Filling Process," *Polym. Eng. Sci.*, **14**, 223 (1974).]

pressures, thicker frozen skin layers are formed. The dependence of the frozen-skin profile on molding variables is indicated in Fig. 13.12, where the frozen skin at the moment of fill is plotted under the conditions specified. Its thickness decreases with increasing pressure, melt, and mold temperature and mold thickness. The shape of the frozen skin profile is characterized by a maximum (a "pinch" region). Near the entrance, fresh hot melt keeps the skin to a minimum, and near the front, the melt near the walls is still hot because it originates from the center region. It is the pinch region, in which flow would stop first, that would be responsible for short shots at low injection pressures. It is also worth noting that the shape of the frozen skin creates both an axial stretching flow and a z-component velocity. This is particularly true in the gate region. The problem has been discussed by Barrie (28). In the disk cavity, the stretching flow discussed earlier offsets the assumption of neglecting the term dv_r/dr.

The Front Region The front region was analyzed by Tadmor (29) in an attempt to model the experimentally observed molecular orientation distribution in molded articles.

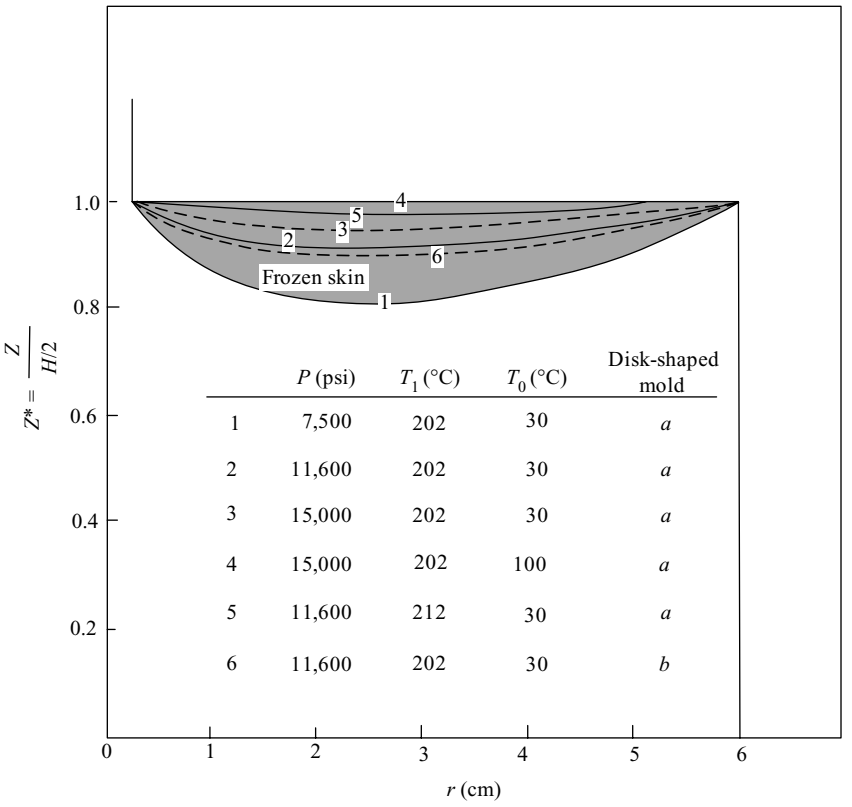

Fig. 13.12 Frozen skin profiles in two disk-shaped center-fed molds (*a*: $R = 6$ cm, $H = 0.5$ cm; *b*: $R = 6$ cm, $H = 0.3$ cm). Rigid (unplasticized) PVC was considered in the simulation. The frozen-skin region is defined by $T < 150°C$ (5). [Reprinted by permission from P. C. Wu, C. F. Huang, and C. G. Gogos, "Simulation of the Mold Filling Process," *Polym. Eng. Sci.*, **14**, 223 (1974).]

Figure 13.13 shows such a distribution measured by Menges and Wübken (30) for amorphous PS. They measured the shrinkage of microtomed molded samples at elevated temperatures. Figure 13.13(a) shows the longitudinal (flow direction) orientation distribution at two injection rates. The characteristic features of the orientation distribution are a maximum orientation at the wall that vanishes at the center with a local maximum near the wall. In Fig. 13.13(b), the longitudinal orientation at the wall and secondary maximum orientation are in close proximity, and the transverse orientation drops continuously from a maximum value at the surface.

Tadmor (29) suggested that both the orientation in the close neighborhood of the wall and the transverse orientation originate from the fountain-type flow (18) in the advancing front region, whereas the source of the orientation in much of the bulk of the material results by-and-large from the shear flow upstream from the front. Figure 13.14 shows a numerical simulation by Mavridis et al. (31) of the velocity field in the advancing front from a coordinate system moving at the average velocity, where the fountain flow is clearly visible.

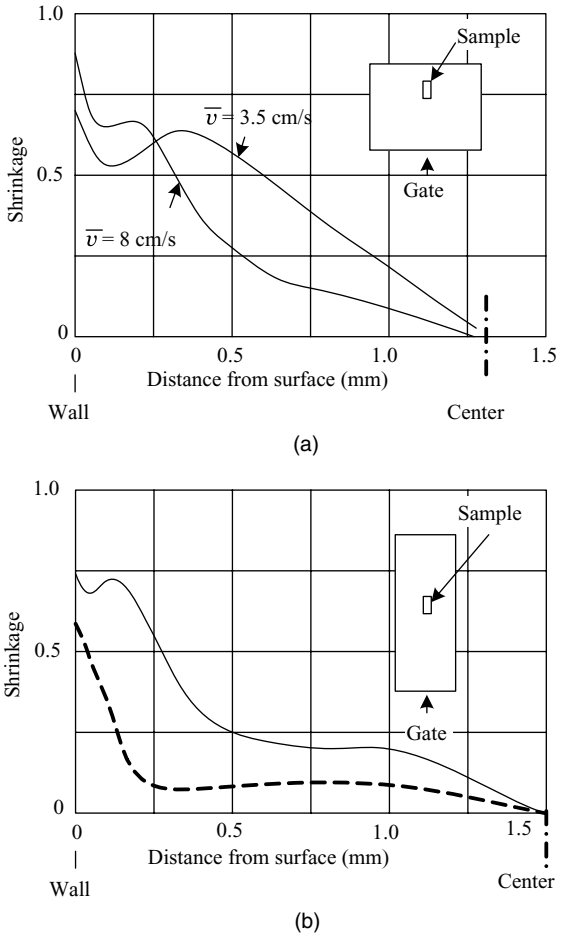

Fig. 13.13 Shrinkage distributions of injection molded amorphous PS (*a*) at two injection rates: longitudinal direction, (*b*) solid curves, longitudinal direction; broken curve, transverse direction. [Reprinted with permission from G. Menges and G. Wübken, "Influence of Processing Conditions on Molecular Orientation in Injection Molds," *Soc. Plastics Eng., 31st Annual Technical Conference*, Montreal, Canada, 1973.]

Figure 13.15 shows schematically the changing shape of a square-shaped fluid particle as it approaches the advancing front. It decelerates in the direction of flow and accelerates in the perpendicular direction. Thus, the fluid particles are stretched perpendicular to the direction of flow. By assuming a steady extensional flow in the y direction, Tadmor developed a semiquantitative model for the orientation distribution. The velocity profile in a coordinate system located on the advancing front and moving with it at the mean velocity $\langle v \rangle$, is $v_x = -\dot{\varepsilon}_{\text{pl}} x$, $v_y = \dot{\varepsilon}_{\text{pl}} y$, and $v_z = 0$, where $\dot{\varepsilon}_{\text{pl}}$ is the steady rate of elongation (this velocity profile also describes incompressible stagnation potential flow). The molecular orientation is a function of the *rate* of elongation, which can be estimated by assuming that the maximum velocity $v_{x,\max}$, upstream of the advancing front, drops to the mean front velocity $\langle v \rangle$ within a certain distance. Assuming this distance to be of the order of the gap

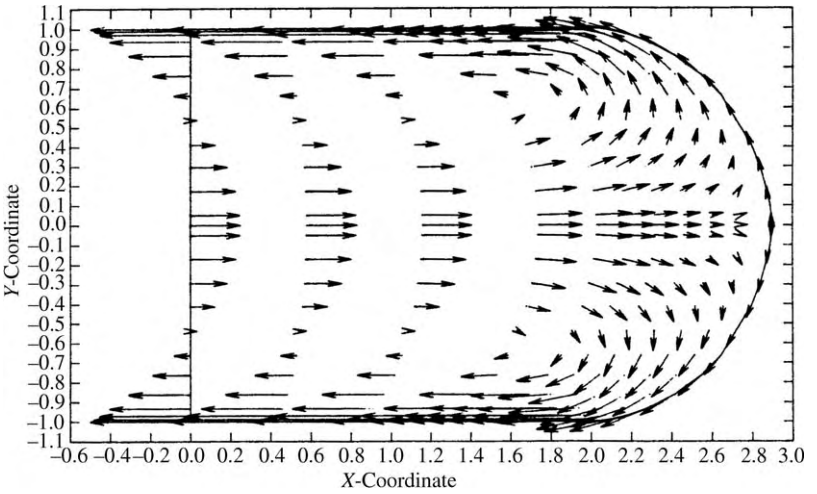

Fig. 13.14 Numerical simulation of the velocity field behind an advancing liquid front, moving at constant speed inside a two-dimensional channel. Calculations were carried out with a standard, general purpose FEM program. [Reprinted by permission from H. Mavridis, A. N. Hrymak and J. Vlachopoulos, "A Finite Element Simulation of the Fountain Flow," *Polym. Eng. Sci.*, **26**, 449 (1986).]

thickness, which is quite reasonable on the basis of Fig. 13.14, we obtain the following estimated rate of elongation:

$$\dot{\varepsilon}_{\text{pl}} = \frac{dv_y}{dy} = -\frac{dv_x}{dx} = \frac{\langle v \rangle - v_{\max}}{H} \tag{13.1-7}$$

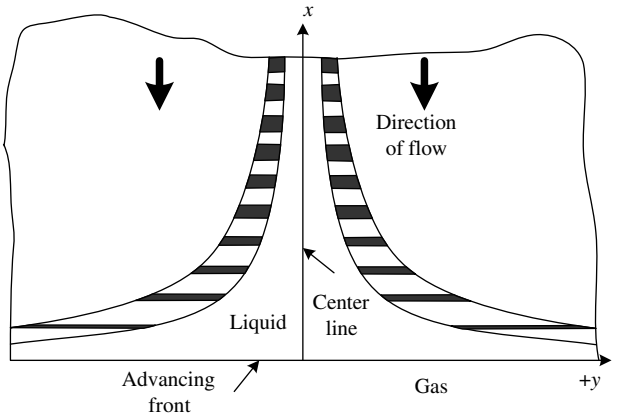

Fig. 13.15 Schematic representation of the flow pattern in the central portion of the advancing front between two parallel plates. The coordinate system moves in the x direction with the front velocity. Black rectangles denote the stretching deformation the fluid particles experience. [Reprinted by permission from Z. Tadmor, "Molecular Orientation in Injection Molding," *J. Appl. Polym. Sci.*, **18**, 1753 (1974).]

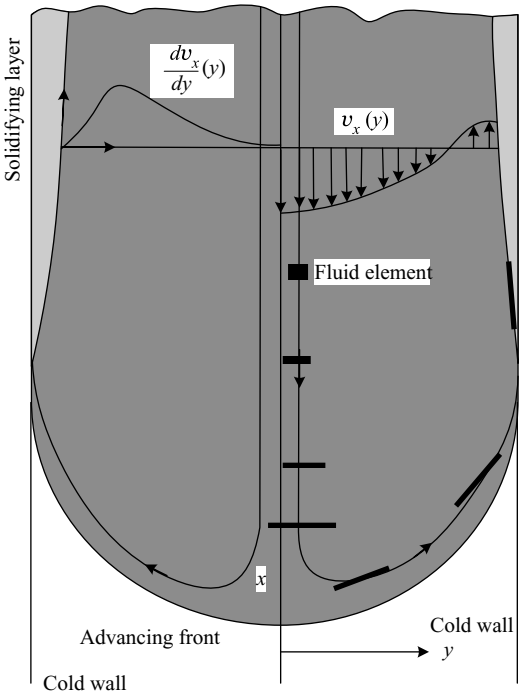

Fig. 13.16 Schematic representation of the flow pattern in the advancing front between two parallel cold walls. Black rectangles denote the stretching and orientation of a fluid particle approaching the central region of the front. The curved shape of the front causes fluid particles initially oriented in the y direction to end up on the wall, oriented in the x direction. The velocity profile upstream from the front is in the x direction and is viewed from a coordinate system located *on* the front. [Reprinted by permission from Z. Tadmor "Molecular Orientation in Injection Molding," *J. Appl. Polym. Sci.*, **18**, 1753 (1974).]

Note that $\langle v \rangle < 0$ and $v_{\max} < 0$, since they are in the negative x direction and hence, $\dot{\varepsilon}_{\text{pl}} > 0$. If $v_{\max}$ is taken from the fully developed flow of a Power Law model fluid between parallel plates, then

$$-\dot{\varepsilon}_{\text{pl}} = \left(\frac{n}{n+1}\right)\frac{\langle v \rangle}{H} \tag{13.1-8}$$

Clearly, according to this model the rate of elongation increases with injection rate, with decreasing gap and increasing n. Because the shape of the front is not flat but, as shown in Fig. 13.16, bends "backward" and becomes *tangent* to the walls at $y = \pm H/2$, the fluid elements that were oriented by the fountain flow in the y direction are deposited on the cold wall with an x-direction orientation.

Thus, as the result of the fountain type of flow, an oriented polymer layer originating from the central core of the advancing front and experiencing a steady elongation rate given in Eq. 13.1-8 is deposited on the cold wall of the mold, where it solidifies upon contact with the cold wall, retaining its elongational orientation. Molecular relaxation occurs further away from the surface into the skin layer, reducing this orientation. The

final orientation distribution in the skin layer will be a function of the cooling rate and the spectrum of relaxation times. The fountain-type flow mechanism and the orientation model just described suggest that in narrow-gap flow, skin-layer orientation is unidirectional in the direction of the front advances. If, however, the cross section of the flow is deep, the fountain-type flow leads to biaxial orientation, that is, orientation in the x-longitudinal and z-transverse directions.

Further away from the surface, the fully developed shear flow behind the front is responsible for any molecular orientation that may be present in the final product. Shear orientation, is a function of shear rate, which varies over the gap. As discussed earlier, in a fully developed flow in molds with cold walls, $\dot{\gamma}$ is almost zero in the immediate vicinity of the wall, exhibits a maximum *near* the wall, and is very low in the central core. Thus the initial shear orientation distribution at any particular location in the mold is approximately determined by the local shear-rate distribution at the moment of fill. Shear orientation therefore is unidirectional in the direction of flow. This initial shear orientation relaxes to various degrees, depending on the cooling rate and the relaxation spectrum. A complete orientation distribution can be approximately obtained by superimposing the elongational and shear orientations. The result, depending on the relative magnitude of the two orientation sources, may be complex, as is the case in Fig. 13.13(a). Alternatively, if the shear orientation is dominant, a maximum orientation is exhibited at a short distance from the wall where the shear rate was maximum. Clearly, the transverse orientation distribution [broken line in Fig. 13.13(b)] exhibits no secondary maximum, lending support to the assumption that it originates from the elongational type of flow in the advancing front. We should note that the relative significance of the orientation sources, as well as the detailed distribution, depend on polymer properties (ability to orient during and relax upon cessation of flow), injection conditions (filling rate, melt, and mold temperatures), and mold geometry.

Finally, by assuming that there is a quantitative relationship between shrinkage due to orientation and mean molecular end-to-end distance, following the framework of the previously described model, and assuming a bead-spring molecular model developed by Warner and Christiansen and Bird (32), Tadmor (29) obtained orientation distributions that, with a reasonable choice of parameters, agreed semiquantitatively with experimental measurements (30). The flow pattern and temperature distribution in the advancing melt, both in the bulk of the liquid and the frontal region, affect not only molecular orientation distribution, but are also frozen in strains and crystallinity distributions that have a decisive effect on the properties of the final product. Therefore, a great deal of work has been done on modeling such flows with Newtonian and non-Newtonian fluids.

Mavridis et al. (31), as previously pointed out, not only solved the flow pattern using FEM, but also dealt with the consequences of the deformation history experienced by the fluid elements on the frozen strains of injection molded parts. Dietz, et al. (33) demonstrated that birefringence measurements during and after filling can be useful in obtaining information about the filling flow kinematics. Birefringence measurements are related to the stress field through the stress optical law, $\Delta n = C\sigma$, where C is the ''universal'' stress optical coefficient for amorphous matter. The stress, in turn, is related to the flow kinematics by assuming the appropriate constitutive relations for flow and stress relaxation. Conversely, one can check the validity of assumed velocity fields and constitutive relations by comparing the predicted birefringence to that obtained by experiments.

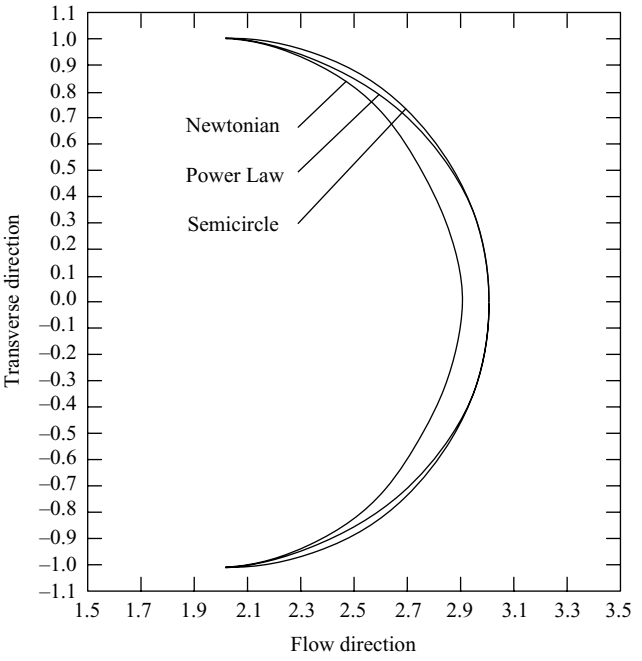

Fig. 13.17 Comparison of advancing front shapes for Newtonian and Power Law fluids (planar geometry). Power Law parameters: $m = 10{,}000\,\text{Pa}\cdot\text{s}^n$, $n = 0.5$, $\dot{\gamma}_w = 500\,\text{s}^{-1}$. [Reprinted by permission from H. Mavridis, A. N. Hrymak, and J. Vlachopoulos, ''A Finite Element Simulation of Fountain Flow,'' *Polym. Eng. Sci.*, **26**, 449 (1986).]

Gogos and Huang (34) and Huang (35) used the ''marker and cell'' method to investigate the melt front flow. Assuming isothermal Newtonian and Power Law fluid behavior, they obtained fountain-type flow patterns. Furthermore, their results are in good agreement with the experimental work of Schmidt (17) for nonisothermal flows, where V-shaped streaks of tracer polymer introduced at midplane were observed. Similar results were obtained by Friedrichs and Guçeri (36) using a hybrid three-dimensional and two-dimensional numerical technique to handle the three-dimensional advancing front flow and the Hele–Shaw flow behind it. Mavridis et al. (31), as pointed out earlier, used a finite-element methods (FEM) scheme developed by Mitsoulis and Vlachopoulos (37) to study the isothermal fountain flow of Newtonian and Power Law fluids. They followed the iterative method of Orr and Scriven (38) to find the location and shape of the melt front, and found that the difference between the calculated Newtonian and Power Law front shapes is small. As is seen in Fig. 13.17, the front is very close to a semicircle for Power Law fluids. Recently, Chung and Kwon (39) used a rigorous three-dimensional FEM analysis, utilizing the pseudoconcentration method at the advancing melt front capturing technique (40,41).

Figure 13.18 gives an example of the predicted flow field viewed from a reference frame moving with the velocity of the flow front for a center-gated disk mold. By this method, using a fiber-filled material, Dinh and Armstrong (42) succeeded in predicting fiber orientation distributions closer to the experimentally measured ones than those of assuming a Hele–Shaw flow throughout.

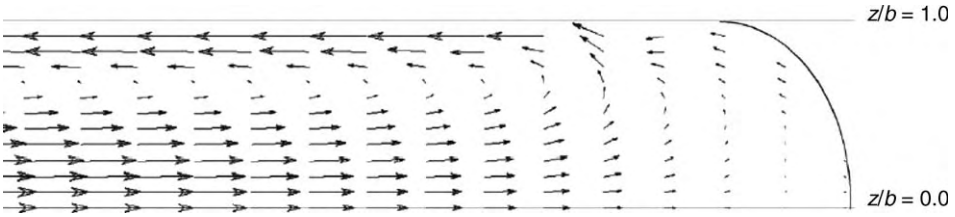

Fig. 13.18 Predicted velocity field showing fountain flow around the melt front region for non-Newtonian fiber suspension flow at about half the outer radius of the disk. The reference frame is moving with the average velocity of melt front, and the length of arrow is proportional to the magnitude of the velocity. The center corresponds to $z/b = 0$ and wall is $z/b = 1$, where z is the direction along the thickness and b is half-gap thickness. [Reprinted by permission from D. H. Chung and T. H. Kwon, "Numerical Studies of Fiber Suspensions in an Axisymmetric Radial Diverging Flow: The Effects of Modeling and Numerical Assumptions," *J. Non-Newt. Fluid Mech.*, **107**, 67–96 (2002).]

Extensive experimental and simulation investigations (43–45) consistently show that the rheological melt properties do not affect the shape of the advancing front, as indicated in Fig. 13.17. The reason for this may be attributed to conservation of mass, and not the momentum, governing the flow-front kinematics (46). Thus, the following fourth-order approximate expression (47) for the velocity field of an end-fed wide-slit mold with respect to an observer moving with the front velocity $v_x \neq (z)$ may be of general use for obtaining particle tracking information in the flow front domain, which is taken to be of length equal to the slit spacing H.

$$\frac{v_x}{\bar{v}_x} = -(0.5 - 6z^2/H^2) \times [1 - 1.45\exp(-5x/H)\sin(0.76 + 2x/H)] \qquad (13.1\text{-}9)$$
$$- 0.53(1 - 80z^4/H^4)\exp(-5x/H)\sin(2x/H)$$

$$\frac{v_z}{\bar{v}_x} = z/H(1 - 4z^2/H^2)[3.63\exp(-5x/H)\sin(0.76 + 2x/H)$$
$$- 1.45\exp(-5x/H)\cos(0.76 + 2x/H)] \qquad (13.1\text{-}10)$$
$$- 2z/H(1 - 16z^4/H^4)[1.32\exp(-5x/H)\sin(2x/H)$$

The dimensionless residence time is

$$\bar{t}_r = \frac{t_r \bar{v}_x}{H/2} \qquad (13.1\text{-}11)$$

with dimensions scaled with $H/2$, and is shown in Fig. 13.19. The folding point or plane is the dimensionless z_u position where, from the moving observer frame used, the velocity $v_x(z)$ can be considered negative.

Elucidating the flow pattern in the advancing front also helps to better understand the weld-line formation when two fronts collide. Figure 13.20 depicts the various stages of flow during weld line formation. When they meet, the two fronts are made of polymer molecules that are aligned with the front shape. Thus, they will meet tangentially. Following the first contact, a stagnation-type flow fills the two wedge-shaped regions next to the two mold walls. This flow further stretches the free boundaries of the two fronts and

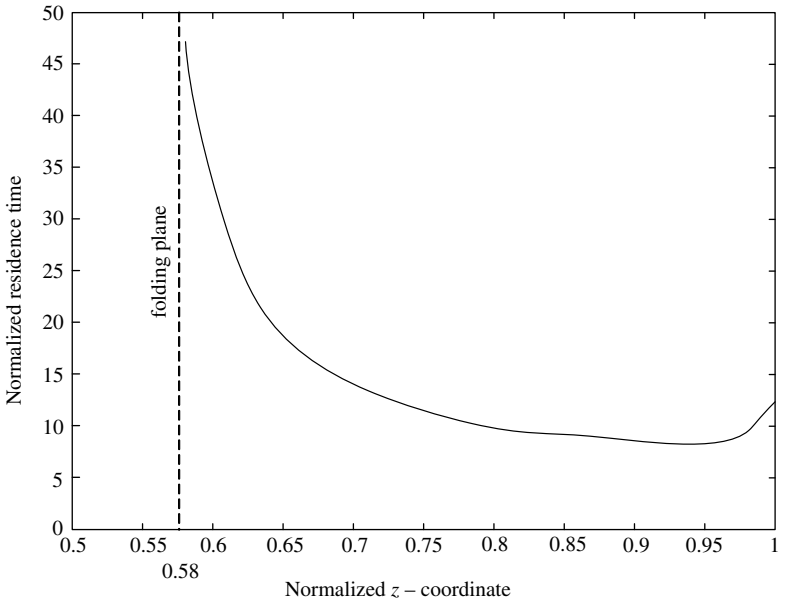

Fig. 13.19 Normalized residence time $(\bar{t}_r = t_r \bar{v}_x/(H/2))$ as a function of normalized position $(\bar{z}_u = z_u/(H/2))$, where a particle leaves the flow front domain; the dashed line indicates the position of the folding point. [Reprinted by permission from G. W. M. Peters, P. J. L. van der Velden, H. E. H. Meijer, and P. Schoone, "Multilayer Injection Molding," *Int. Polym. Process*., **9**, 258–265 (1994).]

has a tendency to resist the packing flow that is necessary to avoid small sink marks at the weld line.

Front Instabilities During mold filling flow instabilities, which apparently originate from the advancing front, may occur. Bogaerds et al. (47) reviewed flow instabilities that normally occur above a critical filling rate, treating them analytically and experimentally. The general nature of such instabilities are surface defects, characterized by shiny and dull bands periodically appearing and alternating from top to bottom surfaces. They are roughly perpendicular to the flow direction, as shown in Fig. 13.21. The defects are called *tiger stripes*, flow *marks*, or *ice lines*. Under any name, they limit the use of molded parts with such defects in unpainted products requiring uniform surface appearance, such as car bumpers. For homopolymers, such as PP, the dull bands appear in scanning electron micrographs (SEM) to have a striated topology of hills and valleys (48–50). Hamada and Tsunasawa (51) showed that in polymer blends such as polycarbonate/acrylonitrile-butadiene-styrene (PC/ABS), the shiny bands are PC-rich and the dull (cloudy) ones, ABS-rich. Furthermore, they found that in the shiny bands, the blend morphology indicated a symmetric flow pattern approaching the free surface. On the other hand, when the flow front passed through the region where the cloudy band was being formed, the flow pattern was not symmetric. Other investigators (49,50,52–54) have also concluded that the surface defects are due to *unstable flows in the fountain flow region*. The cause of such unstable fountain flows, shown schematically in Fig. 13.22, is most often thought to be *slip* at the wall. This unstable flow mechanism was first demonstrated experimentally by Rielly

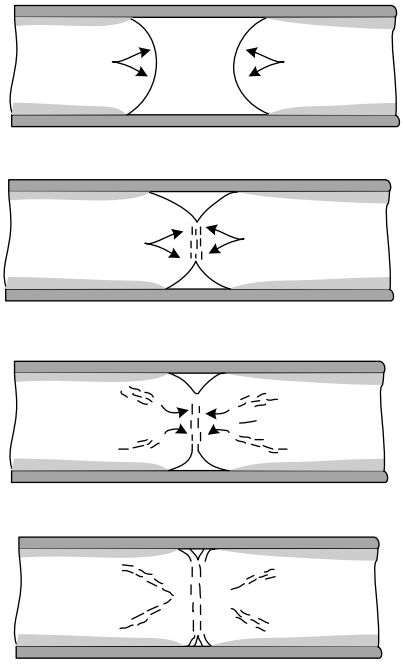

Fig. 13.20 Schematic representation of the impingement and the subsequent flows in the weld-line region: gray areas indicate cold regions of the melt; dashed lines denote regions undergoing extensional flow. [Reprinted by permission from S. Y. Hobbs, ''Some Observations on the Morphology and Fracture Characteristics of Knit Lines,'' *Polym. Eng. Sci*., **14**, 621 (1974).]

and Price (54) at high fill rates: when a small, red, oil/lubricant-based crayon mark was made on one of the flat mold surfaces, upon mold filling, a red transfer mark would appear on the *opposite wall downstream*, with progressively fainter red marks on alternating walls downstream as the mold was being filled. The wall-slip explanation for this phenomenon is based on the very low viscosity of the crayon, which causes a melt front *slip velocity* on

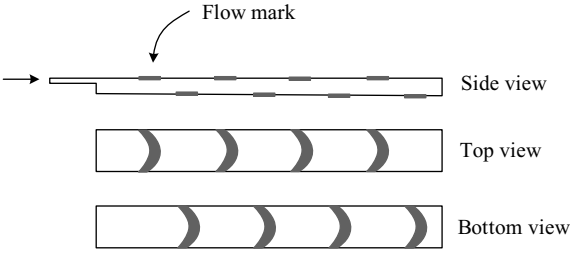

Fig. 13.21 Schematic representation of the surface defects that appear periodically and alternate in location on opposite sides of a flat mold. [Reprinted by permission from A. C. B. Bogaerds, G. W. M. Peters, and F. P. T. Baaijens, ''Tiger Stripes: Instabilities in Injection Molding,'' in *Polymer Processing Instabilities*, S. G. Hatzikiriakos, and K. B. Migler, Eds., Marcel Dekker, New York, 2005.]

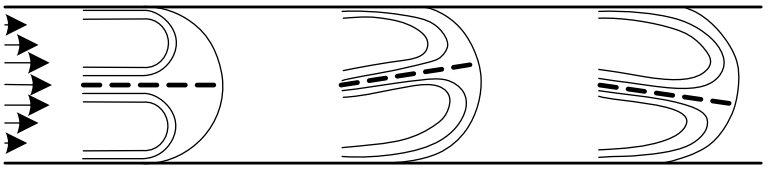

Fig. 13.22 Schematic representation of stable (left) and unstable (two right) fountain flows as causes of surface defects. [Reprinted by permission from A. C. B. Bogaerds, G. W. M. Peters, and F. P. T. Baaijens, ''Tiger Stripes: Instabilities in Injection Molding,'' in *Polymer Processing Instabilities*, S. G. Hatzikiriakos and K. B. Migler, Eds., Marcel Dekker, New York, 2005.]

one of the walls. Since the other side of the front *sticks* on the wall, it causes the slipping side to transfer to the opposite wall, transferring with it part of the crayon mark (55). Bulters and Schepens (48,49) used a two-color molding technique and high fill rates to obtain the short-shot flow patterns shown in Fig. 13.23. The black core melt, instead of becoming the surface layer on both walls, as would be expected in a symmetric fountain flow, is first swept to the bottom side and then flipped to the top.

Bogaerds et al. (47) developed a *linear* flow stability analysis ''toolbox'' in conjunction with the single-mode extended pom-pom (XPP) constitutive equation (56–58). Their analysis did not show the periodic nature of the flow-front motion observed experimentally with instabilities. On the other hand, their simulations do show that the onset of the linear instability can be postponed by increasing the number of the pom-pom–bearing arms of the XPP model, which would render in the melt increased, strain-hardening behavior.

Multicomponent Systems The flow kinematics of the multicomponent system is of considerable interest in molding. Vos et al. (59) used multilayer polymer tracers to study experimentally and to simulate the fountain and reverse fountain flows occurring in the driven and driving piston regions of the simple capillary experimental device shown in

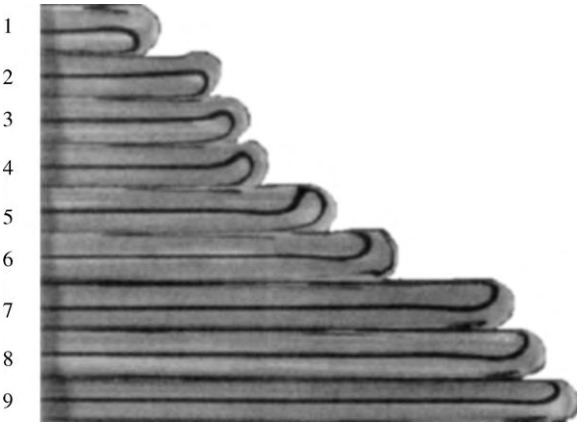

Fig. 13.23 Two-color, PP injection, high-rate mold-filling short shots documenting fountain flow instability. [Reprinted by permission from A. C. B. Bogaerds, G. W. M. Peters, and F. P. T. Baaijens, ''Tiger Stripes: Instabilities in Injection Molding,'' in *Polymer Processing Instabilities*, S. G. Hatzikiriakos and K. B. Migler, Eds., Marcel Dekker, New York, 2005.]

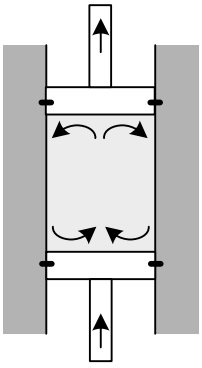

Fig. 13.24 Schematic representation of the fountain and reverse fountain flows at the driving and driven pistons.

Fig. 13.24. Solid cylindrical slices of the same polymer, but stacked in two alternating colors, as shown in Fig. 12.25 are heated and melted to 200°–260°C, causing them to flow in a circulatory pattern under the force of the driving piston $F_p - F_g$. The fountain and reverse fountain flows, with no slip at any of the three melt-containing walls, were studied for two polymer melts: Dow PS 634 and DMS ABS Ronfalin FX50. PS at 230°C is quasi-Newtonian for $\dot{\gamma} < 10\,\mathrm{s}^{-1}$, while ABS has a Power Law behavior even at $\dot{\gamma} = 10\,\mathrm{s}^{-1}$, as shown in Fig. 13.26. The ''marker'' layer deformations are *very* different for the two rheologically different polymers, as shown on Figs. 13.27 and 13.28. Furthermore, the agreement between experimental and simulation results, using the Carreau model for PS and a Bingham fluid model for ABS, is good. The shear-thinning nature of PS is exhibited both experimentally and computationally in Fig. 13.27. An FEM, variable mesh-density method was used with different boundary conditions, to account for leakage at the two piston corners. The pluglike flow behavior of ABS could be obtained computationally only

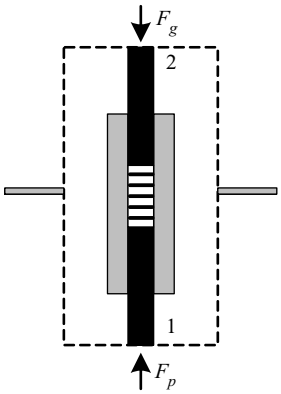

Fig. 13.25 Experimental setup on an apparatus for displacing a multilayered, two-color melt by the driving piston force ($F_p - F_g$). [Reprinted by permission from E. Vos, H. E. H. Meijer, and G. W. M. Peters, ''Multilayer Injection Molding,'' *Int. Polym. Process.*, **6**, 42–50 (1991).]

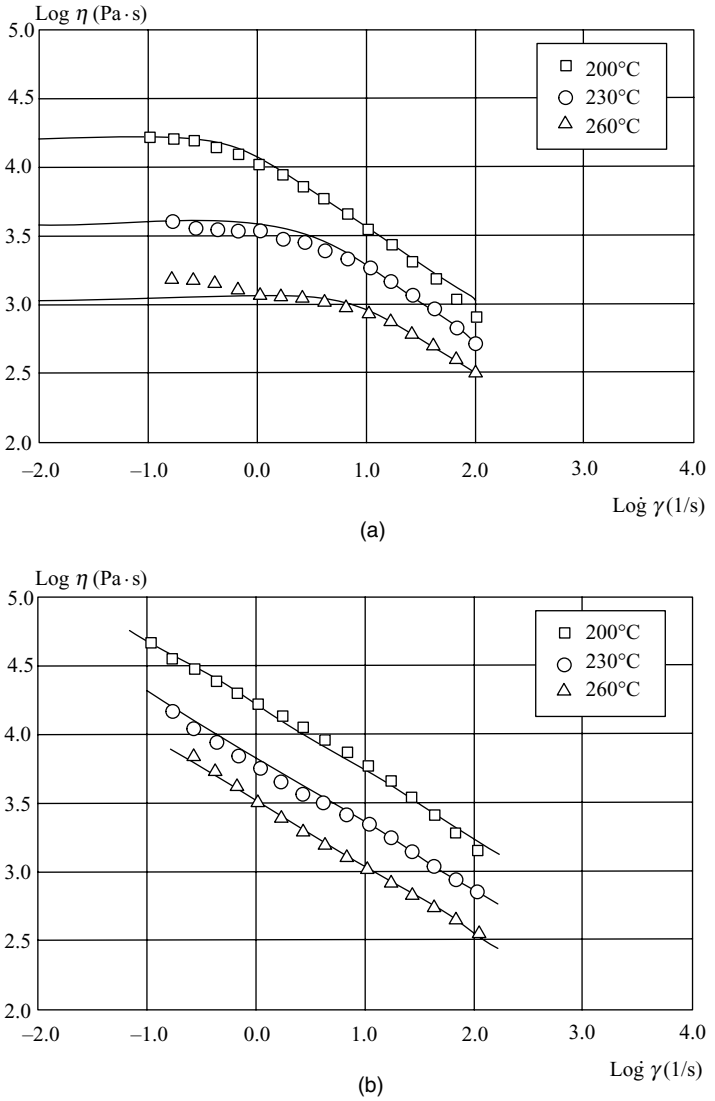

Fig. 13.26 Experimental flow curves for PS and ABS. Lines represent fits with a Carreau, for PS, and Power Law, for ABS, constitutive equations. [Reprinted by permission from E. Vos, H. E. H. Meijer, and G. W. M. Peters, "Multilayer Injection Molding," *Int. Polym. Process.*, **6**, 42 (1991).]

when a Bingham fluid is used, indicating the presence of yield behavior in the circulating flow inside the chamber. The Bingham fluid model used is

$$\eta = \eta_b \left[1 + \left(\frac{\tau_y}{\eta_b} \right) \dot{\gamma}^{-1} \right] \tag{13.1-12}$$

where τ_y is the yield stress and η_b is the viscosity at high shear rates.

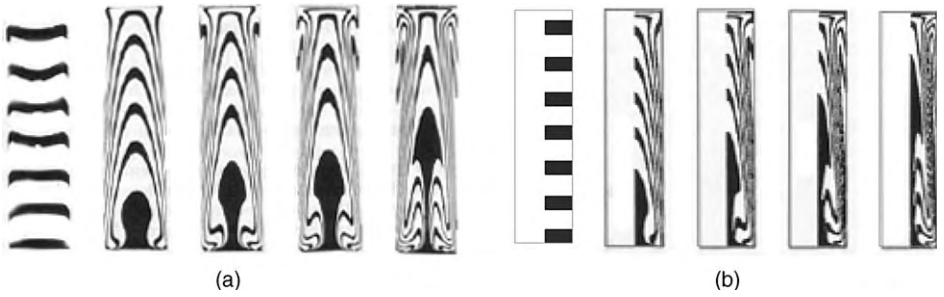

Fig. 13.27 Deformation of PS at different displacements: 0, 22, 33, 44, and 55 mm. (a) Experimental. (b) Calculated using the Carreau model ($T = 230°C$). [Reprinted by permission from E. Vos, H. E. H. Meijer, and G. W. M. Peters, ''Multilayer Injection Molding,'' *Int. Polym. Process*., **6**, 42 (1991).]

Peters et al. (46) incorporated particle tracking by means of labels into the FEM software program developed at Eindhoven University of Technology and used by Vos et al. (59), whose results were discussed previously. They simulated the coinjection process, where two different colors of the same polymer DuPont PA (Zytel 101 L N C-10) are sequentially injected into an end-gated mold with four ribs, shown in Fig. 13.29 (a). Since particle tracking provides the deformation history of every fluid element that enters the mold it enables the prediction of the occurrence and the location of the technologically important problem of ''layer breakthrough,'' where the second melt breaks through the first via the fountain flow, and ends up at the outer layer of the coinjection molded product, which is not acceptable for coinjection. The agreement between the simulated and experimentally obtained breakthrough regions for the rib mold in Fig. 13.29(a) is good, as shown in Fig. 13.29(b) and 13.29(c). Once again, the importance of the fountain flow is demonstrated.

Coinjection Molding

In 1967, Imperial Chemical Industries (ICI) developed the ''sandwich'' or coinjection molding process for producing structural foam products. In this process, the first melt is

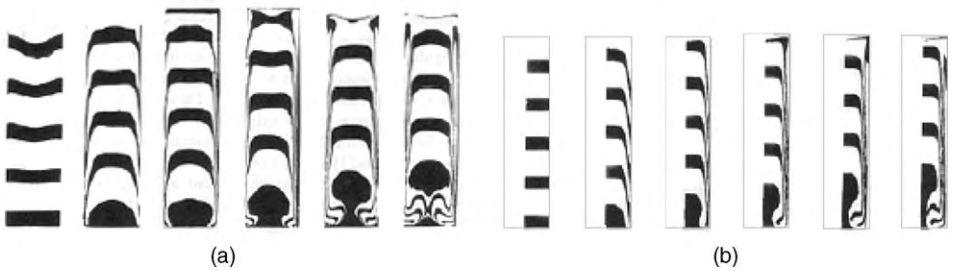

Fig. 13.28 Deformation of ABS at different piston displacements: 0, 11, 22, 33, 44, and 55 mm. (a) Experimental. (b) Calculated using a Bingham fluid model ($T = 230°C$). [Reprinted by permission from E. Vos, H. E. H. Meijer, and G. W. M. Peters, ''Multilayer Injection Molding,'' *Int. Polym. Process*., **6**, 42 (1991).]

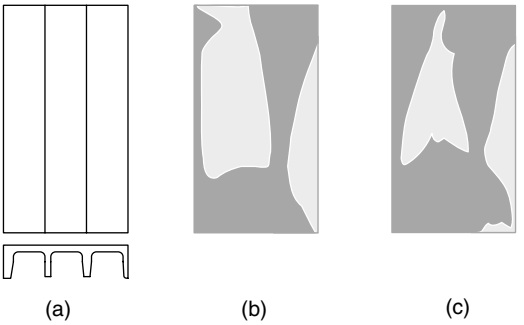

Fig. 13.29 (a) The four-ribbed, end-fed rectangular tray mold used by Peters et al. (46) for coinjection molding experiments and simulations; (b) numerically determined ''breakthrough'' areas by the second melt; (c) experimentally obtained ''breakthrough'' areas. [Reprinted by permission from G. W. M. Peters, P. J. L. van der Velden, H. E. H. Meijer, and P. Schoone ''Multilayer Injection Molding,'' *Int. Polym. Process.*, **9**, 258 (1994).]

injected into the mold until it fills it partway. At this point the second melt, which is the same polymer as the first, but contains a foaming agent, is injected behind the first, pushing its core forward and, because of the fountain flow, creating a skin made of the first melt. When the mold is filled and the polymers undergo cooling, the internal pressure is reduced and foaming takes place, resulting in the formation of a structural foam product—foamed core and solid skin. Before the gate freezes, the first polymer is injected again to purge the sprue of the second melt, in preparation for the next molding cycle. These sequential steps of the process are shown schematically in Fig. 13.30, where the changeover from one melt to the other is carried out by shifting a valve. Two melt-generating devices are needed. This can be achieved either with two injection molding machines or with two extruders feeding into the reservoir of a ram positive-displacement hydraulic injection unit. When utilizing hot runner molds, the two melt streams are directed into the mold via separate channels, which remain hot and separate until they reach the gate area, where they flow in a concentric nozzle arrangement similar to the common, machine-based coinjection process in Fig. 13.30. Coinjection molding has found application in ''green'' products where the second, foaming agent-containing melt is a recycled grade of the ''virgin'' melt. Two different polymers can be used in this process to take advantage of the following benefits: lower-cost parts, higher strength, reinforcing agent-containing core, sound absorbing core, and reduced cooling times, especially in thick parts, when the injection temperature of the core is lower. However, at least one of the two different polymers must contain a compatibilizing agent with the first in order to achieve interfacial bonding.

Gas-Assisted Injection Molding

The gas-assisted injection molding process involves the high-pressure injection of a gas into a partially filled mold. Under the gas pressure, the polymer *core* melt is driven downstream of the mold and, because of the fountain flow, a continuous melt skin is formed until the mold is filled. The result of this process is a product with a polymer skin and a gas core. In this process, the gas pressure is maintained while the polymer skin melt is cooling, transmitting the required packing pressure to the skin. Having gates that are not polymer filled, this process is more effective than the application of the packing melt

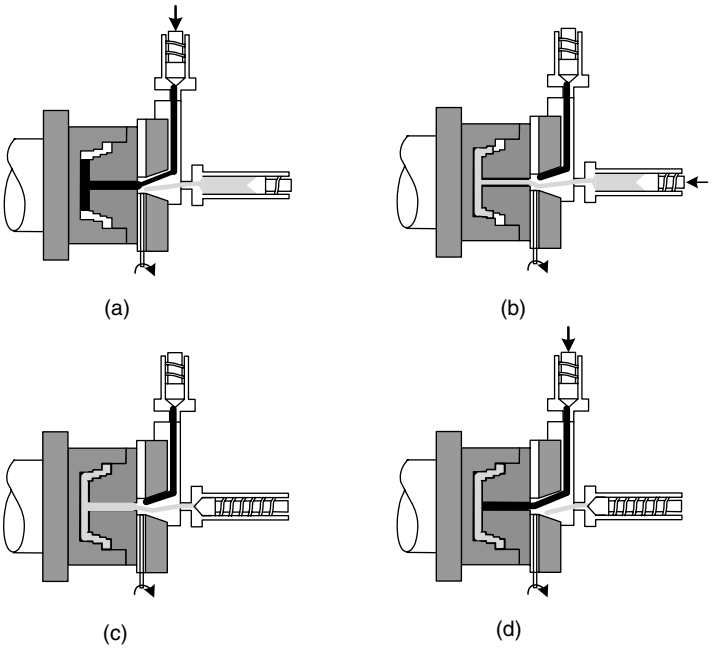

Fig. 13.30 Four stages of coinjection molding. (a) Short shot of skin polymer melt (shown in dark shade) is injected into the mold. (b) Injection of core polymer melt until cavity is nearly filled, as shown in (c). (d) Skin polymer is injected again, to purge the core polymer away from the sprue. [Reprinted by permission from Design Center, School of Engineering, Santa Clara University, Santa Clara, CA.]

pressure in conventional injection molding, especially for thick product parts, resulting in the absence of surface sink marks. Once the polymer skin has completely solidified, the gas pressure is released, the mold opened and the product ejected. The process stages are shown in Fig. 13.31. In visualizing and understanding the gas-assisted injection molding process, it is important to note that the *viscosity of the gas is immensely lower* than that of the polymer melt it is displacing, and that the gas is compressible. Thus, the pressure gradient in the gas core is zero, as it advances in the direction of the least resistance, which involves hot melt-containing thick part regions. As a result, this process yields more uniform polymer skins compared to those of coinjection-molding products, as shown schematically in Fig. 13.32. Other consequence of the use of compressed gas include a more uniform packing pressure distribution, a reduction in injection and packing pressures, and reduction of the molding cycle due to shorter required cooling times. Because of these advantageous consequences, gas-assisted injection molding allows for forming of thick products, which is technologically very significant. On the other hand, low injection and packing pressures may result in limited reproduction of textured mold surfaces, in surface marks due to the incompressible melt to compressible gas switchover, and, finally, uncontrolled gas penetration.

The problem of gas-assisted displacement of Newtonian fluids along capillaries was first examined by Fairbrother and Stubbs (60). Later, Marchessault and Mason (61) measured the coating thickness after gas penetration $(R_0 - R_b)$ as well as the ''fractional

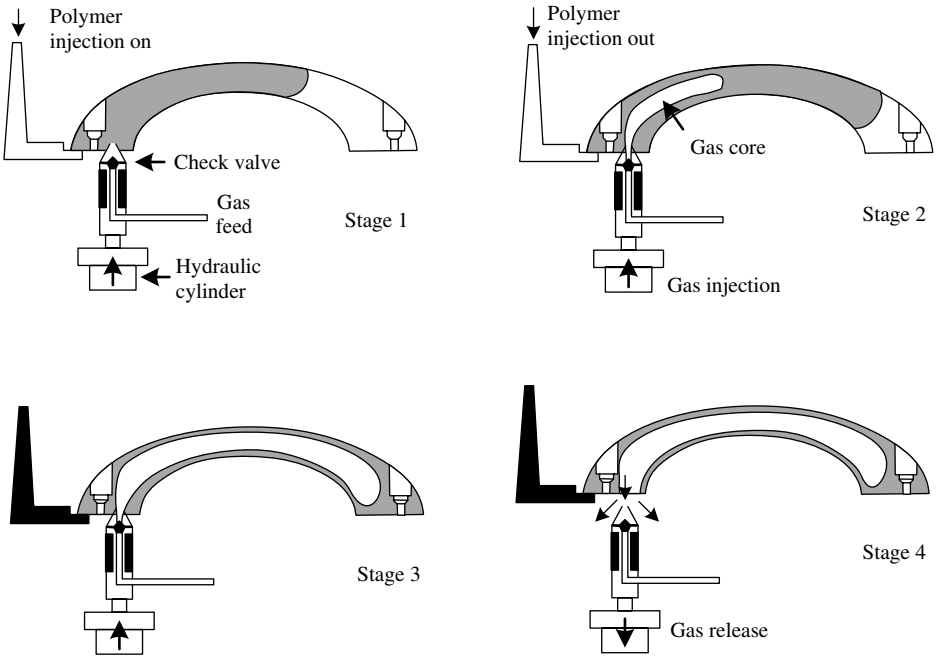

Fig. 13.31 Schematic representation of the stages of the gas-assisted injection molding process for a container handle.

coverage,'' defined as

$$m = \frac{(R_0^2 - R_b^2)}{R_0^2} \tag{13.1-13}$$

where R_0 and R_b are the capillary wall and the fluid-bubble radii. Their experiments were expanded by Taylor (62) who examined a large number of Newtonian fluids in the capillary number region $10^{-3} < \mathrm{Ca} < 1.9$, where

$$\mathrm{Ca} = U_b \mu / \Gamma \tag{13.1-14}$$

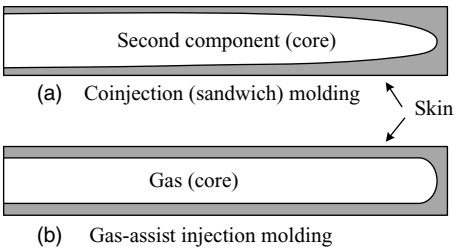

Fig. 13.32 Schematic comparison of the skin thickness distributions in co- and gas-assisted injection molded parts due to the negligible gas viscosity.

where U_b is the constant bubble velocity used in the experiments, μ is the Newtonian viscosity, and Γ is the gas–liquid interfacial tension. Ca is the ratio of the viscous forces driving the creation of new interfacial surface to that of the resisting surface tension. In the absence of gravitational contributions, that is, the Bond number $\mathrm{Bo} = \rho g R_0^2/\Gamma \ll 1$, the Ca number is the only controlling dimensionless number. This is what Taylor and later Cox (63) found experimentally: a single curve of fractional coverage, m, versus Ca was obtained for a variety of Newtonian fluids and capillary radii, reaching an asymptote of $m = 0.6$ at $\mathrm{Ca} > 10$. Westborg and Hassager (64) used a Galerkin formulation to solve the problem of a Newtonian fluid by a gas bubble for the region $10^{-2} < \mathrm{Ca} < 1$ and compared their results with those of Fairbrother and Stubbs (60) and Taylor (62). The agreement was quite good.

Turning to the problem of the penetration of long gas bubbles in tubes with non-Newtonian fluids, a physical situation that is more akin to gas-assisted injection molding, Poslinski et al. (65,66) concluded both experimentally and through FEM computational work with shear thinning fluids, that the fractional coverage, m, has asymptotic values lower than those of Newtonian fluids, and that the asymptote is lower with lower Power Law index fluids. Finally, Huzyak and Koelling (67), and Gauri and Koelling (68) were the first to investigate, both through thorough experiments, including particle tracking velocimetry (PTV), and FEM (POLYFLOW) simulations, the effect of the viscoelasticity on the coating thickness and fractional coverage, m, during displacement of melts by long gas bubbles for the wide range of the capillary number $10^{-2} < \mathrm{Ca} < 10^2$. For Newtonian fluids, their experimental and POLYFLOW simulation work predictions coincide with the experimental results of Taylor (62), as shown in Fig. 13.33.

The simulation results are shown in Fig. 13.34 for the Newtonian, Amoco Polybutene (PB) H-100 of weight average molecular weight $\bar{\mathrm{M}}_\mathrm{w} = 10^3$ and a constant viscosity up to $10\,\mathrm{s}^{-1}$ of $19\,\mathrm{Pa}\cdot\mathrm{s}$. The fluid flow in the liquid being displaced by the gas bubble is viewed from a Lagrangian perpective, where the bubble is stationary and the tube wall is

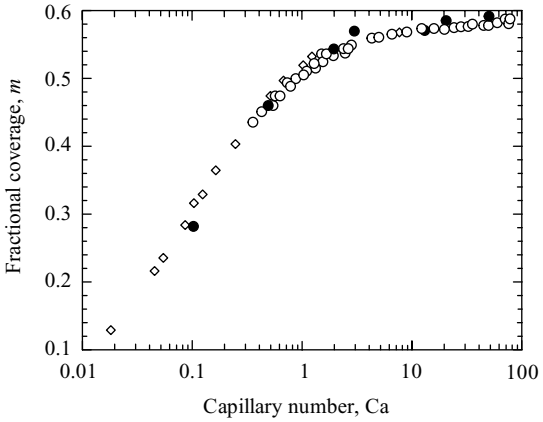

Fig. 13.33 Fractional coverage predicted by simulations (solid circles) in comparison with the experiments of Taylor (62) (open diamond) and Hyzyak and Koelling (67). [Reprinted by permission from V. Gauri and K. W. Koelling, "Gas-assisted Displacement of Viscoelastic Fluids: Flow Dynamics at the Bubble Front," *J. Non-Newt. Fluid Mech.*, **83**, 183–203 (1999).]

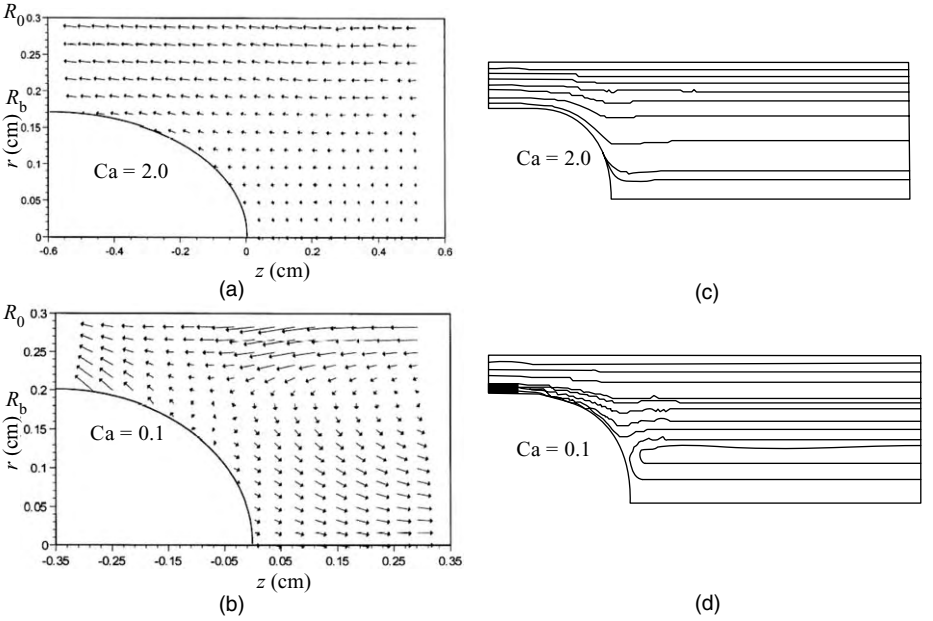

Fig. 13.34 Velocity vectors from PTV experiments with the Newtonian PB H-100. (a) Ca = 2.0; (b) Ca = 0.1; FEM POLYFLOW streamlines for the same fluid; (c) Ca = 2.0; (d) Ca = 0.1. [Reprinted by permission from V. Gauri and K. W. Koelling, "Gas-assisted Displacement of Viscoelastic Fluids: Flow Dynamics at the Bubble Front," *J. Non-Newt. Fluid Mech.*, **83**, 183–203 (1999).]

moving backwards with the bubble advance velocity. At the free surface, the interfacial tension is $2.95 \times 10^{-2}\,\mathrm{Nm}^{-1}$ for PB H-100 and $2.41\,\mathrm{Nm}^{-1}$ for the Boger fluid, discussed later. The pressure-related, normal force is an imposed process variable at the free surface. A reverse fountain-like flow in front of the advancing bubble (the frame of reference) is observed at low Ca, while a bypass flow is observed with stagnant layers near the bubble apex at higher Ca values. The shear ratios in front of the bubble are in the range of $0–0.75\,\mathrm{s}^{-1}$.

Hyzyak and Koelling (67), and Gauri and Koelling (68) used a Boger fluid to study the effects of viscoelasticity. The fluid is 31 wt % Exxon Vistanex L-120 of $\mathrm{M_w} = 1.2 \times 10^6$ in a Newtonian solvent of 95 wt % Amoco PB H-100 and 5 wt % tetradecane. It exhibits a constant viscosity of 12.5 Pa · s and a nonzero, first normal stress coefficient, Ψ_1. That is, it is Newtonian and at the same time elastic and can be modeled with a four-mode Giesekus constitutive equation (69). The velocity vectors obtained are similar to those of Newtonian fluids. On the other hand, the fractional coverages, both experimentally and computationally, are increasing with increasing De, and are 30% higher than the Newtonian at De = 4, as shown in Fig. 13.35

For the Boger fluid $\mathrm{De} = \lambda\dot{\gamma}_w$, $\lambda = \Psi_1(w)/2\mu$, $\dot{\gamma}$ is the shear rate and the subscript (w) denotes the fluid shear rate at the fluid–bubble interface. The increase in the fractional coverage for Boger fluids at De > 1 was attributed to their elastic nature, in particular their extensional flow thickening. Higher De values are obtained at high imposed capillary numbers, that is, higher U_b. Under such conditions, the computed flow, close to the stagnation point at the centerline, right behind the bubble, is purely extensional, with a

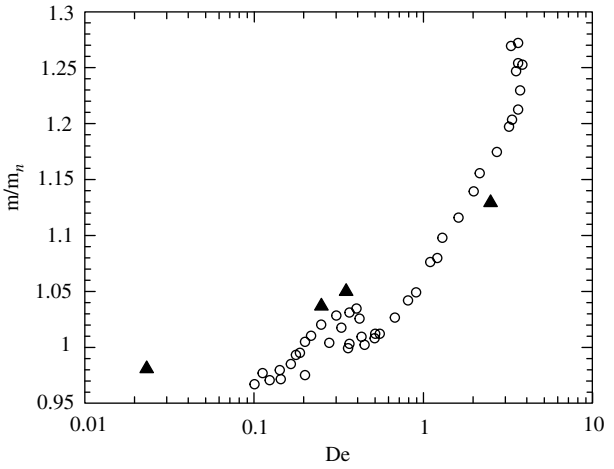

Fig. 13.35 Fractional coverage results for the Boger fluids (open circles) compared to experiments (solid triangles). [Reprinted by permission from V. Gauri and K. W. Koelling, ''Gas-assisted Displacement of Viscoelastic Fluids: Flow Dynamics at the Bubble Front,'' *J. Non-Newt. Fluid Mech*., **83**, 183–203 (1999).]

value of the Giesekus parameter (69) $R = 1$. This parameter is

$$R = \frac{\dot{\gamma} - \omega}{\dot{\gamma} + \omega} \tag{13.1-15}$$

where $\dot{\gamma}$ and ω are the scalar local shear rate and vorticity, respectively.

Koelling et al. (70) conducted nonisothermal, pressurized gas-bubble Newtonian fluid-displacement experiments. The fluid used was PB H-300. It was injected into a capillary tube maintained at 60°C. The tube was then transferred in a different temperature bath at 0°C. The penetrating gas was then injected after different delay times, t. The longer the delay time, the deeper the cooling penetration thickness will be, since it is dependent on the Fourier number,

$$\mathrm{F_0} = \frac{\alpha t}{R_0^2} \tag{13.1-16}$$

where α is the thermal diffusivity of the fluid.

The hydrodynamic fractional coverage for the 60° to 0°C switchover under various $\mathrm{F_0}$ values is shown in Fig. 13.36. It is to be noted that, even at $\mathrm{F_0} = 0$, the fluid is being cooled during gas penetration. This explains why m is close to, but higher than, the isothermal $m = 0.6$ value. The increase in m with increasing $\mathrm{F_0}$ continues, since the cooler and the more viscous the fluid layers near the wall are, the more difficult the displacement would be, so the bubble advances through a narrowed, cylindrical, hotter melt passage. A maximum is reached as $\mathrm{F_0}$ is further increased and m approaches the isothermal $m = 0.6$ at $\mathrm{F_0} \sim 1.0$, when an almost uniform 0°C fluid temperature is established. That is, the experimental conditions revert back to isothermal simulations, and are capable of predicting the results shown in Fig. 13.36, once the activation energy for flow, which is

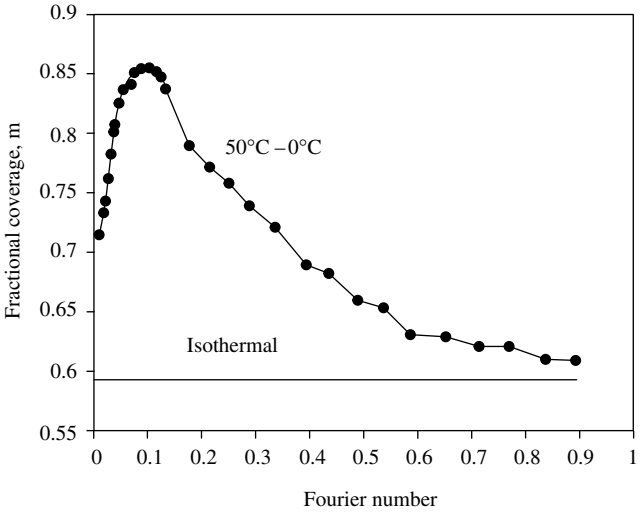

Fig. 13.36 The fractional coverage during nonisothermal gas-penetration experiments in PB-300, where the gas was injected after different $F_0 = \alpha t/R_0^2$, that is, dimensionless delay times, following the step bath temperature switchover from 60° to 0°C. [Reprinted by permission from K. W. Koelling, V. Gauri, M. Tendulkar, R. Kaminski, and O. Becker, "Understanding the Controlling Mechanisms of Gas-assisted Injection Molding through Visualization," *SPE ANTEC Tech Papers*, **43**, 3697 (1997).]

$\Delta H/R = 8.525\,\mathrm{K}^{-1}$ for PB H-300, is known. Finally, we note that the nonisothermal temperature profiles here exist only in the absence of a phase transition, which occurs in the gas-assisted injection-molding process, at least with semicrystalline polymers.

The Overall Flow Pattern

The most characteristic feature of injection molds is geometrical complexity. In such molds there is a need to predict overall flow pattern, which provides information on the sequence in which different portions of the mold fill, as well as on short shots, weld line location, and orientation distribution. The more complex a mold, the greater this need is. The irregular complexity of the geometry, which forms the boundary conditions of the flow problem, leads naturally to FEMs, which are inherently appropriate for handling complex boundary conditions.

In principle, the pressure, velocity, and temperature distribution can be determined by such methods. The problem, however, can be greatly simplified by restricting the flow to the narrow-gap type of configurations in which locally fully developed flow can be assumed at any instant of time. Many molded articles have a generally thin-walled structure where such an analysis is relevant. The FEM formulation of the two-dimensional narrow-gap flow problem would closely follow that of anisotropic seepage problems analyzed by Zienkiewicz et al. (71). A simple lattice-type FEM formulation called *flow analysis network* (FAN) was suggested for this problem by Broyer et al. (72), assuming isothermal non-Newtonian flow. Krueger and Tadmor (6) simulated with this model the filling of rectangular molds with inserts (Fig. 13.8). A computational grid of 18 × 72 was used. The time-dependent gate pressure used in the simulations were based on the

experimental pressure traces at location P_3 (Fig. 13.5), neglecting the pressure drop from the gate outlet to this location. The temperature was also measured at the same location, and its mean value was used in the simulations. Figure 13.8(a) plots simulation results. Calculated advancing front profiles are marked by $\times$ symbols (sudden jumps in values are the result of the rather coarse grid size) labeled by corresponding filling times. Experimental front profiles obtained by short shots are denoted by solid lines, and experimental (visually observable) weld line locations by dotted lines. The agreement between predicted and measured front profiles is surprisingly good, considering the restrictive isothermal flow assumption in the model and the possible front distortion in short shots. The theoretical model does not account for side-wall effects, which clearly appear to restrict flow in the experimental profile. Reasonable agreement was also obtained in predicting mold filling times (6). The good prediction of the advancing front profiles indicates that no large melt temperature drop occurred during filling under the conditions used, and suggests that theoretical prediction of orientation distribution and weld-line locations may be possible.

Finally, simulation studies indicate that the overall flow pattern and the front shapes are only weak functions of the viscous nature of the liquids used; Newtonian liquids exhibit almost the same front patterns as pseudoplastic melts. Such behavior is implied by the results of Example 13.1. This finding was supported experimentally by studies that utilized high-speed movie photography during the injection of low viscosity Newtonian fluids in a transparent mold (6). The implications of such findings are twofold: from a modeling point of view we can use at first approximation a simple Newtonian constitutive equation to predict the position of the advancing front and its shape. Moreover, we can also study filling patterns of very complex molds with low viscosity Newtonian fluids in transparent molds experimentally with reasonable accuracy. Of course, filling times and pressures are highly dependent on the rheological properties of the melt used. For a more reliable and accurate simulation, there are complete simulation packages for mold filling that can be of great value in the process of mold design and exploration of operating conditions on the process. Example 13.2 shows some results with one such package, MoldFlow^{TM}.

Cooling of the Molded Part

Melt cooling takes place from the start of the injection-molding cycle; that is, because, with the exception of the case of hot runner molding, the entire mold is near room temperature. We saw earlier that during filling temperature gradients appear in both the flow and transverse directions, and a ''frozen skin'' develops whose average thickness decreases with increasing entering melt temperature and injection rate. At the end of the filling stage, cooling of the melt is the predominant phenomenon. However, because of the resulting specific volume decrease, a small amount of melt must be ''packed'' into the mold to compensate. Furthermore, if the injection pressure is removed before the gate freezes (or in the absence of a one-way valve), backflow can occur because of the prevailing high pressure in the mold cavity. Finally, during cooling, minor secondary flows occur, which, being at a relatively low temperature, may result in appreciable macromolecular orientation. These flows are triggered by temperature gradients, causing the melt to flow from the hot region to the cold to compensate for the volume contraction. Thus, secondary flows are expected to occur in regions of abrupt decreases in the cross-sectional dimension. Whenever such flows are *not* possible, usually due to lack of material, voids are formed in the bulk of the molded article. From an overall point of view, the

TABLE 13.1 The Equation of State of Spencer and Gilmore and the Experimental Data

$$(P+\pi)(\hat{V}-\omega)=RT$$

where $\hat{V}=\hat{V}(T,P)$ is the specific volume, π = "internal pressure," ω = specific volume at 0 K, R = material constant.

Polymer	R (psi · cm^3/g K)	ω (cm^3/g)	π (psi)
PS (atactic)	11.60	0.822	27.000
PMMA (Lucite HM 140)	12.05	0.734*	31.300
PE (du Pont P1000 PM1)	43.00	0.875*	47.600

*Values uncertain owing to lack of reliable values of equilibrium densities

necessary requirement for avoiding void formation is that the mass of the polymer injected is greater than or equal to the product of the atmospheric density times the cavity volume.

In specifying the transport equations that simulate the cooling and solidification of molded parts, we neglect the packing, back flow, and secondary flows that take place during that stage of molding and contribute convectively to the heat transfer. Kuo and Kamal (73) have simulated cavity packing for the following two cases: fast flows that end in rapid decelerations, and negligible thermal contractions during packing and slow-filling flows, where deceleration is negligible but thermal contractions are controlling. In both cases, the equation of state of Spencer and Gilmore (Table 13.1) was used. For an end-fed rectangular mold cavity of a small thickness compared to the other two dimensions, we expect temperature gradients in the flow and thickness direction at the end of the filling, such as those in Fig. 13.10. Thus, for a cavity such as that in Fig. 13.7, the energy equation describing mold cooling is

$$\rho C_p \frac{\partial T}{\partial t}=k\left[\frac{\partial^2 T}{\partial y^2}+\frac{\partial^2 T}{\partial x^2}\right] \tag{13.1-17}$$

The temperature field at the end of filling is taken as the initial condition for the preceding equation. The boundary conditions are (where l is the mold length)

$$\left.\begin{aligned}
\left(\frac{\partial T}{\partial y}\right)(0,x,t)&=0\\
\left(\frac{\partial T}{\partial y}\right)\left(\frac{H}{2},x,t\right)&=-\frac{h}{k}\left[T\left(\frac{H}{2},x,t\right)-T_0\right]\\
\left(\frac{\partial T}{\partial y}\right)(y,0,t)&=-\frac{h}{k}[T(y,0,t)-T_0]\\
\left(\frac{\partial T}{\partial y}\right)(y,l,t)&=-\frac{h}{k}[T(y,l,t)-T_0]
\end{aligned}\right\} \tag{13.1-18}$$

This problem can be solved numerically for the case of constant thermophysical properties.

The next section discusses the solution and its results in covering reactive molding. As Chapter 5 discussed, the solution of solidification with crystallization can be treated by stating Eq. 13.1-17 twice, once for the melt and once for the polycrystalline solid, taking into account the heat released during the first-order transition by a thermal balance at the interface. Alternatively, Eq.13.1-17 can be used for both phases if C_p, ρ, and k are allowed to vary continuously over the entire temperature range. Finally, the conduction in the direction of flow can be neglected, since the gradients in that direction are, in general, smaller than the transverse gradients. In this case, the term $k\partial^2 T/\partial x^2$ is zero, and only the first two boundary conditions of Eq. 13.1-18 have to be used.

Injection Molding Structuring

There is a broad potential of structuring in injection molding, because the flow field in filling the mold is rapid and complex and can be varied by varying the process variables. Furthermore, the heat transfer can be fast and efficient, at least for the molecules near the surfaces of the mold. In other words, the probability of freezing molecular orientation brought about by flow is high near the surface layers and low near the core, enabling the formation of the sandwich type of structure.

From our earlier discussion in this chapter we expect to have the following macromolecular orientation, starting from the center of the thickness and proceeding outward: (a) near the center, no orientation at all because the shear velocity gradients are zero; (b) moving away from the center, an increasing amount of shear flow orientation due to the shear gradients that pass through a maximum value, and due to the faster cooling as we approach the wall; (c) near the wall, we expect only some shear flow orientation (shear gradients are low), in addition to some extensional flow orientation due to the fountain flow; and (d) in the wall region, only extensional flow orientation, due to the fountain effect. Although there is no question that shear flow occurs during filling, experimental evidence must be brought forth in support of the fountain flow, since it is so important to the resulting morphology.

We cite two experimental investigations, one by Schmidt (17) and the other by Thamm (74). In Schmidt's work, colored tracer particles, which entered the mold at the center of the mold thickness while the mold was partly filled, were found deposited at the mold walls at a later time, and at an axial distance beyond that of the front at the time of the tracer entrance (the approximate locations of such particles on the mold wall were predicted by Huang (35) who simulated the melt front flow region problem during filling). Thamm, investigating the morphology of injection molded blends of PP and ethylene-propylene-diene terpolymer (EPDM), found that near the mold surface, the EPDM profiles are either elongated for flat narrow molds or disk shaped for more squarelike molds. The EPDM particles in this case act as deformable tracer particles. Thus, from Schmidt's work we see that center particles catch up with the surface and flow to the wall, and from Thamm's evidence, we can deduce that the flow is either that of simple extension for narrow flat molds, or biaxial extension for square molds. Figure 13.37 demonstrates the extensional nature of the front region flow as the EPDM ''tracer'' particles are deformed on either side of the weld line. In light of this, the crystalline morphology reported by Kantz, Newman, and Stigale (75), Clark (76), and others can be understood fairly clearly. At the surface layer row, nuclei are formed by chains aligned in the direction of flow (extensional flow) on which lamellae grow in

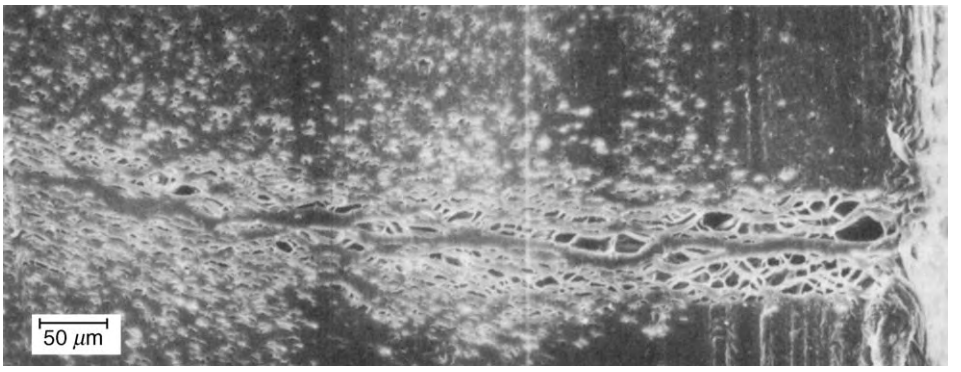

Fig. 13.37 Scanning electron photomicrograph of a weld line formed during the injection molding of a polypropylene–15% EPDM blend. Surface is hexane-extracted to remove EPDM. [Reprinted by permission from, R. C. Thamm, *Rubber Chem. Technol.*, **50**, 24 (1977).]

the plane perpendicular to the filling direction. At the layer just below, row nucleation still persists, but there the lamellae are perpendicular to the mold surface, but randomly oriented with respect to the filling direction. Shear flow orientation in combination with the prevailing temperature gradients is probably responsible for this morphology. Recall that both shear and elongational flows are capable of producing chain orientation that is intense enough to create row nucleation. Spherulitic morphology, indicative of little or no orientation, is observed in the core region. Figure 13.38 shows such variation of crystalline morphology with thickness. Similar morphologies have been reported by Hobbs (77) at and behind weld lines. This is expected in light of our previous discussion. We note in passing that if nucleating agents were added, the effect of row nuclei would be masked by profuse nucleation on the surfaces of the nucleating agents. Furthermore, the spherulitic core morphology would be grainy. The desirability of adding nucleating agents depends on the mechanical properties that are sought.

For amorphous polymers, the skin will be oriented, thus ductile, whereas the core region, being unoriented, will be brittle. Furthermore, the mechanical properties will be anisotropic, since the orientation is predominant in the filling direction. This anisotropy can be overcome for cup-shaped injection-molded articles. The male part of the mold can be rotated during filling, giving rise to additional orientation in the θ direction. This double orientation has been termed *helicoidal* by Cleereman (78), who suggested the process. Figure 13.39 illustrates the resulting impact strength.

For decades now, a great deal of work has been conducted in studying injection molding, both from the mathematical simulation and structuring-morphology points of view. The stage seems to be set for the next step forward, namely, the complete prediction of the properties of any given injection molded product, given the macromolecular specification of the polymer and the design and operating conditions used in molding it. This is the ultimate goal of polymer processing: to combine the power of computational continuum mechanics and molecular dynamics packages with powerful, molecular theory–based constitutive equations, equations of state and crystallization rates, and

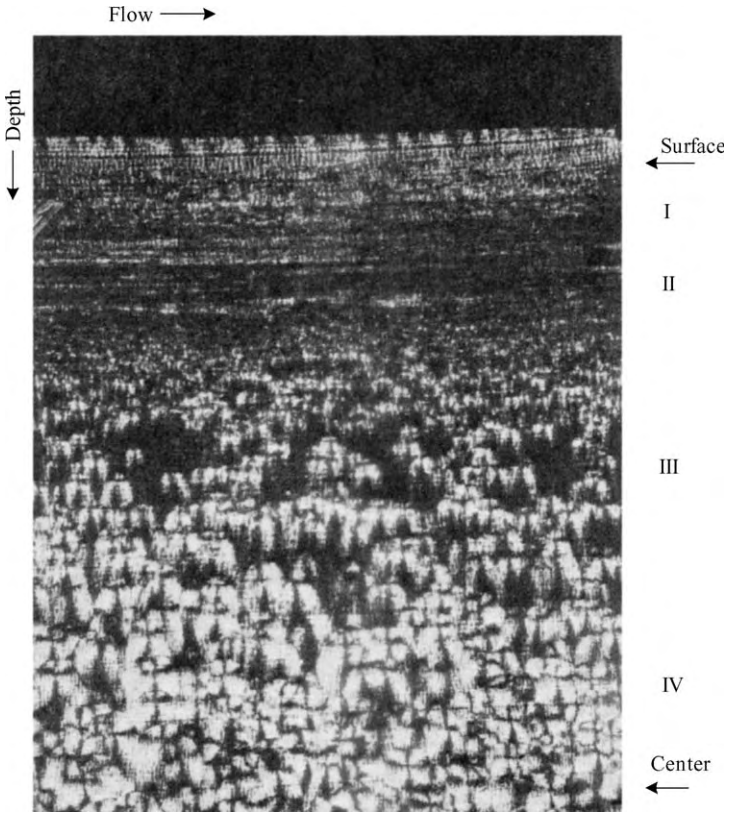

Fig. 13.38 Birefringence microscopy study of a cross section of molded HDPE, depicting various morphological regions. [Reprinted by permission from V. Tan, paper presented at the International Conference on Polymer Processing, MIT, Cambridge, MA, August 1977.]

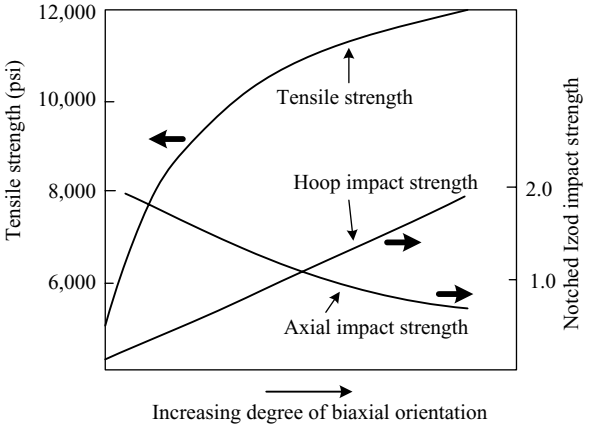

Fig. 13.39 Mechanical properties of biaxially (helicoidally) oriented PS. [Reprinted by permission from K. J. Cleereman, "Injection Molding of Shapes of Rotational Symmetry with Multiaxial Orientation," *Soc. Plast. Eng. J.*, **23**, 43 (1967).]

morphology theories, to arrive at an a priori specification of molded product properties. Once this is achieved, polymer processing will be equally adept both in process and product scientific design and engineering. For the time being, however, this goal has not yet been reached. Nevertheless, as discussed in Section 1.4, we can find important progress being made in this direction in the intense and focused multidisciplinary macromolecular engineering research, which is being carried out at several leading universities and research centers.

Computer Simulation Package Analysis

Example 13.2 Simulation of Mold Filling Using the MoldFlow™ Simulation Package We have previously described the various elements of the mold filling process, beginning with the hot melt flow through the sprue, runner, and gate into the cold mold. The details of the flow in an advancing front were discussed, as well as the way this front fills the mold and determines molecular orientation and the weld lines, and finally the cooling process. As in the case of plasticating extrusion, where the conveying, melting, mixing, and pumping of solids take place partly sequentially and partly concurrently, and which requires a complete computer simulation package to describe the process as a whole (Section 9.3), in injection molding we also need a complete computer simulation package to describe the entire process. In this Example, we present simulation with the MoldFlow™ Simulation Package.

Figure E13.2a shows the geometry of a tray that is to be molded from DuPont Zytel® 101F DAM PA66 and injected at 290°C into 90°C mold. The gate is located at the bottom center of the mold. The computations were carried out with 34×28 elements. Some of the computed parameters are given in the following table and meshing in Fig. E13.2b:

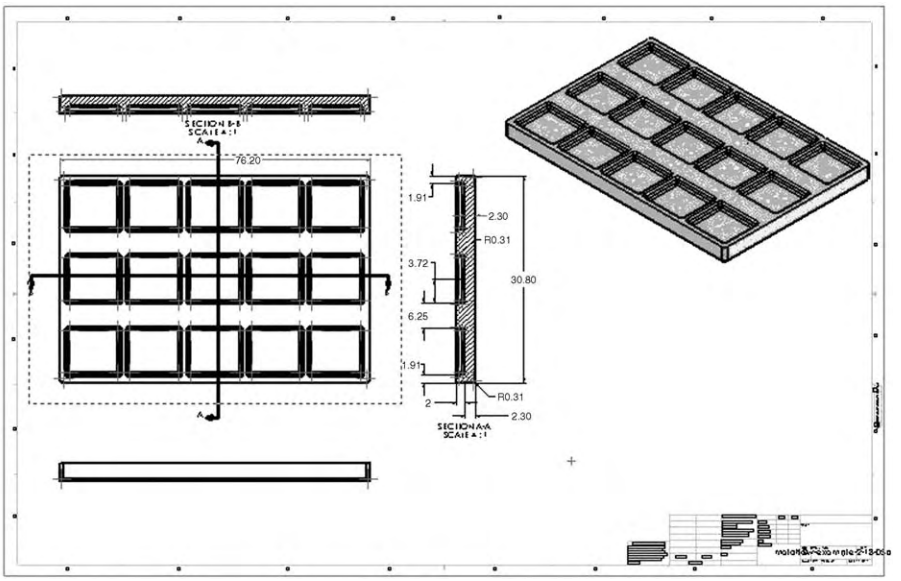

Fig. E13.2a A fifteen-compartment flat tray with wall thickness of 2.5 mm.

Injection time (s)	1.0
Nominal flow rate (cm^3/s)	12.8
Packing pressure profile (MPa) Duration (s),	
0	0.9
10	0.9
Cooling Time (s)	20.0
Total volume of the part and cold runners (cm^3)	12.8
Switchover pressure (MPa)	1.2

The results of the simulation are shown in Figs. E13.2c to E13.2m. By using color coding the designer gets an immediate and in-depth view of the whole process, which would be very difficult if not impossible to get from a numerical output. Indeed, in modern computerized fluid mechanics the visual representation plays a key role in studying a problem and is an inherent part of the solution. The vast amount of detailed data that can be obtained from the simulation of a complex process cannot be absorbed without appropriate visual two- or three-dimensional representation.

Figure E13.2c shows the fill time. As expected in this center-gated mold, the center region fills up first and the outer edges last, by a factor of 2:1.

Figures E13.2d and E13.2e show the melt front and bulk temperature distribution.

Figure E13.2f plots the pressure profile at the injection location.

The next two figures, Figs. E13.2g and E13.2h, show the thickness of the fraction of frozen layer, and regions of trapped air. Both are important for designing a good mold.

Figure E13.2i shows the average velocity at the end of fill, which determines, to a large extent, core orientation [E13.2j], whereas skin orientation, as discussed earlier, is determined by the normal of the advancing front shown in Fig. E13.2k.

Finally, Fig. E13.2l shows the recommended ram speed, and Fig E13.2m shows the weld-line locations.

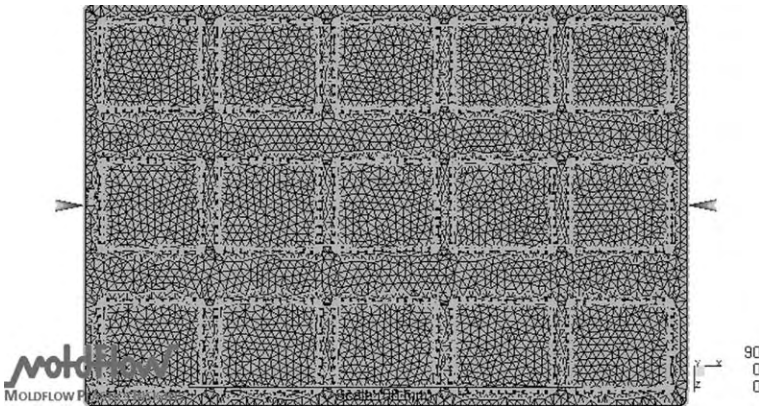

Fig. E13.2b The FEM cells generated by the program for the simulation.

13.2 REACTIVE INJECTION MOLDING

Injection molding has been used to form objects ranging in weight from a fraction of a gram to several kilograms. As the size of the article to be molded increases, two problems arise in injection molding: (a) generating enough homogeneous melt in the injection molding machine, and (b) maintaining sufficient clamping pressure to keep the mold closed during the filling and packing stages of the injection molding operation. The latter problem becomes serious when the projected area of the molded part is large and requires enormous mold presses.

The reaction injection molding (RIM) process was developed to bypass both of these problems. In this process, two or more low viscosity, 0.1–1.0-Pa · s liquid streams, which react when brought together, are mixed prior to being injected into large cavities (79). Some of the polymerization reaction (which may result in linear, branched, or cross-linked polymers) occurs during the filling stage. The bulk of the reaction, however, takes place after filling and even after removal from the hot mold. Thus, the injection pressures needed for filling molds in the RIM process are generally small. As the polymerization proceeds after filling, heat is generated by the reaction, which increases the specific volume of the polymer system. On the other hand, a specific volume decrease of the order of 10% accompanies polymerization. Thus, packing flows would be necessary, which would require high pressures, since the viscosity of the reacting system increases with increasing molecular weight or degree of cross-linking. To eliminate the necessity of packing, a small amount of a foaming agent is introduced into one of the streams. The resulting foaming action ensures that the RIM article will conform to the shape of the cavity. In this way, very large and complex-shaped cavities can be formed using a rather small injection pressure, of the order of 1–10 MN/m^2, and small clamping presses with inexpensive molds.

Obviously a key to the success of the RIM process has to be economically fast rates of polymerization. Otherwise the process is not competitive to injection molding, but comparable to casting. It follows, then, that not all polymer systems are good candidates for the RIM process. The most commonly used polymer system since the commercial inception of the process in the early 1970s is that of linear and cross-linked polyurethanes, where di- or trialcohols and di- or tri-isocyanates are the two main reacting species. Fiber-filled polyesters also have been used. Other systems used include polyureas, nylon 6 (ring opening), polyesters, polyacrylamides, and epoxies. Table 13.2 lists the principal differences between the injection molding and the RIM processes.

Since RIM involves reaction between miscible reactants, the process equipment must provide for: (a) fine control of the temperature of both reactant streams, (b) very accurate stoichiometric metering of the reactants, and (c) nearly instantaneous intimate mixing of the reactants within a ‘‘mixhead’’ prior to being delivered to the hot mold. Figure 13.40 is a schematic representation of the polyurethane RIM process. Jacketed and stirred isocyanate and polyol tanks with gas dispersed in them keep the reactants at process temperature. Low-pressure pumps recirculate both streams (see right tank) between the delivery piping and the tanks. Heat exchangers keep the reactants in the pipe channels at process temperatures so that, when the valves to the two metering cylinders are opened, both reactants are at process temperature. When the cylinders are filled, the reactants undergo high-pressure (rate) recirculation until they are directed to the mixhead, where they

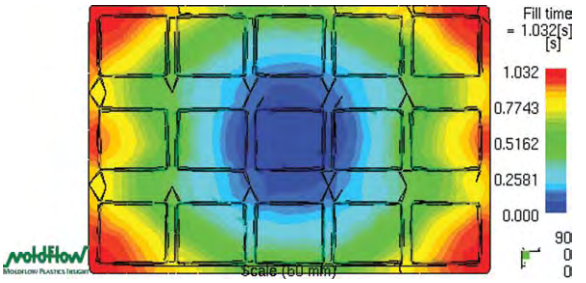

Fig. E13.2c Fill time.

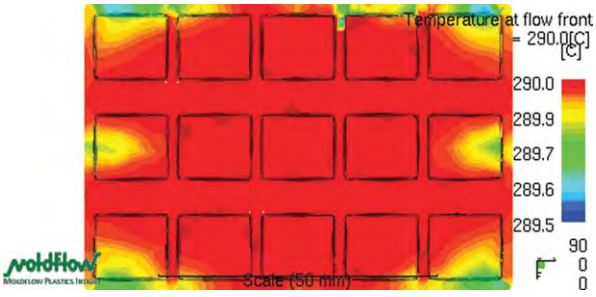

Fig. E13.2d Temperature at flow front.

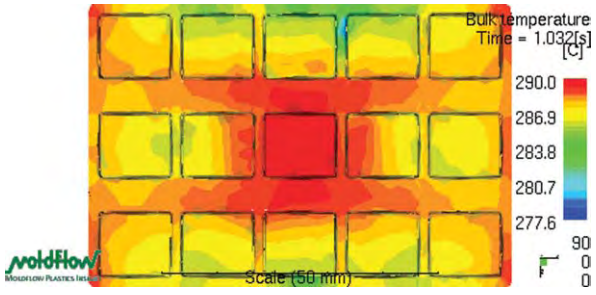

Fig. E13.2e Bulk temperature.

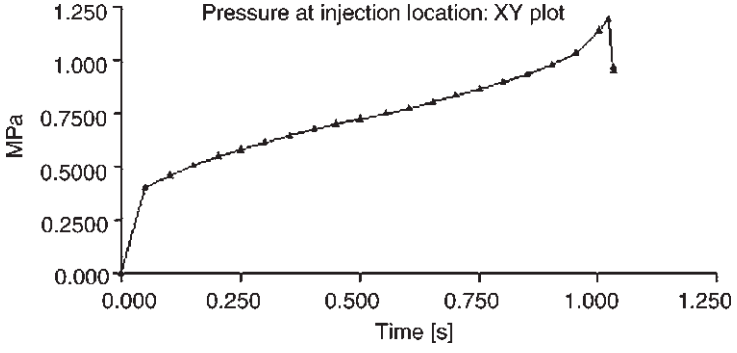

Fig. E13.2f Pressure at injection location.

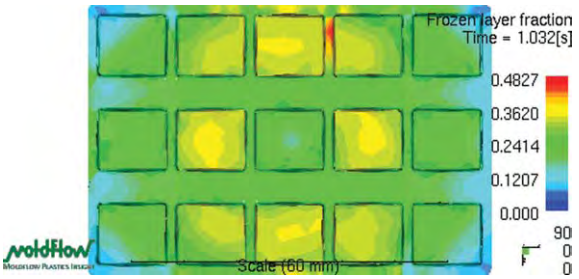

Fig. E13.2g The fraction of frozen layer at the end of injection.

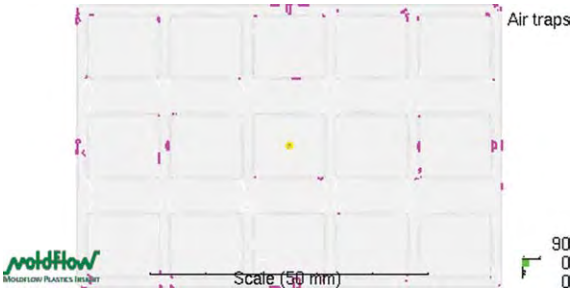

Fig. E13.2h Air traps locations.

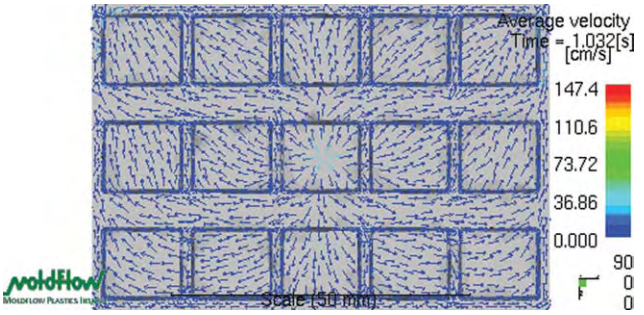

Fig. E13.2i Average velocity at the end of fill.

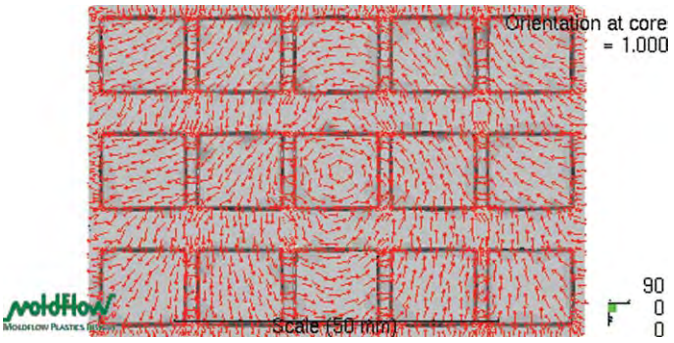

Fig. E13.2j Core orientations.

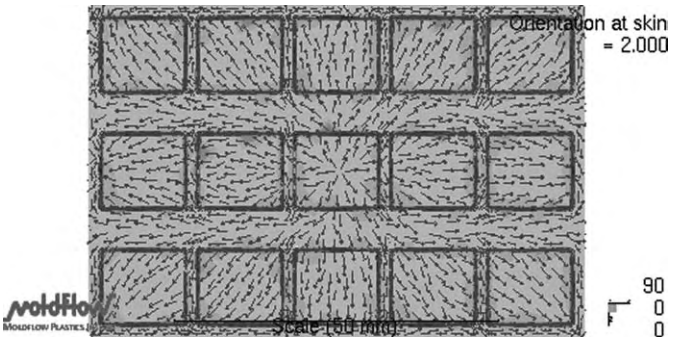

Fig. E13.2k Skin orientation..

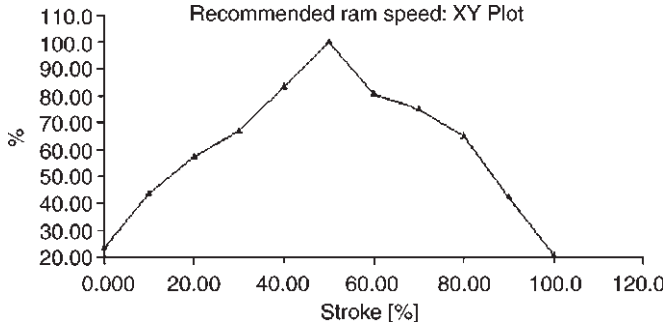

Fig. E13.2l Recommended ram speed..

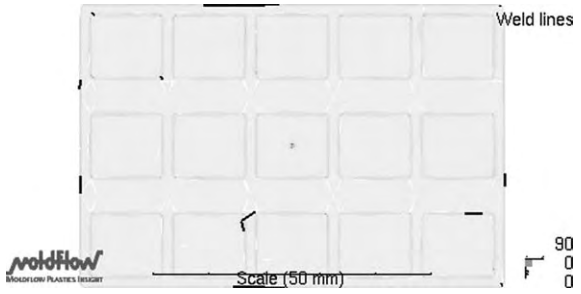

Fig. E13.2m Weld line location..

TABLE 13.2 Comparison between Typical RIM and Thermoplastic Injection Molding (TIM)[*]

	RIM	TIM
Temperature		
reactants	40°C	200°C
mold	70°C	25°C
Material viscosity	1 Pa · s	10^2–10^4 Pa · s
Injection pressure	100 bar	1000 bar
Clamping force (for 1 m^2 surface part)	50 ton	3000 ton

[*]C. W. Macosko, *RIM Fundamentals of Reaction Injection Molding*, Hanser, Munich, 1989.

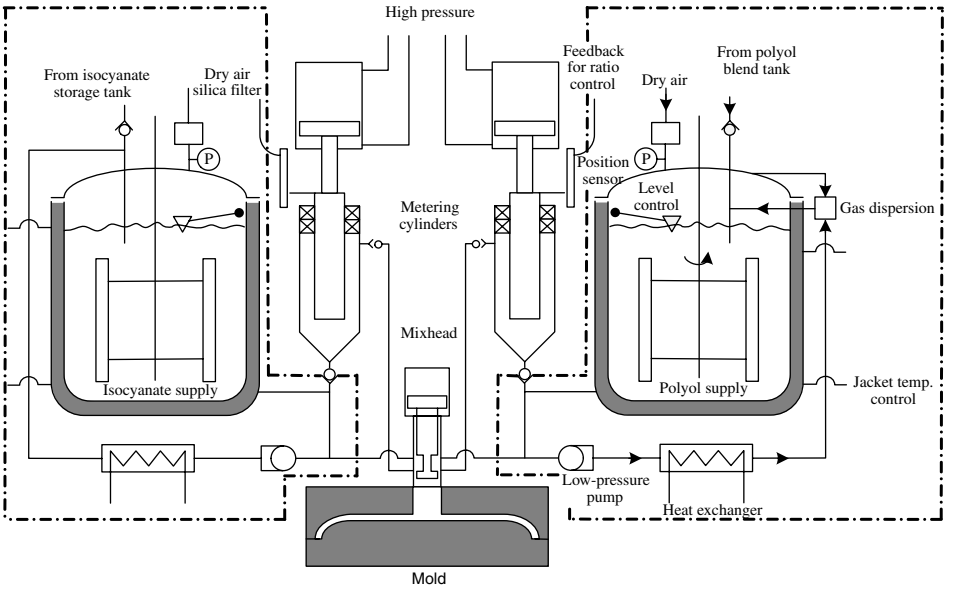

Fig. 13.40 Schematic representation of a typical RIM machine. The machine can be divided into three basic parts: (1) low-pressure recirculation or conditioning (bounded by the dotted lines); (2) high-pressure metering; and (3) the impingement mixhead. The mold is usually considered separately. The figure shows the machine in low-pressure recycle mode. [Reprinted by permission from C. W. Macosko, *RIM Fundamentals of Reaction Injection Molding*, Hanser, Munich, 1989.]

undergo impingement mixing, which is capable of creating very small striation thicknesses. Consequently, the ratio of the characteristic diffusion times $t_d = \bar{r}^2 / \mathscr{D}_{AB}$ is smaller than the characteristic reaction time of the particular polyurethane reactants used at process temperature, $t_r = ([c]/\dot{r})|_0$, where $[c]$ is reactive species concentration, and $\dot{r}$ is the rate of reaction, both at $t = 0$. The impingement mixing and self-cleaning features of a mixhead are shown in Fig. 13.41 (80,81)

The success of high velocity jet impingement mixing in reducing the striation thickness of the impinging reactant streams from 1–3 mm to about 100 μm nearly instantaneously, and within a very small volume and readily cleanable mixhead, has been the key to the development of RIM. With a striation thickness of 100 μm, the reactant diffusivity required for good diffusional mixing in one second, is $\mathscr{D}_{AB} = 10^{-4}\,\text{cm}^2/\text{s}$. The mixed reactants flow out of the small mixhead chamber into the mold through a runner and gate. Impingement mixing with RIM reactants was first studied by Menges et al. (81) and later by Malguarnera et al. (82,83), by Macosko and Suh (84), Lee and Macosko (85), and Lee et al. (86). The studies are experimental, with dimensional analysis of the results. Tucker and Suh (87) took the fine-scale features of the reactants in the mixhead, l_m, to be of the same order as the scale of turbulence given by the Kolmogoroff microscale, l_k

$$l_k \sim (\nu^3 P_m)^{1/4} \tag{13.2-1}$$

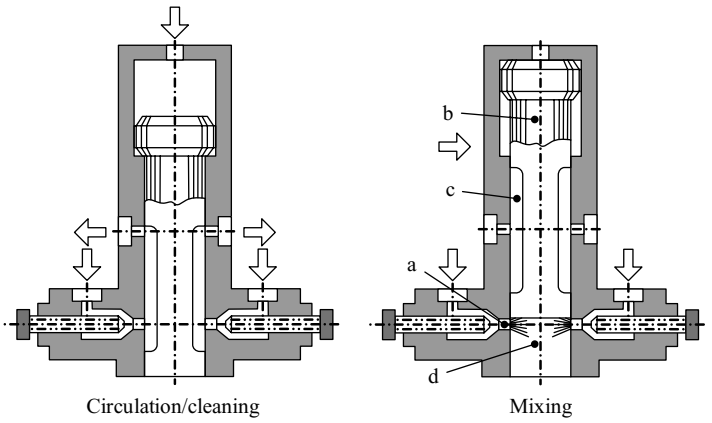

Fig. 13.41 The Keuerleber and Pahl (1970) mixhead. In the closed or recirculation position, reactants recirculate through grooves (c) along the cylindrical cleanout piston (b). In the open position, reactants flow at high velocity through circular orifices (a), impinge in the chamber (d), and flow out to the mold cavity (diagram from G. Oertel, 1985 (80)). [Reprinted by permission from C. W. Macosko, *RIM Fundamentals of Reaction Injection Molding*, Hanser, Munich, 1989.]

where $v = \mu/\rho$ is the reactant kinematic viscosity and P_m is the rate of turbulent energy dissipation:

$$P_m \sim V^3/D \tag{13.2-2}$$

where V is the average reactant jet velocity in the nozzles leading to the mixhead and D is the nozzle diameter. Thus, noting $l_m \sim l_k$ one obtains

$$l_m/D \sim [v^3/V^3D^3]^{1/4} \tag{13.2-3}$$

or

$$l_m/D \sim \mathrm{Re}^{-3/4} \tag{13.2-4}$$

Experimentally it has been found that the $\mathrm{Re}_{\mathrm{crit}}$ for impingement mixing for onset of turbulence is around 140. This value seems to be insensitive to the impinging jet angle of incidence (82). Furthermore, the $\mathrm{Re}^{-3/4}$ dependence seems to hold until the range $140 < \mathrm{Re} < 250 \sim 500$ (83).

From a process simulation point of view, in addition to impingement mixing, there are two main problems: (a) nonisothermal and transient flow with chemical reaction, prevalent during the filling stage of the process, and (b) conductive heat transfer with heat generation due to the polymerization reaction. We discuss these two problems next, using the case of

linear polyurethane being molded in a long, rectangular, thin mold that is fed by a ''gate'' occupying the entire feed surface.

Mold Filling by a Reactive Liquid

Domine and Gogos (88–90) considered a very long, very wide, and thin mold being fed by a constant temperature mixture of AA, BB molecules. Both types are bifunctional and the feed has a molecular weight M_0. The polymerization, assumed to be reversible, proceeds by the reaction of A-ends with B-ends, and follows idealized step polymerization (condensation) kinetics without the generation of a small molecule (91). Specifically, we have

$$\mathrm{AA} + \mathrm{BB} \underset{k_r}{\overset{k_f}{\rightleftharpoons}} \mathrm{AA} - \mathrm{BB} \qquad [-\Delta H] \tag{13.2-5}$$

Setting $(\mathrm{AA} - \mathrm{BB})_x = M_x$, we can write the general reversible condensation reaction

$$\mathrm{M}_x + \mathrm{M}_y \underset{k_r}{\overset{k_f}{\rightleftharpoons}} \mathrm{M}_{x+y} \qquad [-\Delta H] \tag{13.2-6}$$

Equation 13.2-5 is second order in A- or B-ends and first order in A–B links. The rate of change of the concentrations c_A, c_B, and c_AB are

$$\left.\begin{aligned} \frac{dc_\mathrm{A}}{dt} &= -k_f c_\mathrm{A} c_\mathrm{B} + k_r c_\mathrm{AB} \\ \frac{dc_\mathrm{B}}{dt} &= -k_f c_\mathrm{A} c_\mathrm{B} + k_r c_\mathrm{AB} \\ \frac{dc_\mathrm{AB}}{dt} &= -k_f c_\mathrm{A} c_\mathrm{B} - k_r c_\mathrm{AB} \end{aligned}\right\} \tag{13.2-7}$$

thus, $dc_\mathrm{A}/dt = dc_\mathrm{B}/dt = -dc_\mathrm{AB}/dt$ and for $c_\mathrm{A} = c_\mathrm{B}$, $c_\mathrm{A0} = c_\mathrm{B0}$, $c_\mathrm{AB0} = 0$, and $c_\mathrm{AB} = c_\mathrm{A0} - c_\mathrm{A}$, and we can write Eq. 13.2-7 as

$$\frac{dc_\mathrm{A}}{dt} = -k_f c_\mathrm{A}^2 + k_f[c_\mathrm{A0} - c_\mathrm{A}] \tag{13.2-8}$$

Defining the reaction conversion ϕ as

$$c_\mathrm{A} = c_\mathrm{A0}(1 - \phi) \tag{13.2-9}$$

Eq. 13.2-8 becomes

$$\frac{d\phi}{dt} = k_f c_\mathrm{A0}(1 - \phi)^2 - k_r \phi \tag{13.2-10}$$

For a flowing system with a velocity $v_x = v_x(x, y, t)$ undergoing the chemical reaction just given, $d\phi/dt = D\phi/Dt$. Thus, Eq. 13.2-10 becomes

$$\frac{\partial \phi}{\partial t} + v_x \frac{\partial \phi}{\partial x} = k_f c_\mathrm{A0}(1 - \phi)^2 - k_r \phi \tag{13.2-11}$$

The boundary and initial conditions are

$$\left.\begin{aligned}\phi(0,y,t) &= 0\\ \phi(x,y,0) &= 0\end{aligned}\right\} \tag{13.2-12}$$

Both reaction-rate constants are assumed to obey the Arrhenius temperature dependence

$$\left.\begin{aligned}k_f &= k_{f0}\exp\left(\frac{-E_{fr}}{RT}\right)\\ k_r &= k_{r0}\exp\left(\frac{-E_{rr}}{RT}\right)\end{aligned}\right\} \tag{13.2-13}$$

The forward and reverse reaction activation energies are related to the heat of reaction as follows (89);

$$E_{rr} - E_{fr} = -\Delta H \tag{13.2-14}$$

The reaction also has a characteristic temperature, where $k_f = k_r$. For this reacting system the number and weight average molecular weights are (91)

$$\overline{M}_n = \frac{M_0}{1-\phi} \tag{13.2-15}$$

$$\overline{M}_w = M_0\left[\frac{1+\phi}{1-\phi}\right] \tag{13.2-16}$$

To solve the filling flow and heat-transfer problem with the reacting system just given, we need to specify the x-direction momentum and energy balances. Following Domine and Gogos (88–90), the x-momentum equation during filling is

$$\rho\frac{\partial v_x}{\partial t} = -\frac{\partial P}{\partial x} + \eta\frac{\partial^2 v_x}{\partial y^2} + \frac{\partial \eta}{\partial y}\frac{\partial v_x}{\partial y} \tag{13.2-17}$$

The boundary conditions for Eq. 13.2-17 are

$$\left.\begin{aligned}\frac{\partial v_x}{\partial y}(x,0,t) &= 0\\ v_x\left(x,\frac{H}{2},t\right) &= 0\\ \frac{\partial \eta}{\partial y}(x,0,t) &= 0\\ \frac{\partial v_x}{\partial t}(0,y,t) &= 0\\ \frac{\partial P}{\partial x}(0,y,t) &= 0\end{aligned}\right\} \tag{13.2-18}$$

The viscosity is given by the Carreau fluid equation, which for melts is

$$\eta = \frac{\eta_0}{[1 + (\lambda\dot{\gamma})^2]^{(1-n)/2}} \tag{13.2-19}$$

where

$$\lambda = \frac{\lambda_0 \eta_0 (\overline{M}_w)^{0.75}}{\rho T} \tag{13.2-20}$$

and λ_0 is a curve-fitting parameter. The zero shear viscosity is primarily a function of the weight-average molecular weight

$$\eta_0 = \alpha_i (\overline{M}_w)^{\beta_i} \exp\left(\frac{\Delta E}{RT}\right) \tag{13.2-21}$$

where α_i are material parameters, and

$$\Delta E = \delta_i \exp\left(\frac{-\varepsilon_i}{\overline{M}_n}\right) \tag{13.2-22}$$

and $i = 1,2$, and denote the two regions of no entanglement and entanglement, respectively. Specifically, for $i = 1$, $\overline{M}_w < M_e$ (91)

$$\begin{aligned} \beta_1 &= 1 \\ \delta_1 &= \Delta E_0 \exp\left(\frac{\varepsilon_1}{M_0}\right) \\ \varepsilon_1 &= M_0 \left(\frac{M_e + M_0}{M_e - M_0}\right) \ln\left(\frac{\Delta E}{\Delta E_0}\right) \end{aligned} \tag{13.2-23}$$

For $i = 2$, $\overline{M}_w > M_e$

$$\begin{aligned} \beta_2 &= 3.4 \\ \delta_2 &= \Delta E \\ \varepsilon_2 &= 0 \end{aligned} \tag{13.2-24}$$

The energy equation for the filling stage is for constant density and thermal conductivity:

$$\rho C_p \left(\frac{\partial T}{\partial t} + v_x \frac{\partial T}{\partial x}\right) = k \frac{\partial^2 T}{\partial y^2} + \eta \left(\frac{\partial v_x}{\partial y}\right)^2 + \frac{\partial \phi}{\partial t}(-\Delta H) \tag{13.2-25}$$

The boundary conditions for Eq. 13.2-25 are

$$\begin{aligned} \frac{\partial T}{\partial y}(x, 0, t) &= 0 \\ \frac{\partial T}{\partial y}\left(x, \frac{H}{2}, t\right) &= -\frac{h}{k}\left[T\left(x, \frac{H}{2}, t\right) - T_w\right] \\ T(0, y, t) &= T_0 \\ \frac{\partial T}{\partial t}(0, y, t) &= 0 \end{aligned} \tag{13.2-26}$$

where T_w is the mold temperature and T_0 is the temperature of the feed, both time independent.

Section 13.1 indicated that the fountain flow in the front region could be neglected in the simulation of the mold filling process and calculations of the time-dependent front position and filling pressure. In RIM, unfortunately, this is no longer true, because the fluid viscosity depends on the molecular weight, and to know the molecular weight of any fluid element at any time, we must know where the fluid has been since entering the mold. Domine (88) tracked fluid particles as they move from the central region of the front toward the front mold wall in a manner similar to that of the fountain flow.

The species balance relation Eq. 13.2-8 is transformed to a difference equation using the forward difference on the time derivative and the backward difference on the space derivative. The finite difference form of the x-momentum equation (Eq. 13.2-25) is obtained by using the forward difference on all derivatives, and is solved by the Crank–Nicolson method. The same is true for the energy equation (Eq. 13.2-26).

The results of the simulation show that for reaction rates that are common in the conventional RIM process, the chemical reaction cannot be ignored during the filling step. In other words, RIM *is not casting*. Appreciable conversion and nonisothermicity can be obtained during filling. Figure 13.42 gives the conversion and temperature fields at the moment of fill. Both temperature and conversion increase with increasing flow direction distance; this is simply the result of larger residence times. It is worth noting that the fountain flow taking the reactive fluid from the center and depositing it on the wall makes both profiles flatter. As the feed reaction constant and the fill time increase, there is more chance for chemical reaction during filling.

Figure 13.43 presents the results of such increases, for the case where the product of $(k_f \times t_{\text{fill}})$ is four times that of the preceding case. Conversion levels exceeding 90% are obtained, giving rise to a rather thick ''reacted skin,'' as Fig.13.43(b) indicates by the line for velocity of 10 cm/s. Furthermore, there is a pinching effect on the flow midway in the flow direction, which results in a nipple-like velocity profile with very high velocity gradients and viscous energy dissipation (VED) levels. As a matter of fact, for the system studied, there appears to be an upper limit in the feed-condition reaction-rate constant because of local thermal problems that arise by way of high chemical and viscous heat generation terms. This problem can be reduced by increasing the thermal conductivity of the reacting system (by incorporating conductive additives) and by making the system more shear thinning (perhaps by the addition of dissolved elastomer). At any rate, the effects of both the material and process variables must be studied in order to understand the filling step of the RIM process. A study of this kind was carried out by Domine (88).

Peters et al. (46) utilized their fourth-order approximation of the fountain flow velocity field, Eqs. 13.1-9 and 13.1-10, and the particle tracking numerical technique they incorporated, to calculate the temperature and conversion fields in that region. They assumed that the very flow front material particles experience an adiabatic thermal history, which is reasonable.

At the end of the filling stage, only heat transfer with chemical reaction occurs, which can be described by the following species and energy balance equations:

$$\frac{d\phi}{dt} = k_f c_{\text{A0}}(1-\phi)^2 - k_r\phi \tag{13.2-27}$$

$$\rho C_p \frac{\partial T}{\partial t} = k\frac{\partial^2 T}{\partial y^2} + k\frac{\partial^2 T}{\partial x^2} + \frac{\partial \phi}{\partial t}(-\Delta H) \tag{13.2-28}$$

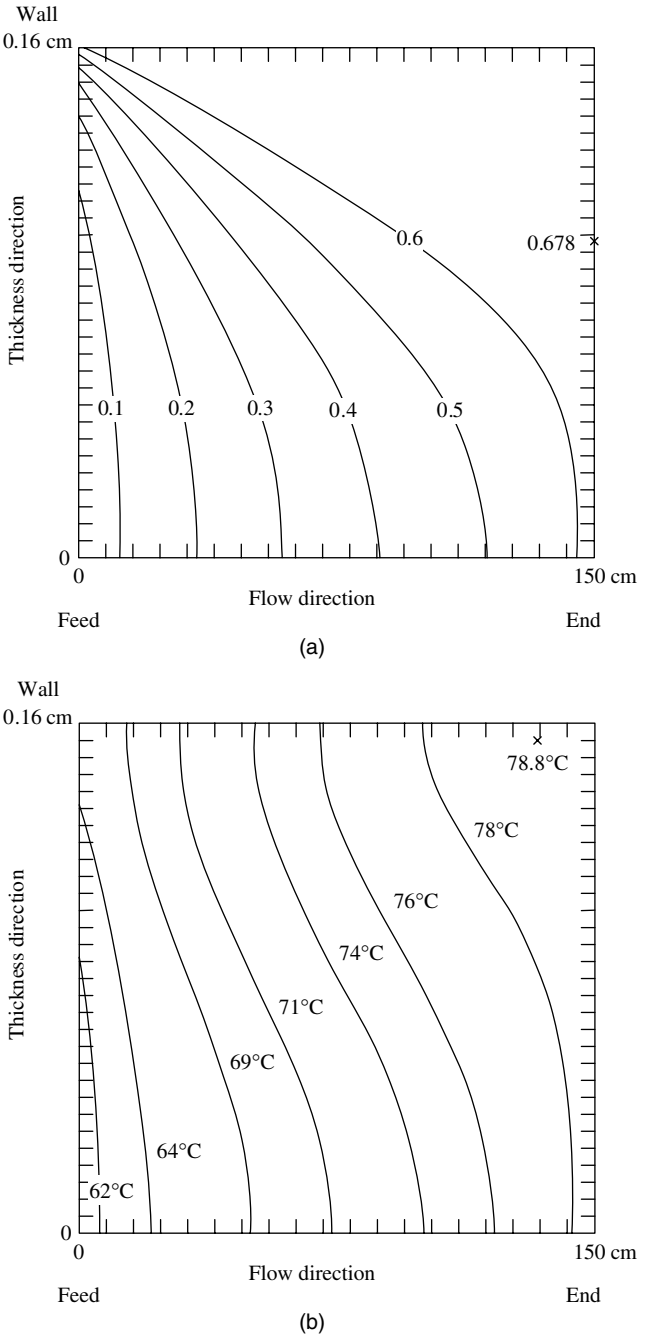

Fig. 13.42 Simulation results of the RIM process involving a linear step polymerization: $T_0 = T_w = 60°C$, $k_f = 0.5\,\text{L/mole} \cdot \text{s}$, $t_{\text{fill}} = 2.4\,\text{s}$. (a) Conversion contours at the time of fill. (b) Temperature contours at the time of fill. [Reprinted by permission from J. D. Domine and C. G. Gogos, ''Computer Simulations of Injection Molding of a Reactive Linear Condensation Polymer,'' paper presented at the *Society of Plastics Engineers, 34th Annu. Tech. Conf.*, Atlantic City, NJ, 1976. (Also published in the *Polym. Eng. Sci.*, **20**, 847–858 (1980); volume honoring Prof. B. Maxwell).]

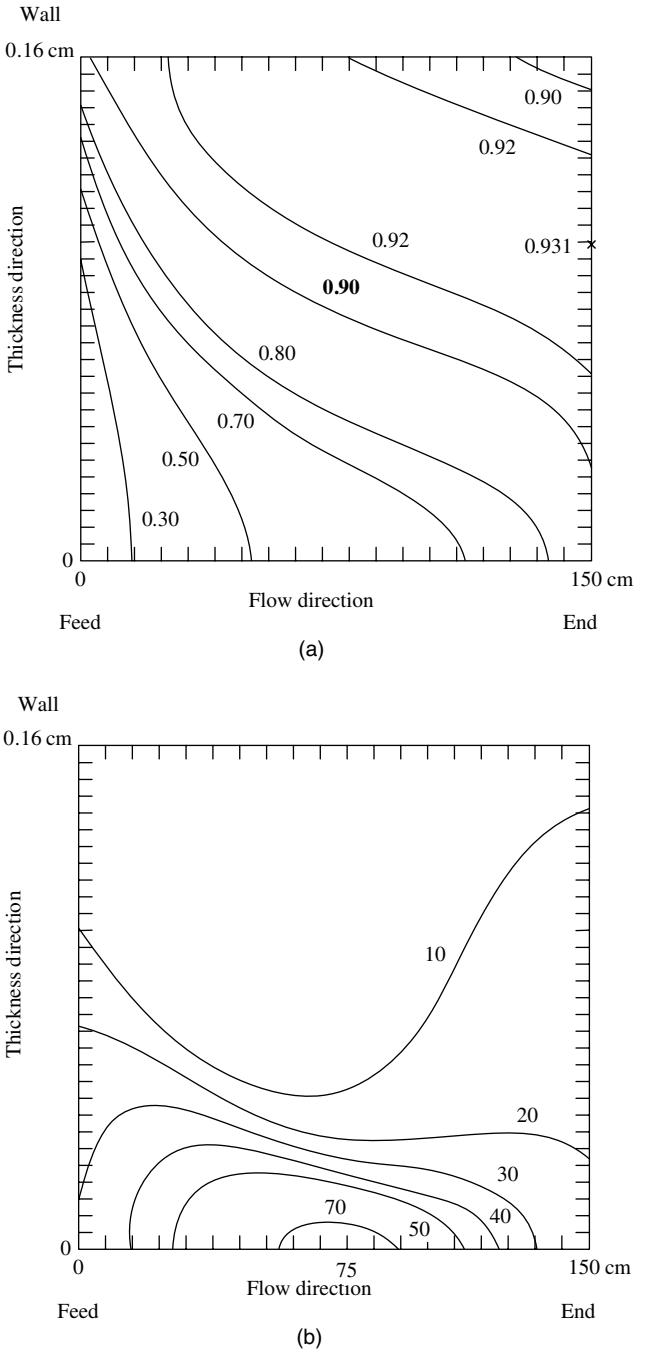

Fig. 13.43 Simulation results of the RIM process involving a linear step polymerization: $T_0 = T_w = 60°C$, $k_f = 1.0\,\text{L/mole} \cdot \text{s}$, $t_{\text{fill}} = 4.8\,\text{s}$. (a) Conversion contours at the time of fill. (b) Temperature contours at the time of fill. [Reprinted by permission from J. D. Domine and C. G. Gogos, "Computer Simulations of Injection Molding of a Reactive Linear Condensation Polymer," paper presented at the *Society of Plastics Engineers, 34th Annu. Tech. Conf.*, Atlantic City, NJ, 1976. (Also published in the *Polym. Eng. Sci.*, **20**, 847–858 (1980); volume honoring Prof. B. Maxwell.)]

The axial conduction, which was neglected in Eq. 13.2-28 as being smaller than axial convection, is now included. The two preceding equations hold for $t \geq t_{\text{fill}}$. The temperature boundary conditions for an adiabatic feed surface are

$$\begin{aligned} \frac{\partial T}{\partial x}(0,y,t) &= 0 \\ \frac{\partial T}{\partial x}(l,y,t) &= -\frac{h}{k}[T(l,y,t) - T_w] \\ \frac{\partial T}{\partial y}\left(x,\frac{H}{2},t\right) &= -\frac{h}{k}\left[T\left(x,\frac{H}{2},t\right) - T_w\right] \\ \frac{\partial T}{\partial y}(x,0,t) &= 0 \end{aligned} \tag{13.2-29}$$

Since the energy balance involves second-order derivatives in both the x and y directions, the alternating direction implicit (ADI) method is used (92). This method requires three time levels of temperature and involves the solution of the equation twice, once in each direction.

The ''postfill cure'' and heat transfer continues until the thickness–average tensile modulus is high enough at every x position for the part to be removed. The tensile modulus is dependent on the number average molecular weight (89). Through this procedure the *de-mold time* is obtained. The de-mold time for the case corresponding to Fig. 13.42 is 62.4 s, compared to 12 s for the case corresponding to Fig. 13.43. The low de-mold time in the latter case is the result of the thick reacted skin formed during the filling process, as mentioned previously.

Analyses such as the foregoing are necessary to understand the interrelations among the chemical, process, and rheological variables in RIM.

Thermoplastic Foam Injection Molding

In thermoplastic foam injection molding, which is, in principle, a RIM-like process, a gas is introduced into the molten polymer in the injection molding machine (93), or a gas-producing compound (usually in fine powder form) is mixed with the polymer pellets or powder prior to processing. In either case, upon injection into the mold, the gas can be released from the solution because of the prevailing low pressures, especially as the advancing front is approached. The product formed can have a very dense ''skin'' and a foamed ''core'' that has a 20–50% density of the unfoamed polymer. The surface contains only a few voids because of the phenomenon of skin formation. Nevertheless the surface is not void-free because of the low pressures during the fountain-flow phenomenon. Typical density profiles of thermoplastic structural foam articles indicate that the solid surface skin is usually about one-quarter of the half-thickness. The density decreases *rapidly* to a constant low value in the core region.

These facts justify the statement made previously that this process is similar to RIM, since physicochemical reactions occur concurrently with mold filling. On the other hand, in contrast to RIM, gas generation can occur *well before* the melt reaches the mold, necessitating the consideration of the chemical reaction during the melting, melt storage, and pumping steps of the process [i.e., inside the injection molding machine (94–96)]. The principles of bubble nucleation and growth in a polymer melt, which are relevant to this process as well, were discussed in Chapter 8.

13.3 COMPRESSION MOLDING

In the compression molding process, a thermoplastic or partially polymerized thermosetting polymer is placed in a heated cavity, usually in a preheated and preformed shape vaguely corresponding to that of the cavity; the mold begins to close and pressure is applied to the preform, forcing it to further heat up close to the mold temperature, and flow to fill the mold cavity. In the process, the polymer undergoes complete polymerization (cross linking). Then the mold is opened, the part is ejected, and the cycle starts again. This process wastes very little material (no runners and sprue) and can produce large parts. However, it is difficult to produce parts with very close tolerances because the final size of the compression molded article depends on the *exact* amount of the preform. Furthermore, the process does not easily lend itself to molding of intricate parts with deep undercuts.

Figure 13.44 represents the various stages of the compression molding cycle from the point of view of the plunger force needed to close the mold at a constant rate. In the first region, $t \leq t_f$, the force increases rapidly as the preform is squeezed and heated. At t_f, the polymer is presumably in the molten state and, as such, is forced to flow into the cavity and fill it. Filling terminates at t_c, when compression of the polymer melt takes place, to compensate for the volume contraction that results from the polymerization reaction. The bulk of the chemical reaction occurs after t_c. We now comment on each of the steps of the compression molding process.

During the preform-heating part of the cycle, the main problems to be considered are heat transfer and flow (or elastic deformation) of the compressed particulate matter. Referring to Fig. 13.45, the heat transfer problem can be described with the following form of the energy equation:

$$\rho C_p \frac{\partial T}{\partial t} = k \frac{\partial^2 T}{\partial z^2} \tag{13.3-1}$$

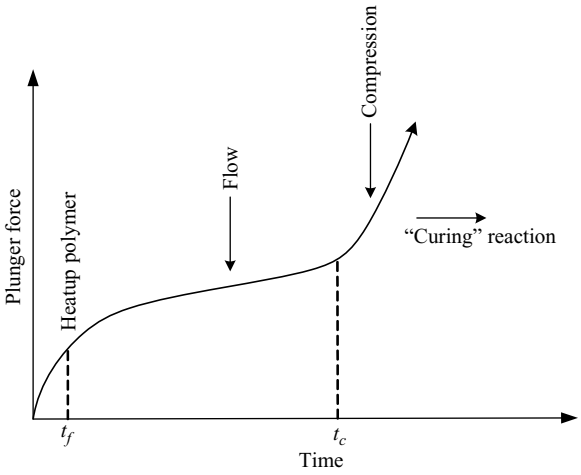

Fig. 13.44 Schematic representation of the plunger force applied during compression molding to move the plunger at a constant speed. The various stages of the process are depicted.

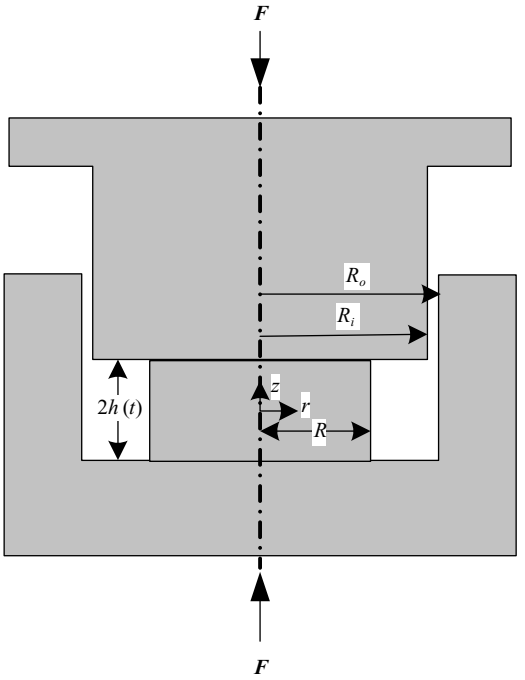

Fig. 13.45 The geometry and coordinate frame used for the simulation of the compression-molding process of a cup-shaped cavity.

where the following assumptions have been made: the convective and dissipative effects associated with v_r are negligible, as is the radial conductive heat transfer, and the thermophysical properties are taken to be constant. The temperature of the preform is constant at the start of the process, and the boundary conditions are

$$\begin{aligned} \frac{\partial T}{\partial z}(0,t) &= 0 \\ \frac{\partial T}{\partial z}[h(t),t] &= -U[T(h(t),t) - T_w] \end{aligned} \tag{13.3-2}$$

where U is the ratio of the heat transfer coefficient to the thermal conductivity. Furthermore, because of the plunger motion,

$$h(t) = h_0 - \dot{h}t \tag{13.3-3}$$

The heat transfer problem just discussed can be solved in a fashion similar to the one used in Section 5.3, to yield $T(z,t)$. In principle, once the temperature field is known in the preform at any time before t_f, the plunger force can be calculated. The preform can be taken as a solid that slips at the mold surface and has a temperature-dependent compressive modulus. At any time $t < t_f$, each layer of the preform will deform by an amount such that (a) the force on *every* layer of thickness Δz is the same (and equal to the unknown quantity), and (b) the sum of the compressive deformations of all the layers equals the deformation imposed on the preform by the plunger at the given time. The force

can also be estimated by assuming that the preform is a viscous liquid with a temperature-dependent viscosity undergoing an overall constant rate squeezing flow. The problem can then be solved in a manner similar to that in Example 6.14. An average temperature value can be used, or each layer can be considered to flow at a rate such that (a) the force on every layer is independent of z, and (b) the sum of all the squeezing rates is equal to the one applied by the plunger $\dot{h}$.

Assuming that $T(z, t_f) = T_w$, we can deal with the flow problem alone for $t_f < t < t_c$. Referring to Fig. 13.45, as long as the preform radius is less than R_0, we can treat the problem as an isothermal radial flow of an incompressible fluid flowing between two disks that approach each other at a constant rate $\dot{h}$. Recapturing the results for the velocity field, pressure distribution, and plunger force needed to squeeze an isothermal Power Law fluid at a constant slow or moderate squeeze rate, we have

$$v_r(z, r, t) = \frac{h^{1+s}}{1+s}\left(-\frac{1}{m}\frac{\partial P}{\partial r}\right)^s \left[1 - \left(\frac{z}{h}\right)^{1+s}\right] \tag{13.3-4}$$

where the pressure gradient can be obtained from

$$P = P_a + \frac{m(2+s)^n}{2^n(n+1)}\frac{(-\dot{h})R^{n+1}}{h^{2n+1}}\left[1 - \left(\frac{r}{R}\right)^{n+1}\right] \tag{13.3-5}$$

The plunger force F_N can be calculated from the preceding equation to give

$$F_N = \frac{\pi m(2+s)^n}{2^n(n+3)}\frac{(-\dot{h})^n R^{3+n}}{h^{2n+1}} \tag{13.3-6}$$

Since the fluid is incompressible and nonreactive at this stage, its volume is constant, implying that

$$h(t)R^2(t) = C_1 \tag{13.3-7}$$

Thus, the Scott Equation 13.3-6 becomes

$$F_N = \frac{\pi m(2+s)^n}{2^n(n+3)}\frac{(-\dot{h})^n R^{5(n+1)}}{C_1^{2n+1}} \tag{13.3-8}$$

When the radius of the flowing preform reaches the value of R_o, the fluid is forced to flow in the annular space $R_o - R_i$. For a constant squeeze rate, the rate of increase of the axial annular distance $\dot{l}$ occupied by the melt is

$$-\pi R_i^2 \dot{h}(t) = \pi(R_o^2 - R_i^2)\dot{l} \tag{13.3-9}$$

For small annular spacing $\Delta R \ll 1$, and Eq. 13.3-9 can be written as

$$\dot{l} = \dot{h}\left(\frac{\overline{R}}{2\Delta R}\right) \tag{13.3-10}$$

Once annular flow occurs, there is an additional force term acting on the plunger. The pressure at $r = R_i$ is not atmospheric but that which is needed to support the flow in the annulus. To calculate this pressure, we first turn to the volumetric flow rate in the annular region, which is

$$Q = \pi(R_o^2 - R_i^2)\dot{l} \tag{13.3-11}$$

For a thin annulus, $\Delta R \ll \overline{R}$, the plunger travel rate $\dot{h}$ is very small compared to $\dot{l}$, and the annular flow can be considered to be a pressure, not a combined pressure and drag flow. For a thin annulus, Eq. 13.3-11 reduces to

$$Q = 2\pi\overline{R}\Delta R\dot{l} \tag{13.3-12}$$

For isothermal annular pressure flow of an incompressible Power Law fluid, Fredrickson and Bird (97) have calculated the following relationship between Q and ΔP

$$Q = \frac{\pi R_o^3}{s+2}\left(\frac{R_o\Delta P}{2ml}\right)^s (1-\kappa)^{s+2}F(n,\kappa) \tag{13.3-13}$$

where $1/\beta = \kappa = R_i/R_o$. Figure 12.45 plots $F(n,\kappa)$. For a thin annulus, $F(n,\kappa) \to 1$ and Eq. 13.3-13 reduces to

$$Q = \frac{\pi R_o^3}{s+2}\left(\frac{R_o\Delta P}{2ml}\right)^s (1-\kappa)^{s+2} \tag{13.3-14}$$

Therefore, to calculate the added pressure at $r = R_i$, we use Eqs. 13.3-11 and 13.3-13 for a wide annulus, or Eqs. 13.3-12 and 13.3-14 for a thin annulus. For the latter case, we write

$$P(R) - P_{\text{atm}} = \frac{2ml}{R_o^{3n+1}}\frac{\left[2(s+2)\overline{R}\Delta R\dot{l}\right]^n}{(1-\kappa)^{+2n}} \tag{13.3-15}$$

When this is multiplied by the plunger area and added to the right-hand side of Eq. 13.3-6, the plunger force is obtained for the case where annular flow takes place in a cup-shaped cavity in compression molding. Similar expressions can be obtained for the entire flow stage $t_f < t < t_c$, during the compression molding of other shapes, by making use of the quasi–steady state and, when needed, the lubrication approximation.

The reaction stage of the compression molding process can be described by Eqs. 13.2-27 and 13.2-28, employed in the simulation of the postfilling reaction stage in the RIM process. Of course, Eq. 13.2-27 is applicable only to a linear and reversible step polymerization. Furthermore, we have assumed that the melt is at a uniform temperature at the beginning of the reaction. Therefore, in Eq. 13.2-28 conduction should occur only in the thickness direction. Broyer and Macosko (98) have solved the problem of heat transfer numerically with a cross-linking polymerization reaction that is more representative of the compression molding process. For a thin rectangular mold of half-thickness h and temperature T_w, as well

as *n*th-order kinetics and constant thermophysical properties, the governing equations in dimensionless form are

$$-\frac{dc_A^*}{dx} = k^* c_A^{*n} \exp B\left[\frac{\Delta T'_{ad} T^*}{\Delta T'_{ad} T^* + 1}\right] \tag{13.3-16}$$

and

$$-\frac{dT^*}{dt^*} = \frac{\partial^2 T^*}{\partial y^*} + k^* c_A^{*n} \exp B\left[\frac{\Delta T'_{ad} T^*}{\Delta T'_{ad} T^* + 1}\right] \tag{13.3-17}$$

where $c_A^* = c_A/c_{A0}$, $t^* = \alpha t/h^2$, $y^* = y/h$, h is the half-thickness of the polymerizing slab, $k^* = c_{A0}^{n-1} h^2 A e^{-B}/\alpha$, $B = E/RT_0$, E is the reaction activation energy, and A is the frequency factor, $T^* = (T - T_0)/(T_{ad} - T_0)$, and the adiabatic temperature rise is

$$\Delta T'_{ad} = \frac{T_{ad} - T_0}{T_0} = \frac{\Delta H c_{A0}}{\rho C_p T_0} \tag{13.3-18}$$

where ΔH is the heat of reaction, c_A is the concentration of the A functional group in the trifunctional group-bifunctional group step reaction

$$A_3 + B_2 \rightarrow \text{cross-linked polymer}$$

The system of Eqs. 13.3-17 and 13.3-18 can be solved for the adiabatic, isothermal, or constant wall flux cases using the Crank–Nicolson method. The thermomechanical and reaction data for such systems were evaluated by Lifsitz, Macosko, and Mussatti (99) at 45°C for a polyester triol and a chain extended 1,6-hexamethylene diisocyanate (HDI) with dibutyltin as a catalyst. Figure 13.46 gives the temperature profiles for the isothermal-wall case. Because of the high heat of polyurethane formation and the low conductivity of

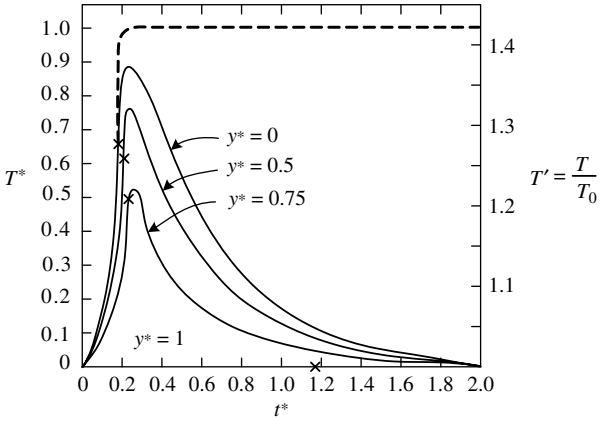

Fig. 13.46 Temperature distribution in a reacting polyurethane slab; isothermal-wall simulations. Dotted line denotes the adiabatic temperature rise and ×'s indicate gel points. $k^* = 1$, $n = 1$, $\Delta T'_{ad} = 0.423$, and $B = 18.7$, $\phi_{\text{gel}} = 0.707$. [Reprinted by permission from E. Broyer and C. W. Macosko, "Heat Transfer and Curing in Polymer Reaction Molding," *AICHE J.* **22**, 268 (1976).]

the system, the center of the slab shows nearly an adiabatic temperature rise. The peaks come also closer to the adiabatic temperature when k^* is increased.

The extent of the reaction ϕ can be related to the $\bar{M}_w$ for the triol-HDI-polyurethane system under equal stoichiometry (100) as follows:

$$\bar{M}_w = \frac{\frac{2}{3}(1+\phi^2)M_{A_3}^2 + (1+2\phi^2)M_{B_2}^2 + 4\phi M_{A_3}M_{B_2}}{\left(\frac{2}{3}M_{A_3} + M_{B_2}\right)(1-2\phi^2)} \tag{13.3-19}$$

The ''gel point'' is defined as the condition when $\bar{M}_w$ goes to infinity, which occurs at $\phi \equiv \phi_{gel} = (½)^{½} = 0.707$. It follows from Fig. 13.46 that the center of the slab will gel faster than the skin. A more uniform extent of reaction can be achieved by maintaining the mold walls at a higher temperature, assuming that this does not result in excessive surface reaction and interference with the filling and the compression processes. Knowing the temperature, the conversion, and the MWD as a function of thickness and reaction time is essential in determining the required compression-mold cycle or the time and temperature in the postcuring step, if it is necessary.

REFERENCES

1. R. C. Donovan, D. E. Thomas, and L. D. Leversen, ''An Experimental Study of Plasticating in a Reciprocating-Screw Injection Molding Machine,'' *Polym. Eng. Sci.*, **11**, 353 (1971).
2. S. D. Lipshitz, R. Lavie, and Z. Tadmor, ''A Melting Model for Reciprocating Screw Injection Molding Machines,'' *Polym. Eng. Sci.*, **14**, 553 (1974).
3. G. B. Thayer, J. W. Mighton, R. B. Dahl, and C. E. Beyer, ''Injection Molding,'' in *Processing of Thermoplastic Materials,* E. C. Bernhardt, Ed., Reinhold, New York, 1959, Chapter 5.
4. I. I. Rubin, *Injection Molding-Theory and Practice,* Wiley-Interscience, New York, 1972.
5. C. F. Huang, ''Numerical Simulations of the Filling Process with a Cup-shaped Mold,'' M.S. Thesis, Department of Chemical Engineering, Stevens Institute of Technology, Hoboken, NJ, 1974.
6. W. L. Krueger and Z. Tadmor, ''Injection Molding into a Rectangular Cavity,'' *Polym. Eng. Sci.*, **20**, 426–431 (1980).
7. F. C. Caras, ''Spiral Mold for Thermosets,'' *Mod. Plast.*, **41**, 140 (1963).
8. G. D. Gilmore and R. S. Spencer, ''Role of Pressure, Temperature and Time in the Injection Molding Process,'' *Mod. Plast.*, **27**, 143 (April 1950); also, R. S. Spencer and G. D. Gilmore, ''Residual Strains in Injection Molded Polystyrene,'' *Mod. Plast.*, **28**, 97 (December 1950).
9. R. S. Spencer and G. D. Gilmore, ''Some Flow Phenomena in the Injection Molding of PS,'' *J. Colloid Sci.*, **6**, 118 (1951).
10. C. E. Beyer and R. S. Spencer, ''Rheology in Molding,'' in *Rheology,* Vol. 3, F. R. Eirich, Ed., Academic Press, New York, 1960.
11. R. L. Ballman, T. Shusman, and H. L. Toor, ''Injection Molding-Flow into a Cold Cavity,'' *Ind. Eng. Chem.*, **51**, 847 (1959).
12. R. L. Ballman and H. L. Toor, ''Injection Molding: A Rheological Interpretation - Part 1,'' *Mod. Plast.*, **37**,105 (September 1959); also R. L. Ballman, T. Shusman, and H. L. Toor, ''Injection Molding: A Rheological Interpretation – Part 2,'' *ibid.,* 37, 115 (October 1959).

13. G. B. Jackson and R. L. Ballman, ''The Effect of Orientation on the Physical Properties of Injection Moldings,'' *Soc. Plast. Eng. J.*, **16**, 1147–1152 (1960).
14. T. Aoba and H. Odaira, Flow of Polymer Melt in Injection Mold, *Proc. of the 14th Japanese Congr. on Materials Research,* Kyoto, Japan, 1970, p. 124.
15. M. R. Kamal and S. Kenig, ''The Injection Molding of Thermoplastics. Part I. Theoretical Model,'' *Polym. Eng. Sci.*, **12**, 294 (1972).
16. J. L. White and H. B. Dee, ''Flow Visualization of Injection Molding Polyethylene and Polystyrene Melts in Sandwich Molding,'' *Polym. Eng. Sci.*, **14**, 212 (1974).
17. L. R. Schmidt, ''A Special Mold and Tracer Technique for Studying Shear and Extensional Flows in a Mold Cavity during Injection Molding,'' *Polym. Eng. Sci*., **14**, 797 (1974).
18. W. Rose, ''Fluid-Fluid Interfaces in Steady Motion", *Nature*, **191**, 242–243 (1961).
19. K. Oda, J. L. White, and E. S. Clark, ''Jetting Phenomena in Injection Mold Filling,'' *Polym. Eng. Sci.*, **16**, 585 (1976).
20. J. R. A. Pearson, *Mechanical Principles of Polymer Melt Processing*, Pergamon Press, Oxford, 1966, p. 128.
21. D. H. Harry and R. G. Parrott, ''Numerical Simulation of Injection Mold Filling,'' *Polym. Eng. Sci.*, **10**, 209 (1970).
22. J. L. Berger and C. G. Gogos, ''A Numerical Simulation of the Cavity Filling Process with PVC,'' *SPE ANTEC Tech. Papers, 17* (1971); also, J. L. Berger and C. G. Gogos, ''A Numerical Simulation of the Cavity Filling Process with PVC in Injection Molding,'' *Polym. Eng. Sci*., **13**, 102–112 (1973).
23. P. C. Wu, C. F. Huang, and C. G. Gogos, ''Simulation of the Mold Filling Process,'' *Polym. Eng. Sci.*, **14**, 223 (1974).
24. B. R. Laurencena and M. C. Williams, ''Radial Flow of Non-Newtonian Fluids between Parallel Plates,'' *Trans. Soc. Rheol.*, **18**, 331 (1974).
25. G. Williams and H. A. Lord, ''Mold Filling Studies for the Injection Molding of Thermoplastics,'' *Polym. Eng. Sci.*, **15**, 553 (1975).
26. J. Crank and P. Nicolson, ''A Practical Method for Numerical Evaluation of Solutions of Partial Differential Equations of the Heat-conducting Type," *Proc. Cambridge Philos. Soc.,* **43**, 50 (1947).
27. G. G. O'Brien, M. A. Hyman, and S. Kaplan, ''A Study of the Numerical Solution of Partial Differential Equations," *J. Math. Phys.*, **29**, 223–251 (1951).
28. I. T. Barrie, ''Understanding How an Injection Mold Fills,'' *Soc. Plast. Eng. J.*, **27** (8), 64–69 (1971).
29. Z. Tadmor, ''Molecular Orientation in Injection Molding,'' *J. Appl. Polym. Sci.,* **18**, 1753–1772 (1974).
30. G. Menges and G. Wübken, ''Influence of Processing Conditions on Molecular Orientation in Injection Molds,'' *SPE ANTEC Tech. Papers*, **19**, 519 (1973).
31. H. Mavridis, A. N. Hrymak, and J. Vlachopoulos, ''A Finite Element Simuation of Fountain Flow," *Polym. Eng. Sci.*, **26**, 449–454 (1986).
32. H. R. Warner, Jr., ''Kinetic Theory and Rheology of Dilute Suspensions of Finitely Extendible Dumbbells,'' *Ind. Eng. Chem. Fundam.*, **11**, 379–387 (1972); also, R. L. Christiansen and R. B. Bird, ''Dilute Solution Rheology: Experimental Results and Finitely Extensible Nonlinear Elastic Dumbbell Theory,'' *J. Non-Newt. Fluid Mech.*, **3**, 161–177 (1977/1978).
33. W. Dietz, J. L. White, and E. S. Clark, ''Orientation Development and Relaxation in Molding of Amorphous Polymers,'' *Polym. Eng. Sci.*, **18**, 273–281 (1978).
34. C. G. Gogos and C. F. Huang, ''The Process of Cavity Filling Including the Fountain Flow in Injection Molding,'' *Polym. Eng. Sci.*, **26**, 1457–1466 (1986).

35. C. F. Huang, Ph.D. Dissertation, Department of Chemical Engineering, Stevens Institute of Technology, Hoboken, NJ, 1978.
36. B. Friedrichs and S. I. Güçeri, ''A Novel Hybrid Numerical Technique to Model 3-D Fountain Flow in Injection Molding Processes,'' *J. Non-Newt. Fluid Mech.*, **49**, 141–173 (1993).
37. E. Mitsoulis and J. Vlachopoulos, ''The Finite Element Method for Flow and Heat Transfer Analysis,'' *Adv. Polym. Technol.*, **4**, 107–121 (1984).
38. F. M. Orr and L. E. Scriven, ''Rimming Flow: Numerical Simulation of Steady, Viscous, Free-surface Flow with Surface Tension,'' *J. Fluid Mech., 84*, 145–165 (1978).
39. D. H. Chung and T. H. Kwon, ''Numerical Studies of Fiber Suspensions in an Axisymmetric Radial Diverging Flow: the Effects of Modeling and Numerical Assumptions,'' *J. Non-Newt. Fluid Mech.*, **107**, 67–96 (2002).
40. E. Thompson, ''Use of Pseudo-concentrations to Follow Creeping Viscous Flows during Transient Analysis,'' *Int. J. Numer. Meth. Fluids,* **6**, 749–761 (1986).
41. G. A. A. V. Haagh and F. N. V. D. Vosse, ''Simulation of Three-dimensional Polymer Mould Filling Processes Using a Pseudo-concentration Method,'' *Int. J. Numer. Meth. Fluids*, **28,** 1355–1369 (1998).
42. S. M. Dinh and R. C. Armstrong, ''A Rheological Equation of State for Semi-concentrated Fiber Suspensions,'' *J. Rheol.,* **28** (3), 207–227 (1984).
43. A. C. Garcia, ''Reactive Mold Filling Modeling,'' Ph.D. Thesis, Chemical Engineering Department, University of Minnesota, Minneapolis, 1991.
44. S. K. Goyal, E. Chu, and M. R. Kamal, ''Non-isothermal Radial Filling of Center-gated Disc Cavities with Viscoelastic Polymer Melts,'' *J. Non-Newt. Fluid Mech.*, **28**, 373–406 (1988).
45. D. J. Coyle, J. W. Blake, and C. W. Macosko, ''Kinematics of Fountain Flow in Mold Filling,'' *AIChE J.*, **33**, 1168–1172 (1987).
46. G. W. M. Peters, P. J. L. van der Velden, H. E. H. Meijer, and P. Schoone, ''Multilayer Injection Moulding,'' *Int. Polym. Process.*, **9**, 258 (1994).
47. A. C. B. Bogaerds, G. W. M. Peters, and F. P. T. Baaijens, ''Tiger Stripes: Instabilities in Injection Molding'' in *Polymer Processing Instabilities*, S. G. Hatzikiriakos and K. B. Migler, Eds., Marcel Dekker, New York, 2005.
48. M. Bulters and A. Schepens, ''The Origin of the Surface Defect 'Slip-stick' on Injection Moulded Products,'' *Proc. Annu. Meet.*, American Institute of Chemical Engineering, Los Angeles, CA, 2000.
49. M. Bulters and A. Schepens, ''The Origin of the Surface Defect 'Slip-stick' on Injection Moulded Products,'' *Proc. 16th Annu. Meet.*, *Polymer Processing Society*, Shanghai, 2000, pp. 144–145.
50. M. C. O. Chang, ''On the Study of Surface Defects in the Injection Molding of Rubber-modified Thermoplastics,'' *SPE ANTEC Tech. Papers*, **40**, 360–367 (1994).
51. H. Hamada and H. Tsunasawa, ''Correlation between Flow Mark and Internal Structure of Thin PC/ABS Blend Injection Moldings,'' *J. Appl. Polym. Sci.*, **60**, 353–362 (1996).
52. S. Y. Hobbs, ''The Development of Flow Instabilities during the Injection Molding of Multicomponent Resins,'' *Polym. Eng. Sci.*, **36**, 1489–1494 (1996).
53. B. Monasse, L. Mathieu, M. Vincent, J. M. Haudin, J. P. Gazonnet, V. Durand, J. M. Barthez, D. Roux, and J. Y. Charmeau, ''Flow Marks in Injection Molding of Polypropylene: Influence of Processing Conditions and Formation in Fountain Flow,'' *Proc. 15th Annual Meeting*, *Polymer. Processing Society,* Hertogenbosch, 1999.
54. F. J. Rielly and W. L. Price, ''Plastic Flow in Injection Molds,'' *SPE J.*, **17**, 1097–1101 (1961).
55. M. M. Denn, ''Extrusion Instabilities and Wall Slip,'' *Ann. Rev. Fluid Mech.*, **33**, 265 (2001).
56. R. S. Graham, T. C. B. McLeish, and O. G. Harlen, ''Using the Pom-pom Equations to Analyze Polymer Melts in Exponential Shear,'' *J. Rheol.*, **45**, 275–290 (2001).

57. N. J. Inkson, T. C. B. McLeish, O. G. Harlen, and D. J. Groves, ''Predicting Low Density Polyethylene Melt Rheology in Elongational and Shear Flows with 'Pom-pom' Constitutive Equations,'' *J. Rheol.*, **43**, 873–896 (1999).
58. W. M. H. Verbeeten, G. W. M. Peters, and F. P. T. Baaijens, ''Differential Constitutive Equations for Polymer Melts: The Extended Pom–pom Model,'' *J. Rheol.*, **45**, 823–843 (2001).
59. E. Vos, H. E. H. Meijer, and G. W. M. Peters, ''Multilayer Injection Molding,'' *Int. Polym. Process.*, **6,** 42–50 (1991).
60. F. Fairbrother and A. E. Stubbs, *J. Chem. Soc.*, **1,** 527 (1935).
61. R. N. Marchessault and S. G. Mason, ''Flow of Entrapped Bubbles through a Capillary,'' *Ind. Eng. Chem.*, **52**, 79–84 (1960).
62. G. I. Taylor, ''Deposition of a Viscous Fluid on the Wall of a Tube,'' *J. Fluid Mech.*, **10,** 161–165 (1961).
63. B. G. Cox, ''On Driving a Viscous Fluid Out of a Tube,'' *J. Fluid Mech.*, **14,** 81–96 (1962).
64. H. Westborg and O. Hassager, ''Creeping Motion of Long Bubbles and Drops in Capillary Tubes,'' *J. Colloid Interface Sci.*, **133**, 135–147 (1989).
65. A. J. Poslinski, P. R. Oehler, and V. R. Stokes, ''Isothermal Gas-assisted Displacement of Viscoplastic Liquids in Tubes,'' *Polym. Eng. Sci.,* **35,** 877–892 (1995).
66. A. J. Poslinski and D. J. Coyle, ''Steady Gas Penetration through Non-Newtonian Liquids in Tube and Slit Geometries: Isothermal Shear-Thinning Effects,'' *Proc. Polymer Processing Society, 10th Annu. Meet.*, Akron, Ohio (1994), pp. 219–220.
67. P. C. Huzyak and K. W. Koelling, ''The Penetration of a Long Bubble through a Viscoelastic Fluid in a Tube,'' *J. Non-Newt. Fluid Mech.*, **71,** 73–88 (1997).
68. V. Gauri and K. W. Koelling, ''Gas-assisted Displacement of Viscoelastic Fluids: Flow Dynamics at the Bubble Front,'' *J. Non-Newt. Fluid Mech.*, **83,** 183–203 (1999).
69. H. Giesekus, *Rheol. Acta*, **2,** 122 (1962).
70. K. W. Koelling, V. Gauri, M. Tendulkar, R. Kaminski, and O. Becker, ''Understanding the Controlling Mechanisms of Gas-assisted Injection Molding through Visualization,'' *SPE ANTEC Tech. Papers*, **43**, 3697–3701 (1997).
71. O. C. Zienkiewicz, P. Mayer, and Y. K. Cheung, ''Solution of Anisotropic Seepage Problems by Finite Elements,'' *Proc. Am. Soc. Civ. Eng.*, **92**, EM1, 111–120 (1964).
72. E. Broyer, C. Gutfinger, and Z. Tadmor, ''A Theoretical Model for the Cavity Filling Process in Injection Molding,'' *Trans. Soc. Rheol.*, **19**, 423 (1975).
73. Y. Kuo and M. R. Kamal, ''Flows of Thermoplastics in the Filling and Packing Stages of Injection Molding,'' paper presented at the International Conference on Polymer Processing, MIT, Cambridge, MA. August 16, 1977.
74. R. C. Thamm, ''Phase Morphology of High-Impact-Strength Blends of EPDM and Polypropylene. Knit-line Behavior,'' *Rubber Chem. Technol.*, **50***,* 24–34 (1977).
75. M. R. Kantz, H. H. Newman, Jr., and F. H. Stigale, ''The Skin-Core Morphology and Structure-Properties Relationships in Injection Molded PP,'' *J. Appl. Polym. Sci.*, **16.** 1249 (1972).
76. E. S. Clark, ''Morphology and Properties of Injection Molded Crystalline Polymers,'' *Appl. Polym. Symp.*, **24**, 45–53 (1974).
77. S. Y. Hobbs, ''Some Observations in the Morphology and Fracture Characteristics of Knit-lines,'' *Polym. Eng. Sci.*, **14**, 621 (1974).
78. K. J. Cleereman, ''Injection Molding of Shapes of Rotational Symmetry with Multiaxial Orientation,'' *Soc. Plast. Eng. J.*, **23**, 43 (October 1967).
79. R. Keuerleber and F. W. Pahl, U.S. Patent 3,706,518, Kraus Maffei, Germany (1972).
80. G. Oertel, Ed., *Polyurethane Handbook*, Hansen, Munich, 1985, Chapter 4.
81. G. Menges, K. Schwanitz, J. C. Petersen, and V. Schulte, *Kunststoff – Rundschau*, **10**, 435 (1973).

82. S. C. Malguarnera, M.S.Thesis, Deptartment of Mechanical Engineering, MIT, Cambridge, MA, 1976.
83. S. C. Malguarnera and N. P. Suh, ''Liquid Injection Molding I. An Investigation of Impingement Mixing,'' *Polym. Eng. Sci*. **17**, 111–115 (1977).
84. C. W. Macosko, *RIM Fundamentals of Reaction Injection Molding*, Hansen, Munich, 1989.
85. L. J. Lee and C. W. Macosko, *SPE ANTEC Tech. Papers*, **24**, 151 (1978); also, L. J. Lee, Ph.D. Thesis, Chemical Engineering Department, University of Minnesota, Minneapolis, 1979.
86. L. J. Lee, J. M. Ottino, W. E. Ranz, and C. W. Macosko, ''Impigment Mixing in Reaction Injection Molding,'' *Polym. Eng. Sci.*, **20**, 868–874 (1980).
87. C. L. Tucker III and N. P. Suh, ''Mixing for Reaction Injection Molding. I. Impingement Mixing of Liquids,'' *Polym. Eng. Sci.*, **20**, 875–886 (1980).
88. J. D. Domine, ''Computer Simulation of the Injection Molding of a Liquid Undergoing a Linear Step Polymerization,'' Ph.D. Thesis, Department of Chemical Engineering, Stevens Institute of Technology, Hoboken, NJ, 1976.
89. J. D. Domine and C. G. Gogos, ''Compuiter Simulations of Injection Molding of a Reactive Linear Condensation Polymer,'' *SPE ANTEC Tech. Papers*, **22**, (1976).
90. J. D. Domine and C. G. Gogos, ''Simulation of Reactive Injection Molding,'' *Polym. Eng. Sci.*, **20**, 847–858 (1980).
91. G. Odian, *Principles of Polymerization*, McGraw-Hill, New York, 1970; also, T. G. Fox and V. R. Allen, ''Dependence of the Zero Shear Melt Viscosity and the Related Friction Coefficient and Critical Chain Length on Measurable Characteristics of Chain Polymers,'' *J. Chem. Phys*., **41**, 344–352 (1964).
92. D. W. Peaceman and H. H. Rachford, Jr., ''The Numerical Solution of Parabolic and Elliptic Differential Equations,'' *J. SIAM*, **3**, 28–41 (1955).
93. R. G. Angell, Jr., U.S. Patent 3,268,636 (to Union Carbide) (1966).
94. J. L. Throne, ''Note on the Mechanical Strength of Self-skinning Foams,'' *J. Cell. Plast., 8*, 208–210 (1972).
95. J. L. Throne and R. G. Griskey, ''Structural Thermoplastic Foam – A Low Energy Processed Material,'' *Polym. Eng. Sci.,* **15**, 747 (1975).
96. P. L. Durrill and R. G. Griskey, ''Diffusion and Solution of Gases in Thermally Softened or Molten Polymers. Part I,'' *AIChE J.*, **12**, 1147 (1966).
97. A. G. Fredrickson and R. B. Bird, ''Non-Newtonian Flow in Annuli,'' *Ind. Eng. Chem*., **50**, 347 (1958).
98. E. Broyer and C. W. Macosko, ''Heat Transfer and Curing in Polymer Reaction Molding,'' *AIChE J.*, **22**, 268 (1976).
99. S. D. Lifsitz, C. W. Macosko, and F. G. Mussatti, *SPE ANTEC Tech. Papers*, **21***, 239 (1975).*
100. C. W. Macosko and D. R. Miller, ''A New Derivation of Post-gel Properties Network Polymer,'' *Macromolecules*, **9**, 206 (1976).

PROBLEMS

13.1 ***Injection Mold Runner Filling at a Constant Flow Rate*** Using the viscosity data and runner dimensions used in Example 14.1 calculate the required injection pressure to fill the entire runner at a constant rate of $1.2 \times 10^{-6}\ \mathrm{m}^3/\mathrm{s}$.

13.2 ***Filling of an Injection Mold Runner of Noncircular Cross Section*** Consider the filling of a runner, the cross section of which is formed by three rectangle sides and a semicircle. The filling takes place at a constant applied injection pressure of

20 MN/m^2. The dimensions of the runner cross section (see Fig. 12.51) are $d/B = 0.8$ and $B = 5.0$ mm, while its length is 25 cm. (a) Assuming that the polymer melt has a viscosity which is shear rate independent and equal to 6×10^3 N · s/m^2, and making the preudo–steady state assumption, calculate $Q(t)$ and $Z(t)$.

13.3 ***Relative Pressure Drops in the Runner and Gate in Injection Molding*** Consider the pressure traces on Fig. 13.5, as well as the location of the pressure transducers. Assuming that the filling process is isothermal, neglecting the "elbows" in the runner and the distance of P_3 from the gate, calculate P_1–P_2 (runner pressure drop) and P_2–P_3 (gate pressure drop) at 0.7 s. The runner distance from P_1 to P_2 is 8.0 in, its width is 0.43 in, and the thickness 0.317 in. The gate dimensions are 0.25 in wide, 0.07 in long, and 0.089 in deep. The rheological properties of the PS melt used are $\ln \eta = A_0 + A_1 \ln \dot{\gamma} + A_{11}(\ln \dot{\gamma})^2 + A_2 T + A_{22} T^2 + A_{12} T \ln \dot{\gamma}$, where $\dot{\gamma}$ is in s^{-1}, and T in °F, and η in lb$_f$ · s/in.^{2} The coefficients are $A_0 = 0.14070 \times 10^2$, $A_1 = -0.80596 \times 10^0$, $A_{11} = -0.22504 \times 10^{-1}$, $A_2 = -0.44972 \times 10^{-1}$, $A_{22} = 0.38399 \times 10^{-4}$, $A_{12} = 0.99782 \times 10^{-3}$. Compare your answers to the P_1–P_2 and P_2–P_3 transducer values appearing in Fig. 13.5.

13.4 ***"Packing" Flow during Injection Molding*** Based on the pressure values recorded in Fig. 13.5 and assuming that during the period $1.5\,\text{s} < t < 3\,\text{s}$ no appreciable skin has been formed at the positions of the transducer P_1, P_2, and P_3, obtain an estimate of the "packing flow rate" both from P_1–P_2 or P_2–P_3. Use the runner and gate dimensions given in Problem 13.3. The fluid can be assumed to be Newtonian at these slow flow rates with a viscosity evaluated from the rheological data in Problem 13.3. Check your answer by calculating the corresponding thermal contraction of the melt in the mold in the period of 1 s. The thermal expansion coefficient of the PS melt is 6×10^{-4} K^{-1}, the entering melt temperature is 400°F and the mold temperature is 75°F.

13.5 ***Design of a Multiple-Cavity Runner System*** Multicavity molds need multiple runners and gates. The accompanying figure shows one half of a center-fed eight-cavity mold, which shows one half of the mold and cavities. The design objective is to start and end filling the cavities simultaneously to attain uniform properties and to avoid flash, on the one hand, and partially filled cavities, on the other. Consider the runner–cavity system shown in the figure. Assuming equal-length branches and gates, develop design equations for the system that will predict the location of the penetrating melt and the pressure at the branching points and gates, as a function of time. Assume that the injection pressure is constant at point A, that flow is isothermal, and the fluid is incompressible and Newtonian.

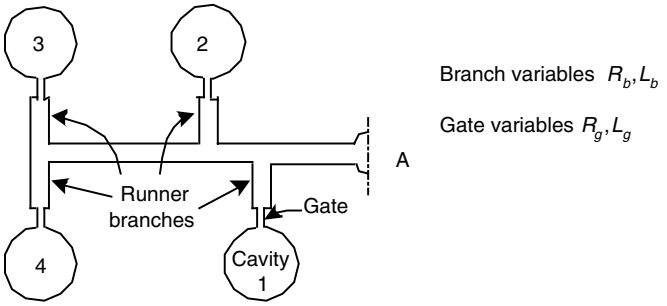

13.6 ***The 'Molding Area' in Injection Molding*** (a) Discuss the dependence of each of the curves making up the molding area in Fig. 13.6 on polymer parameters such as T_g, T_m, $m(T)$, n, k, $m(P)$, and $T_m(P)$, and thermal degradation. (b) Apply the preceding ideas to three polymers—PVC, nylon, and HDPE—whose properties appear in Appendix A.

13.7 ***The Assumption of Isothermal Cavity Filling*** As we have seen, good estimates of filling rates can be obtained by assuming that the cavity filling flow is isothermal. The success of this assumption is illustrated in Fig. 13.8 (a), where the predicted positions of the short shots are compared with the experimental ones.[1] In an attempt to investigate when the isothermicity assumption is good, Wu et al.[2] compared isothermal and nonisothermal calculated filling times for two molds (see figure). The material parameters for the PVC used in the simulations are shown on Fig. 13.10. (a) Discuss the results in terms of the "balance" between heat generated and heat lost during filling. (b) How do the isothermal and nonisothermal velocity profiles look and what physical conditions interrelate them? What can you conclude from this condition about the temperature field? (c) How would the results be for LDPE?

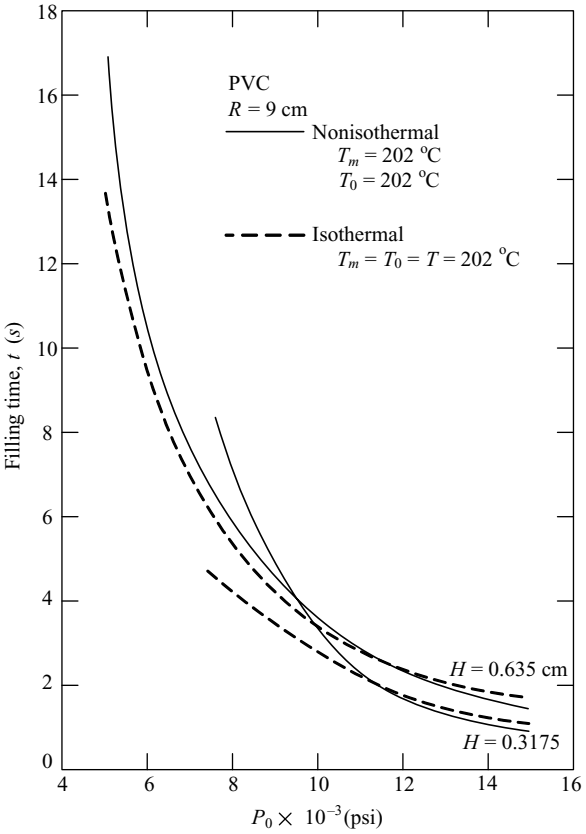

1. W. L. Krueger and Z. Tadmor, "Injection Molding into a Rectangular Cavity," *Polym. Engin. Sci.*, **20**, 426–431 (1980).

2. P. C. Wu, C. F. Huang, and C. G. Gogos, "Simulatin of the Mold Filling Process," *Polym. Eng. Sci*., **14**, 223 (1974).

13.8 ***Overall Flow-Pattern Simulation*** (a) Develop a computer model to simulate, with the FAN[3] method, the filling of a shallow mold, assuming constant gate pressure, isothermal flow, and incompressible Newtonian fluid. (b) Simulate the filling of the mold in Fig. 13.8, Case 1, identify the shape of the advancing front at various times, and the location and shape of the weld lines.

13.9 ***The Assumption of Constant Frozen-Skin Thickness*** Barrie,[4] considering the filling flow of large area articles, suggests that they be treated as isothermal flows between two plates not of the actual separation h, but $(h - 2\Delta x)$, where Δx is the frozen-skin thickness. The Δx is taken to be independent of the flow distance. Evidence supporting this assumption is brought from structural foam molding, where the solid skin thickness does not vary much. Empirical estimates of Δx indicate that $\Delta x \propto \tau^{1/3}$, where $\tau = Ah/Q$, A is the area covered during filling, and Q is the filling rate. On the other hand, from heat-transfer calculations, we find that $\Delta x \propto \tau^{1/2}$. Prove the second relationship.

13.10 ***Sandwich Injection Molding*** In the ICI sandwich molding process, two injection machines are used to fill a mold. First, a melt fills a fraction of the mold from 10% to 20%, and immediately following, the second injection machine injects a melt with a foaming agent. It is observed that the first melt forms the surface area of the entire mold. Explain the flow mechanism—sketching it out at its various stages—that makes this process possible. (A similar process has been used to mold articles of ''virgin'' polymer skin and recycled core.[5])

13.11 ***Squeezing Flow*** A disk-shaped 5-cm-diameter and 1-cm-thick molten polymer preform with $m = 5 \times 104\,\mathrm{Ns}^n/\mathrm{m}^2$, $n = 0.5$ at 200°C is placed between two plates. A 10 kg weight is placed on the upper plate. Calculate the preform thickness and diameter as a function of time.

3. E. Broyer, C. Gutfinger, and Z. Tadmor, ''A Theoretical Model for the Cavity Filling Process in Injection Molding,'' *Trans. Soc. Rheol.*, **19**, 423 (1975).

4. I. T. Barrie, *Soc. Plast. Eng. J.*, **27**, 64(1971); also, I. T. Barrie ''An Application of Rheology to the Injection Molding of Large-Area Articles,'' *Plast. Polym.*, 47–51 (1970).

5. G. Williams and H. A. Lord, ''Mold Filling Studies for the Injection Molding of Thermoplastics,'' *Polym. Eng. Sci.*, **15**, 553 (1975).